FLORIDA STATE UNIVERSITY

COLLEGE OF ARTS & SCIENCES

SEARCH FOR ISOSCALAR RESONANCES IN $\gamma p \to \omega\eta p$ AT GLUEX

By

EDMUNDO SEBASTIAN BARRIGA

A Dissertation submitted to the
Department of Physics
in partial fulfillment of the
requirements for the degree of
Doctor of Philosophy

2023

Edmundo Sebastian Barriga defended this dissertation on July 7, 2023.
The members of the supervisory committee were:

Paul Eugenio
Professor Directing Dissertation

Ettore Aldrovandi
University Representative

Alexander Ostrovidov
Committee Member

Andrew Askew
Committee Member

Sean Dobbs
Committee Member

Jorge Piekarewicz
Committee Member

The Graduate School has verified and approved the above-named committee members, and certifies that the dissertation has been approved in accordance with university requirements.

"Cuando un sueño muere es porque se ha hecho real"

Hoy te toca ser feliz - Mägo de Oz

ACKNOWLEDGMENTS

I am one of those people who knew, from an early age, what I wanted to become. This makes the conclusion of the Ph.D. the end of a childhood dream. There is a vast number of people who have helped me get to this point. At the center of them all are all of my family. Thank you all for the immense amount of support and guidance that you have provided me. Special thanks to Tom, Sol, George, and Alicia who have had been there for me the last 13 years. They gave me an opportunity to start my education in the U.S. and welcomed to their family. También quiero dar gracias a mi mamá, mi papá, Kike, Gar, y Xime. They were among the first to know of my dream and support it ever since. Chata and Rafa, thank you for your help and company. How lucky I feel that among these people I have three moms, two dads, and six siblings.

I also would like to extend my thanks to all of my teacher, professors, and other instructors. I have been lucky to always find in them people willing to help me and give me to my dreams. From FSU, I would like to thank Prof. Piekarewicz and Prof. Reina for always having their door open for me and be willing to answer the bombardment of questions I would bring. I would like to also thank Prof. Crede and Prof. Dobbs for the academic and scientific guidance that they have provided me through out the years. My FSU list would be incomplete without thanking Dr. Ostrovidov and my advisor Prof. Eugenio. I have learn so much during the last few years through our weekly discussions. Prof. Eugenio thank you also for all the opportunities you have provided me such as allowing me to participate in physics conferences and support me while I am stationed at JLab. From JLab, I would like to thank Mark Ito for all the software questions he answered. Thank you Malte and Boris for answering my PWA questions and all the knowledge you have shared with me. Special thanks to Justin who has sat down with me multiple times to talk about PWA, ambiguities in the intensity (which gave huge headaches), and more.

To all my friends and classmates, thank you for the all the times we spend together. Keke, Sean, Minah, Ruojun, Angélica, and Saheli thank you for constantly thinking of me, listening to my crazy happy stories or my afflictions. Alicia, thank you for reading and commenting parts of the dissertation. Huge thanks to my friend and role model Ashley. It was inspiring to see how you pushed yourself to obtain your goals and it was always nice to taste the things you baked. Gabe, thank you so much for keeping up with my ranting, jokes, and analysis questions. I am really fortunate of having someone like you I can count on. Luz, my Mexican bestie, I am not sure how I

would have kept my sanity if it was not for all the times we hang out together. I am grateful you are part of my life and listen to whatever song I share with you. Jason, my brother in research, we literally spend 90% of our time in grad school together, whether it was taking the same classes, sharing office space, answering each other research questions, Game of Thrones nights, etc. It is going to be strange not to have our post meeting calls. I thank you for all those times and I wish you luck in your new endeavours. Of course, I cannot forget my friends at JLab whom I constantly visit in their office when I take breaks. Special thanks to Farah who provided many feedback on the dissertation, as well as, all of the resources she shared with me. Kevin, thank you so much for working alongside me the past couple of months and for all the feedback you gave me on the dissertation. The "Flat Wave Society" could not have been started without you.

I am fortunate to always have people willing to help me. I am sure I might have forgotten to mention some of them this acknowledgments. If you are one of them, thank you for understanding that not writing your name does not mean I do not appreciate all the help you provided me. Although your name is missing, you were not forgotten. So I left a blank space to let you know this. Please come and see me and I'll be more than happy to write your name in this blank space

TABLE OF CONTENTS

LIST OF TABLES

LIST OF FIGURES

ABSTRACT

The GlueX experiment has produced the world's largest statistics for peripheral photoproduction of mesons with a goal to search for exotic mesons. This document presents results on the search for possible intermediate resonances which decay to $\omega\eta$. Little is known for the states seen in this decay channel such as the $\omega(1420)$ and $\omega(1650)$. This channel also allows to search for the never seen exotics $J^{PC} = 0^{--}$, 2^{+-}, and the elusive 2^{--}. The ω, in this reaction, is identified via the $\pi^+\pi^-\pi^0$ decay mode and the η and π^0 are identified via the decay to 2γ. Data from the GlueX Phase I was analyzed. This data was obtained at the Thomas Jefferson National Accelerator Facility utilizing the GlueX detector and a tagged linearly polarized photon beam incident on a liquid hydrogen target. A model using the expected major wave contributors, 1^{+-} and 1^{--}, shows two structure in the region where the $\omega(1420)$ and $\omega(1650)$ are expected. A third structure is seen at threshold with the quantum numbers of an h_1 resonance, however, more studies are needed to assert the nature of this structure. Instabilities on the $m = \pm 1$ were shown to come from mathematical ambiguities. This only occurs between the $m = 1$ and $m = -1$ projections when both reflectivities are present in close amount. Expanding the intensity equation for a single wave allows to extract coefficients that can help describe the data.

A tangent study is also presented in this document which consists on a direct fit to the line-shape of an isolated N(1535). This baryonic resonance is well established but its Breit-Wigner parameters have only been obtained from partial wave analysis. In contrast, this study obtained the Breit-Wigner parameters using a direct fit and finds the value of the width to be 70.5± 9.2 MeV; this is half of the accepted value.

CHAPTER 1

INTRODUCTION

A long time ago humans thought the world was made of only four elements. The philosopher Democritus first thought of a world composed of atoms: particles that were indivisible. Centuries later scientists discovered a world of multiple elements, which Dmitri Mendeleev organized on a periodic table. These elements were thought to be the indivisible particles that make up the world and were coined "atoms." By the end of the twentieth century scientists had discovered that these atoms had an internal structure, making the names of the elements a fancy way of counting protons. Atoms are composed of three particles: electrons, protons, and neutrons. Electrons are point-like particles; protons and neutrons, however, are composite particles. Initially scientists thought that protons were point-like particles, but deep inelastic scattering of electrons into protons showed that they had structure. They are made of quarks [41]. This insight was a great inspiration because physicists found a zoo of particles. The quark model, which was thought to be a mathematical construct, provided a framework to this zoo by describing physical states. During that time theorists were also working on Quantum Electrodynamics (QED) to explain the interaction between light and electrons. With time QED became the most successful theory; meaning that physicists were able to predict with high precision the outcome of an experiment. Inspired by QED, theorists adventured to explain the strong force with a similar theory. And thus, quantum chromodynamics (QCD) was proposed as a theory to describe the interaction between protons, neutrons, and other particles made of quarks.

Physicists have used QCD to successfully predict the outcome of different experiments. QCD at high energies is a perturbative theory similar to QED; but at low energies, perturbation techniques can not be used in QCD [22]. This is not a defect of the theory but a complication, which requires physicists to use supercomputers to try to solve problems of QCD at low energies. Lattice QCD (lQCD) is a common approach to address the non perturbative nature of QCD. It consists on performing QCD in a lattice where space-time is discrete. The resulting predictions vary depending on the lattice volume and some conditions like the mass of the pions. Even with these complications, the Hadron Spectrum Collaboration was able to predict the observed states in the quark model, but it also predicts more Fig. 1.2. These new states contain gluons in their bound state as well as

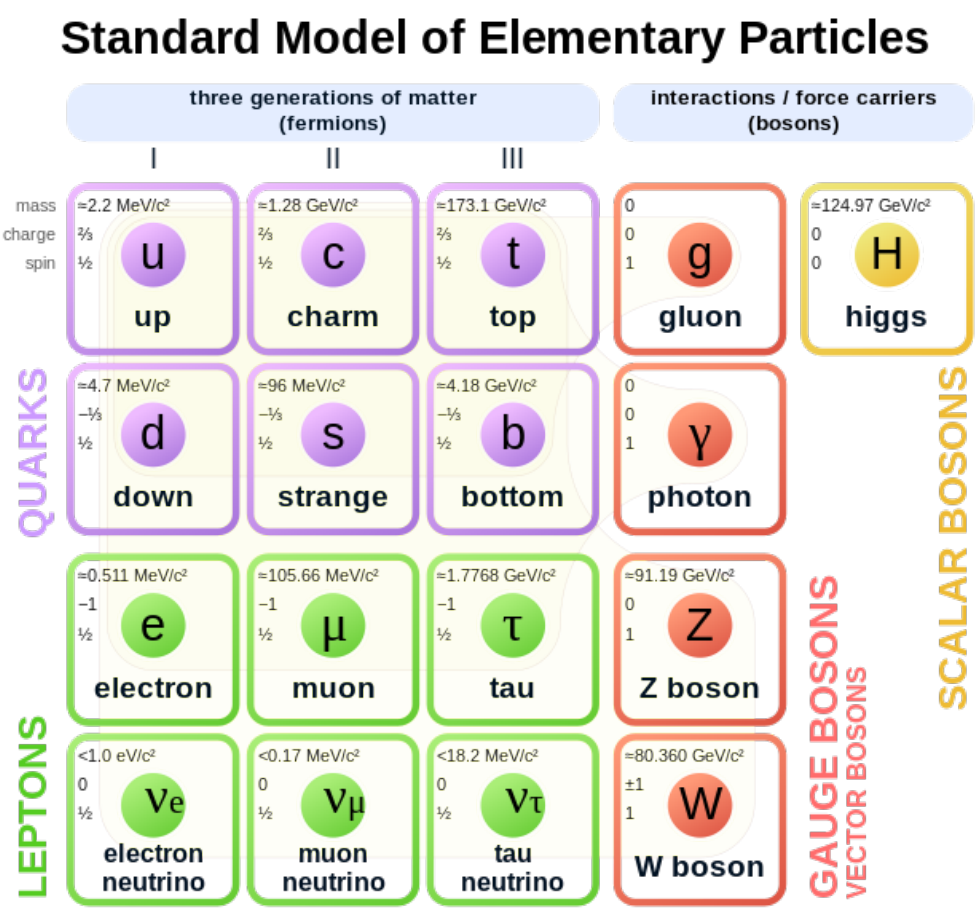

Figure 1.1: Particles in the Standard Model. A theoretical frame from which QED and QCD are part [11].

quarks, providing extra spin and angular momentum. They are called hybrid states. A subset of these states have quantum numbers that are only achievable through the excitation of the gluon. Because of this, they are called exotic mesons. The flux tube model is a theoretical framework that explains how gluons can give angular momentum to create exotic mesons [10][7][44]. There have been experimental attempts to look for hybrid states. From this, three particles came out as exotic meson candidates: $\pi_1(1400)$, $\pi_1(1600)$, and $\pi_1(2015)$ [43]. However, there is a theoretical argument that suggests the $\pi_1(1400)$ and $\pi_1(1600)$ are the same particle since they can be described by the same resonant pole [47]. Theoretical calculation lQCD, put $\pi_1(1600)$ as the lighter exotic meson [12] Fig. 1.2. The $\pi_1(2015)$ was seen in $f_1\pi$ and $b_1\pi$ decays by the E852 collaboration [18][15]. While it could be the first excitation of the $\pi(1600)$, there is not enough experimental evidence to establish it as such[43]. There is particular interest in finding the experimental evidence for the

isoscalar partners of the π_1. This would help consolidate the pi_1 as a hybrid meson, rather than an isolated anomaly. Recently, the BESIII collaboration claimed to observe the η_1, the isoscalar partner of the π_1, with a statistical significance larger than 19σ [17]. Consequentially, evidence of lightest hybrid nonet sparks enthusiasm to search for other particles with exotic quantum numbers.

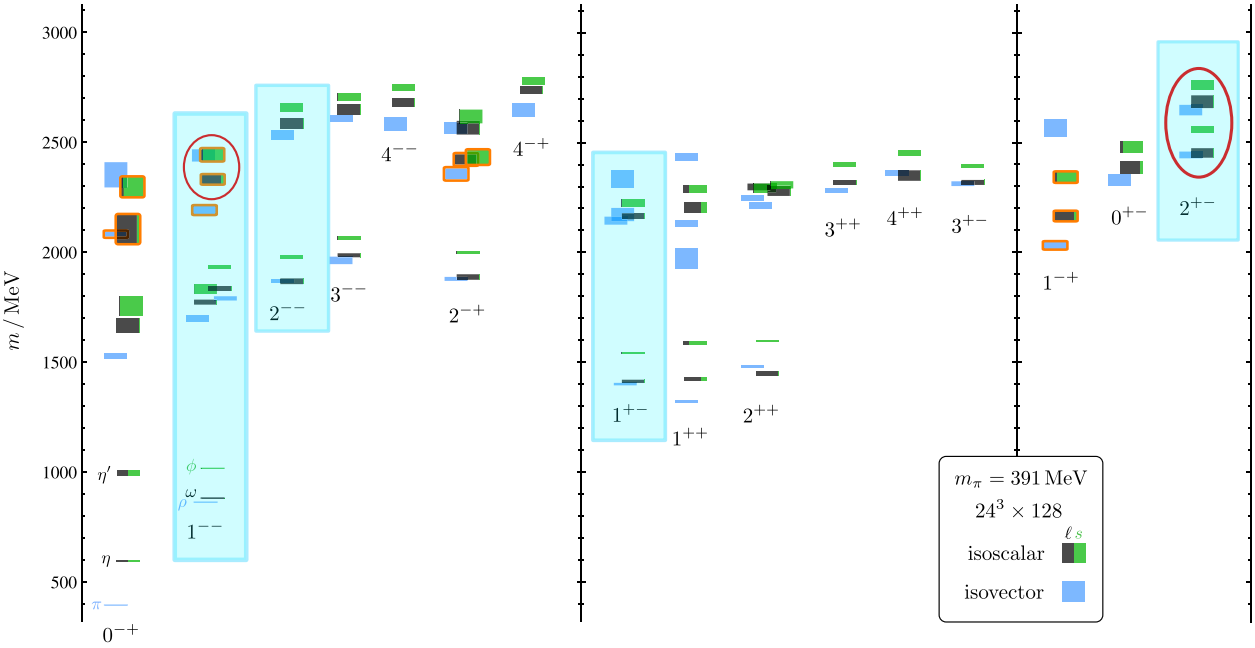

Figure 1.2: Meson spectrum from lQCD calculations [12]. Vertical height is the uncertainty on the mass. States with orange boxes are the lowest mass hybrid mesons. The isoscalar states in the light blue columns are allowed to decay to $\omega\eta$. The ones encircled in red are some of the possible hybrid mesons.

1.1 Motivation to Study $\omega\eta$ Decay

Mesons are classified by their I^G and J^{PC} quantum numbers. The I^G describe the quark content in the meson. The number I is the isospin and it is calculated by adding the the quarks: $\frac{1}{2}$ for an up quark and $-\frac{1}{2}$ for a down quark. The number G is the G-parity and it is a generalization of the C-parity. To calculate G, the following equation is needed $G = (-1)^{L+S+I}$. The other quantum numbers that distinguish mesons are J^{PC}. Here J is the total angular momentum of the system, P is the parity, and C is the charge conjugation. To obtain these quantum numbers one must compute the following equations: $\vec{J} = \vec{L} + \vec{S}$, $P = (-1)^{L+1}$, and $C = (-1)^{L+S}$. Note that J can have values between $|L - S|$ and $L + S$. Here S is the spin of the particle and L is the angular momentum. Exotic mesons, as mentioned earlier, will have J^{PC} combinations that are

only possible when the gluon is excited. This project analyzes the reaction $\gamma p \to \omega\eta p$. The J^{PC} values of states allowed to decay to the particles in the reaction are listed in Fig. 1.3. The final state particles ω and η have quantum numbers 1^{--} and 0^{-+} respectively. The quantum numbers of these particles are not "exotic", but they could have a parent particle whose J^{PC} combination is exotic. These are encircled in red on Fig. 1.3. The 2^{+-} states may be accessible in the data set of this study according to Fig. 1.2, with the caveat that the masses on the table are just estimates. The 0^{--} states are expected to be around 3.8 GeV [39][43] and it may be possible to observe them as well . If the 2^{+-} states are observed, they will be the first exotic tensor mesons to be discovered. Meanwhile, if the 0^{--} is observed, it could lead to new evidence for a glueball state [43]. If neither is observed, it could indicate that these states have a broad mass; or that they lie at higher masses. The lattice calculations of that chart also predict at least a hybrid meson with quantum numbers 1^{--} that is possible to observe. Three out of the four non-hybrid 1^{--} states in the estimated 1.5 - 2.0 GeV mass range have probably been observed. This would be consistent with the nonet grouping of mesons from the Particle Data Group [19] Fig. 1.4. The details of two of these particles are discussed in the following section. The third one, most likely the $\phi(1680)$, is not expected to be observed in this decay due to its $s\bar{s}$ content. Similarly, three out of four 1^{+-} states have been observed Fig. 1.4. The $h_1(1170)$ is below the $\omega\eta$ threshold and the $h_1(1415)$ has only been seen in $K\bar{K}^*$. The third state will be discussed also in the following section.

l	J^{PC}		
0		1^{+-}	
1	0^{--}	1^{--}	2^{--}
2	1^{+-}	2^{+-}	3^{+-}
3	2^{--}	3^{--}	4^{--}

Figure 1.3: This table shows the possible J^{PC} that are allowed to decay to $\omega\eta$. The relative angular momentum between the ω and η is l. Two exotic states are encircled in red. Two states that have been observed are enclosed in a green. The yellow box is enclosing a state that is not exotic, but it has not been seen in light meson decays.

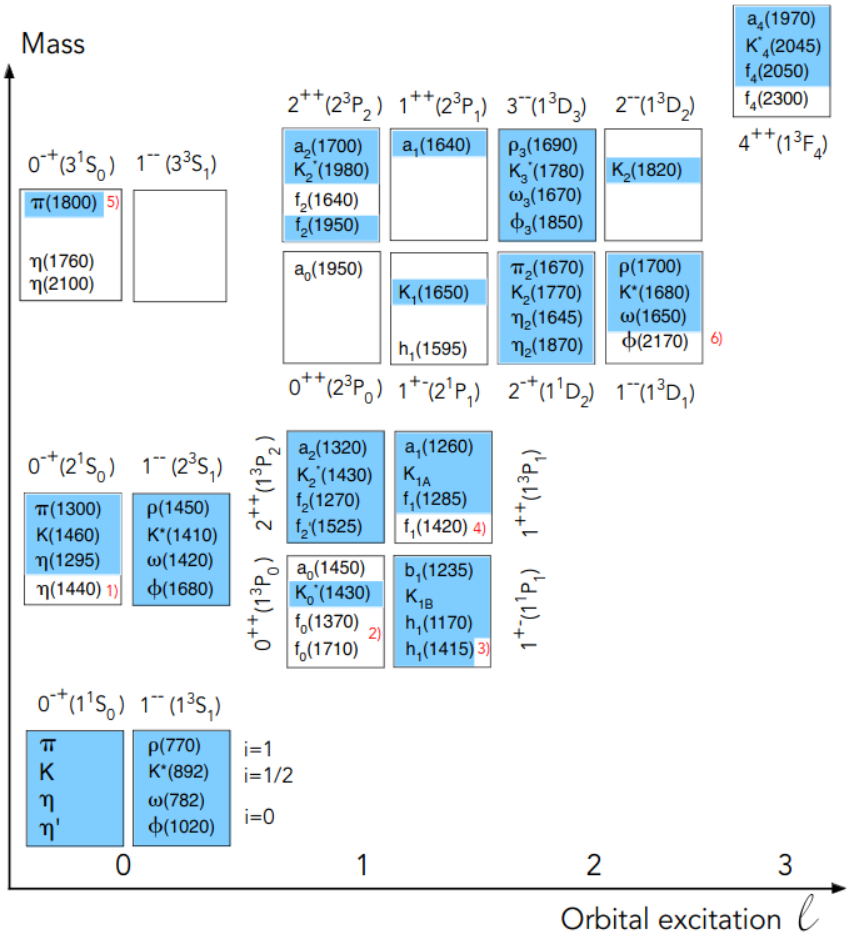

Figure 1.4: The light mesons organized in $J^{PC}(n^{2s+1}\ell_j)$ nonets with isospin i. The established mesons are blue, while the others have a tentative nonet classification [19].

1.2 Experimental Status

The lack of experimental exploration into the $\omega\eta$ final state is a motivation for this study. Only a handful of experiments have taken a look at $\omega\eta$. Some of this experiments were limited by their statistics or did not have access to all possible J^{PC} values for the parent states. The full description of the data analyzed in this study is: $\gamma p \to \omega\eta p$, where $\omega \to \pi^+\pi^-\pi^0$ and both the π^0 and η decay into 2γ. The data gathered at the E852 experiment at Brookhaven National Lab is the closest one to the one presented here. This experiment used an 18 GeV pion beam incident to a proton target and reported ~20,000 exclusive $\omega\eta$ events. Their Partial Wave Analysis (PWA) study extracted two resonances Fig. 1.5 [28] . The first is the $\omega(1650)$. This resonance could be one of the isoscalar 1^{--} states in Fig. 1.2. The $\omega(1650)$ has also been seen in cross-section measurements (Fig. 1.6)

such as the ones performed by the collaborations SND [31], CMD-3 [27] and others. The second particle the E852 experiment saw was the $h_1(1595)$. This is a new resonance and it still needs to be confirmed. However, it is consistent with the 1^{+-} isoscalar state of Fig. 1.2. It was impossible for the other experiments that reported the $\omega(1650)$ to see an $h_1(1595)$ since they did not have access to it due to the quantum numbers of their beam. The electron-positron annihilation, these other experiment used, has $J^{PC} = 1^{--}$. Without extra particle interaction that can provide more momentum to the system, these experiments can only observe 1^{--} states. While, GlueX (Chapter 2) uses a photon beam with also $J^{PC} = 1^{--}$, it has access to more states since the beam is incident on a proton target. GlueX could not only help establish the h_1 resonance, but it will also have access to quantum numbers not allowed with a pion beam. The SND and CMD-3 also reported a third particle not observed in the E852 experiment; the $\omega(1420)$ Fig. 1.6. The $\omega\eta$ channel has the possibility to see some ϕ particles too. BESIII reported the $\phi(2170)$ in their electron-positron annihilation experiment [26]. A short summary of the experiments can be found in Table 1.1

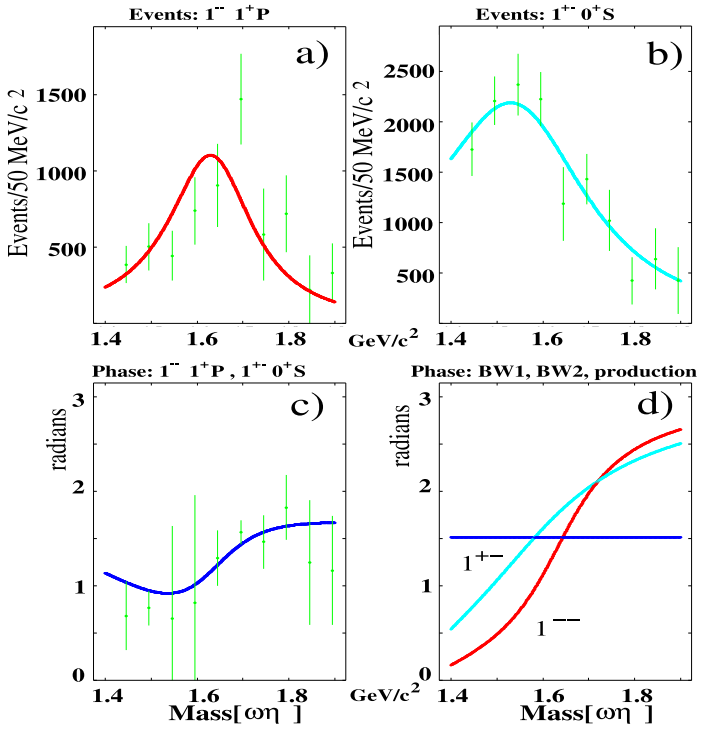

Figure 1.5: These plots are from the E852 collaboration [28]. Plots **a)** and **b)** show a Breit-Wigner fit to the 1^{--} and 1^{+-} partial waves. Plot **c)** shows the phase difference between 1^{--} and 1^{+-}. And, plot **d)** the individual Breit-Wigner phases.

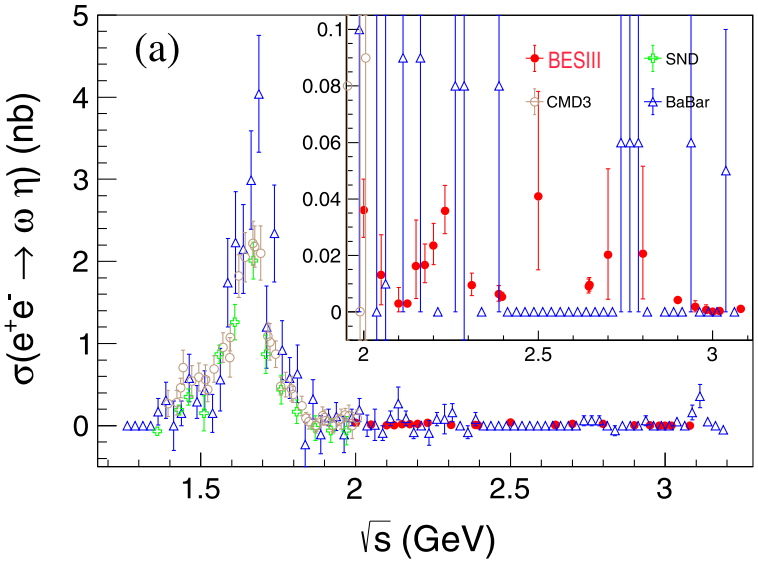

Figure 1.6: Cross-section results of multiple experiments [26]. There are two structures in the lower mass. The first is proposed to be the $\omega(1420)$ and the second the $\omega(1650)$. The zoomed region corresponds to BESIII work and shows some structure above 2GeV.

Unfortunately, all of these particles lack rigorous information about them. Some of their Particle Data Group (PDG) information pages "does not use any of the studies" to "estimate" the mass and width of the particles [19]. This means that the PDG used the observed data range and rather than a weighted average to estimate the particle properties. The lack of statistical significance in some experiments and the high variation between the measured parameters might be to blame. GlueX should provide a high volume of data which should help to solidify the status of these particles. Even more exciting than validation of previous measured particles, this channel offers the possibility to find new and interesting particles. One of such particles is the elusive state with $J^{PC} = 2^{--}$. This particle is predicted by the quark model and it has yet to be seen. Estimations using lQCD [12] set the mass of this particle between 1.5 and 2 GeV. A hybrid meson with quantum numbers of 1^{--} is expected above 2 GeV. It is also possible to observe exotic mesons. As mentioned earlier, these particle would have a J^{PC} of 0^{--} or 2^{+-}.

1.3 Goal of This Study

This study aims to solidify the status of the resonances that are present in the $\omega\eta$ decay channel. The ideal method to study the resonance contributions in a system is through a PWA. The procedure is similar to the one performed by the E852 collaboration. However, this work would be

Table 1.1: This table summarizes the different experiments that have looked into the $\omega\eta$ channel. The ω decays to 3π in all experiments except in the SND experiment; the SND look at $\omega \to \gamma\pi^0$. The Omega Photon Collaboration did not have a polarized photon beam.

Experiment	Reaction	Beam Energy	Statistics	Analysis	Particles Observed
Omega Photon [30]	$\gamma p \to \omega\eta p$	25 -50 GeV	∼100	Cross-section	peak at 1.61 GeV
BESIII [26]	$e^+e^- \to \omega\eta$	2.00 - 3.08 GeV	∼200	Cross-section	$\phi(2176)$
CMD3 [27]	$e^+e^- \to \omega\eta$	1.394 - 2.005 GeV	∼800	Cross-section	$\omega(1420)$, $\omega(1650)$
SND [31]	$e^+e^- \to \omega\eta$	1.05 - 2.00 GeV	∼900	Cross-section	$\omega(1420)$, $\omega(1650)$
BaBar [25]	$e^+e^- \to \omega\eta$	4.5 GeV	∼1.4k	Cross-section	$\omega(1650)$
E852 [28]	$\pi^-p \to \omega\eta n$	18 GeV	∼20k	Partial Wave Analysis	$\omega(1650)$, $h_1(1595)$

among the first linearly polarized photoproduction PWA of a vector-pseudoscalar decay. The data from GlueX differs to that of the Omega Photon Collaboration since GlueX has a linearly polarized beam and the Omega Photon Collaboration's statistics were scarce Fig. 1.7 [30] . The theoretical work on linearly polarized photoproduction of vector-pseudoscalar final state is in development. Different GlueX analyses, including this one, are pioneering the experimental applications. These analyses should aid to provide insight to theoretical framework. Other vector-pseudoscalar decays currently under analysis at GlueX are: $\gamma p \to \omega\pi p$, $\gamma p \to \omega\pi^-\Delta$[50], and $\gamma p \to \phi\eta p$ [5]. Some of these channels allow to test the robustness of the theoretical framework by comparing it to previously measured quantities. For example, the particle $b_1(1235)$, which decays to $\omega\pi$, is a well established resonance. Properties such as its D wave to S wave ratio, D/S, extracted from GlueX can be compared directly to that of many other experiments. This and similar amplitude ratios are sensitive to the decay dynamics. An accurate extraction of amplitude ratios could provide distinguishing power for model predictions [33][38].

This concludes the introduction. The next chapter will describe the different component of the GlueX experiment. This is followed by a chapter which breaks down the different data selection and statistical methods handle background performed in the analysis. Chapter 4 details the PWA fits and its accompanied with a mathematical explanation for the instabilities seen in the $m = \pm 1$ waves. Furthermore, there is a tangential study that consists of a line-shape description of the N(1535); an isolated baryonic resonance in M[ηp]. In the last chapter, contains suggestions on how to move forward for an angular description of the $\omega\eta$ channel; as well as the next steps in the N(1535) study.

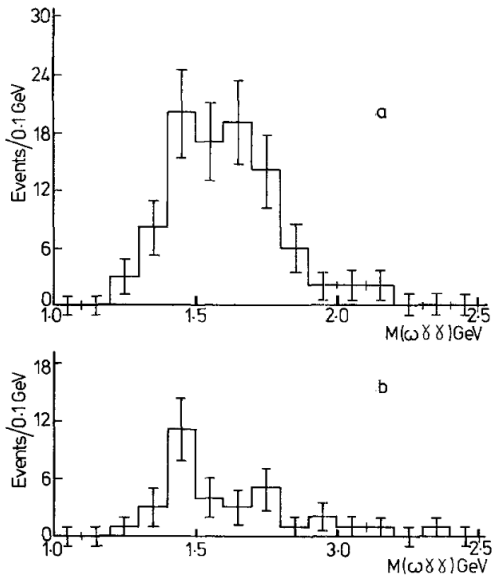

Figure 1.7: The Omega Photon Collaboration reported less than 1000 $\omega\eta$ events [30]. The upper plot **a** shows the invariant mass for $\omega\eta$. The lower plot **b** shows the sideband contribution.

CHAPTER 2

THE GLUEX EXPERIMENT

The main goal of the GlueX (gluonic excitation) experiment is to map out the light spectrum of hadrons and search for hybrid mesons [10]. The experimental facilities are located in Hall D at Thomas Jefferson National Accelerator Facility (JLab) in Newport News, Virginia. The devices and methods used to reconstruct events at Jefferson Lab are detailed in the following section. This section is based on the condition for GlueX Phase I, which took collected data between 2017 and 2018. GlueX Phase II will upgrade some of the current detectors and it will add a Cherenkov detector, DIRC, to aid in the identification of kaon final states [16].

Figure 2.1: Aerial view of CEBAF with its four halls labeled from A to D [6].

2.1 Continuous Electron Beam Accelerator Facility

The Continuous Electron Beam Accelerator Facility (CEBAF), as the name implies, delivers a continuous beam to up to four different experiments Fig. 2.1. Each experiment is located in a Hall labeled from A to D. At CEBAF, a laser is directed into a single photocathode to produce the electron beam bunches every 4 nanoseconds. It is possible to use up to three independent lasers allowing each beam to have different characteristics but they would repeat every third bunch Fig. 2.2a. These beam bunches are separated through the use of radio frequency cavities. This allows distinct beams to be delivered to multiple halls. The beams are accelerated using the five-pass recirculating linear accelerator (linac) Fig. 2.2b. When accelerated the beams occupy the same spatial location, but during re-circulation the beams are given unique arcs to accommodate the specific beam momentum an experiment needs Fig. 2.2c. With this mechanism CEBAF can deliver beams of up to 200 μA with 75% polarization, with energies ranging from 0.6-12 GeV [40].

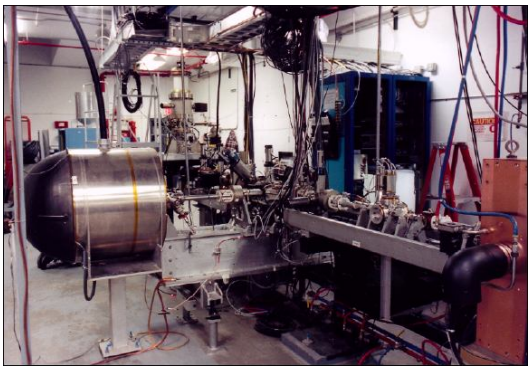

(a) CEBAF injector equipment

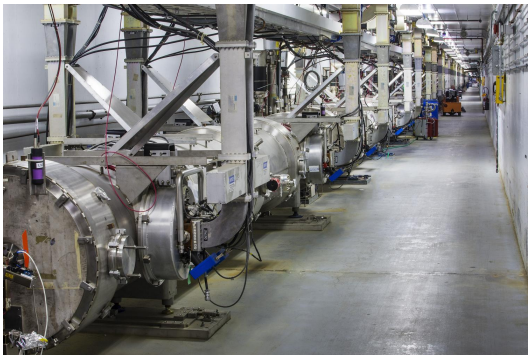

(b) CEBAF linear accelerator segment

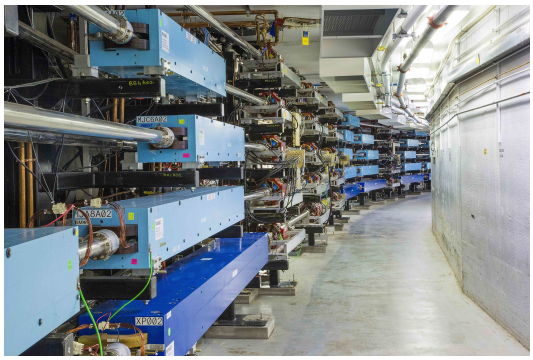

(c) CEBAF magnet arcs

Figure 2.2: Pictures of different sections inside CEBAF [32]

2.2 Coherent Photon Beam Source

GlueX is a photoproduction experiment, meaning that it uses a photon beam to produce the particle interactions. This section summarizes how the electron beam from CEBAF produces photons, and the equipment used to measure the photon beam's qualities. This information helps understand what is hitting the target and producing particles.

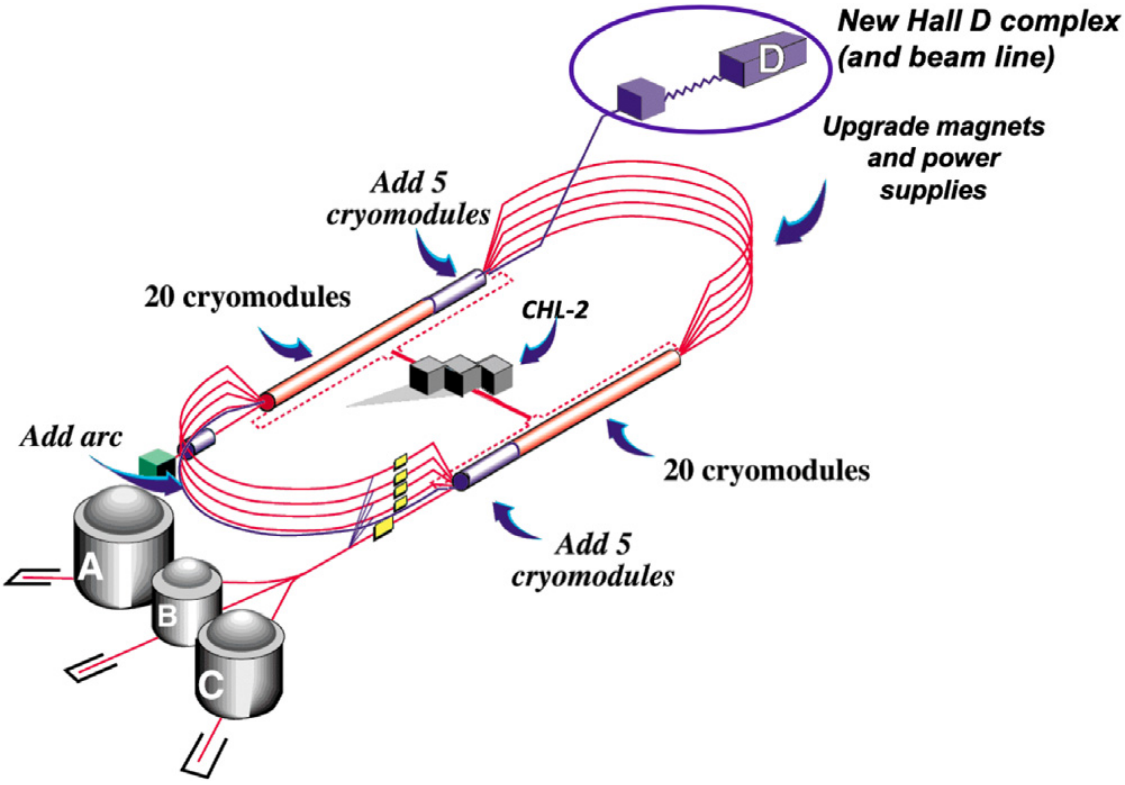

Figure 2.3: The diagram shows the upgrades to CEBAF as for the 12 GeV era.

For the data produced, GlueX takes advantage of a recent addition – an extra recirculating arc added during CEBAF's 12 GeV upgrade Fig. 2.3. This lets Hall D receive an electron beam that has gone through one additional acceleration stage in the North linac, which allows it to have a maximum energy of 12 GeV. Upon arrival, the electron beam interacts with a 50 μm thick diamond radiator to produce linearly polarized photons, via a process called coherent bremsstrahlung. It is an enhancement to normal bremsstrahlung, in which photons are produced when the momentum transfer from the electron to the atom matches a reciprocal lattice vector [35]. This produces highly polarized and monochromatic photons. The photons will proceed towards Hall D, while the

scattered electrons are bent by the tagger magnet to measure their energy. Electrons that did not interact in the diamond are sent to the electron beam dump.

Radiator. The GlueX experiment counts with two type of radiators: a diamond crystal that produces linearly polarized photons and an aluminium radiator which produces unpolarized photons Fig. 2.4. The linearly polarized photons appear as peaks in the photon energy distribution Fig. 2.5. The position of this enhancements, as well as the polarization of the beam, depends on the orientation of the diamond crystal. For GlueX, the configuration allows for a dominant coherent peak at 9 GeV with a corresponding linear polarization of 40% [29].

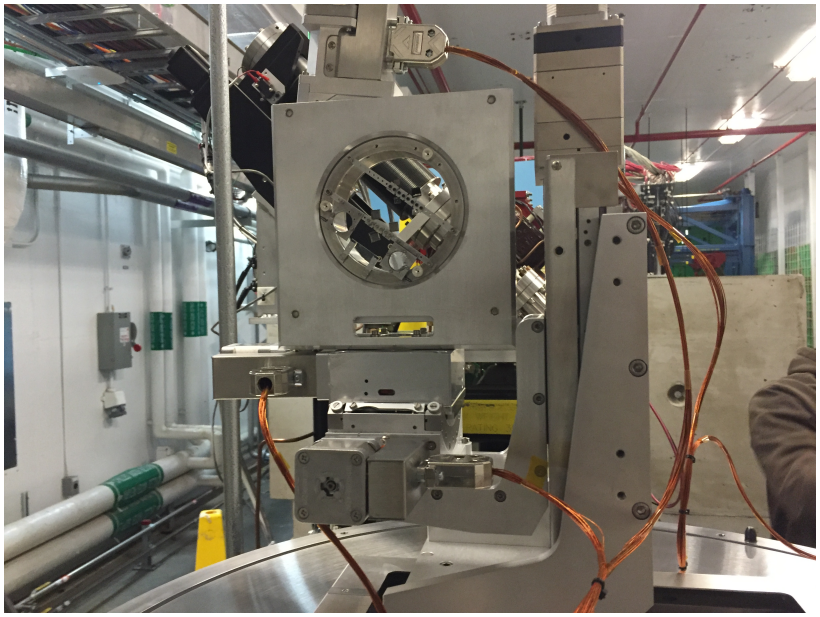

Figure 2.4: The radiators mounted on the goniometer, a device to adjust finely its position.

It is worth mentioning that the diamond's small lattice constant and high Debye temperature gives the diamond a high probability for coherent bremsstrahlung scattering [13]. This paired with the diamond's conductivity and radiation hardness makes the diamond an excellent choice for the high intensity electron beam at GlueX.

2.2.1 Measuring Photon Beam Properties

Taggers. The photon energy is measured from the scattered electrons. In the tagger hall, the recoiled electrons are deflected by magnets to two apparatuses that accomplish this task: the Tagger Microscope (TAGM) covers, through an array of scintillating fibers, the 8 to 9 GeV energy

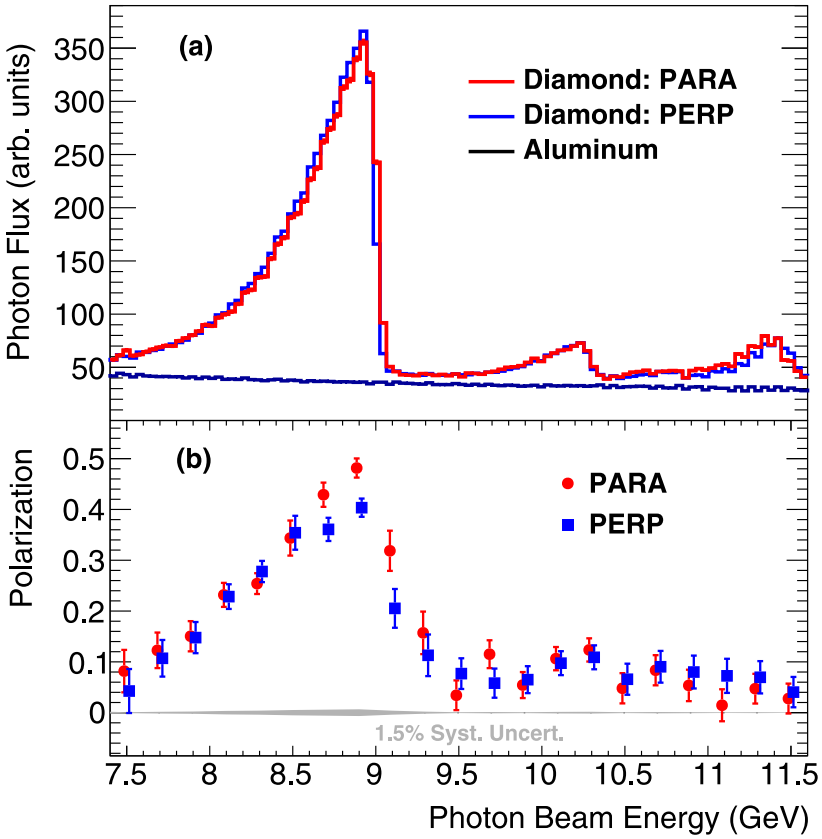

Figure 2.5: The Upper plot shows the coherent bremsstrahlung enhancement for both diamond orientation (red and blue) and the incoherent base produced by the aluminum radiator (black). The bottom plot shows the polarization fraction as a function of the beam energy [29]

range; and the Tagger Hodoscope (TAGH) which cover energies from 3-8 GeV and from 9-12 GeV. The following equation determines the energy of an individual photon:

$$E_\gamma = E_0 - E_e \tag{2.1}$$

Where E_0 is the initial energy of the electron beam and E_e is the energy of the electron after the interaction with the diamond radiator measured by either the TAGM or TAGH Fig. 2.6a. Multiple interactions in the diamond radiator introduce uncertainties in E_γ of the same order as the spread of energies in the beam's electrons. The TAGH consists of 222 scintillator counters. The TAGM is located within a gap in the middle of counters. This gap also corresponds to the recoiled electrons that produced the primary coherent peak from the coherent bremsstrahlung scattering Fig. 2.6b. The TAGM's scintillating fibers are divided horizontally into 102 columns. Each column is further

broken down vertically in five rows. The detection efficiency of the TAGM averages 75% across its full energy range, in good agreement with the geometric factor of 77% [29].

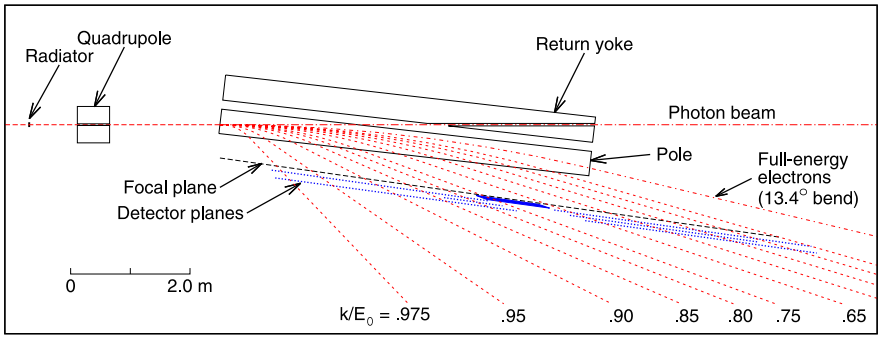

(a) Diagram showing the spread of the taggers (blue)

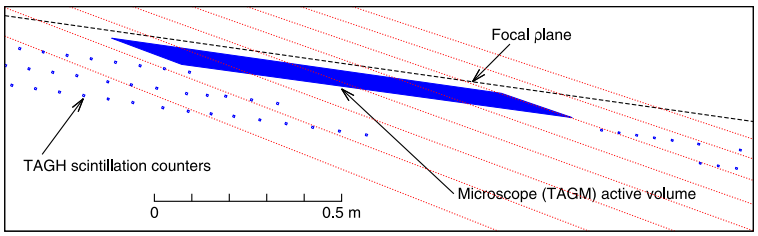

(b) A closer look to the tagger region showing the gap in the TAGH and the TAGM region

Figure 2.6: Diagrams of the electron taggers [29]

Polarization and Flux. After the photons pass through the taggers, they pass through the primary collimator. This is a tungsten block with an aperture of 5 mm, located at a distance about 75 m from the radiator. Its purpose is to remove incoherent photons since the coherent bremsstrahlung photons have a smaller angular spread. It also provides feedback in case the electron beam needs to be steered. Fig. 2.7. Ahead of this collimator, there is a beryllium radiator which will be used by the Triplet Polarimeter (TPOL) and the Pair Spectrometer (PS). They measure the linear polarization of photons and the photon flux respectively. An e^-e^+ pair is produced when the photon beam hits an atomic electron in the beryllium foil. The reaction is $\gamma e^- \rightarrow e^-e^+e^-$. The TPOL uses a silicon strip detector to measure the azimuthal distribution of the atomic electrons scattered from that reaction. The polarized cross-section of the above reaction is then used to calculate the degree of polarization:

$$\sigma = \sigma_0[1 - P_\gamma \Sigma cos(2\phi)] \tag{2.2}$$

Here σ_0 is the unpolarized cross-section that is modified by the degree of polarization (P_γ), (ϕ) is the azimuthal angle of the scattered atomic electron, and Σ is the beam asymmetry, which is known from QED calculations The TPOL relies on the PS to trigger on e^-e^+ pairs to coincide with the recoiled electron. On top of that, the PS determines the photon flux by counting the fraction of beam photons converted into the e^-e^+ pairs. The beam flux calculation starts by integrating the number of photons for each beam energy bin. These bins are dictated by the energy division of the taggers. A special type of calibration run using the Total Absorption Counter (TAC), a small calorimeter, is performed to determine the detection efficiency for leptons in the PS. With this information plus the converter thickness and acceptance the photon flux is calculated with an expected precision of up to 1% [29].

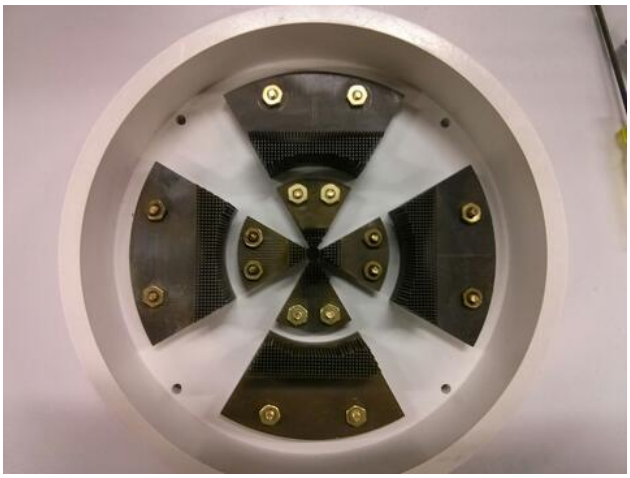

Figure 2.7: The active collimator helps improve the polarization fraction of the beam. [34]

2.3 GlueX Spectrometer

The GlueX detector Fig. 2.8 has almost a full angular coverage to detect charged and neutral particles. It employs multiple types of detectors, which will be detailed in the following section. The tracking detectors provide information about charge particles. The electromagnetic calorimeters measure the energy of neutral particles. Finally, the scintillation detectors contribute mainly timing information that is used for particle identification. For reference, the coordinate system used in the description of the detector is as follow: The z-axis is defined along the direction of the photon beam. The y-axis points up and since this is a right-handed coordinate system, the x-axis is defined

as the cross-product of the other to coordinates. The origin is placed 50.8 cm downstream which makes the nominal center of the target at (0,0,65 cm) [29].

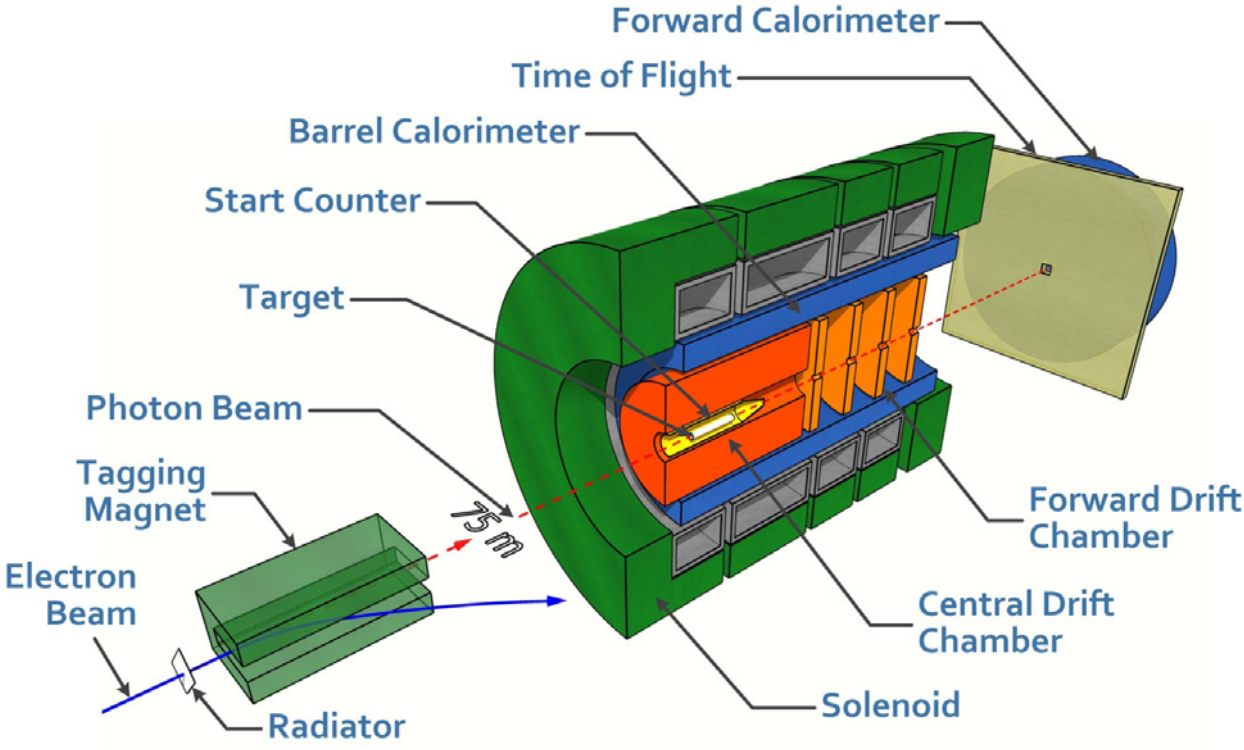

Figure 2.8: GlueX spectrometer and beam line.

2.3.1 Target

GlueX uses a liquid hydrogen (H_2) target. Hydrogen, having no neutrons, is the best choice of an element for the target. This allows the physicists observing particle reactions to assume that the reaction comes from photons interacting with protons. The gas is liquefied to increase its density and, consequentially, increase the chances for photon-proton interactions. The target cell is contained within an aluminum and stainless steel vacuum chamber, which is in turn, surrounded by a foam chamber. The Start Counter (Section 2.3.4) encloses these chambers and helps support the horizontal portion of the vacuum chamber. The target is 30 cm long and it is located 50 cm inside the spectrometer; where 0 is defined where the solenoid (Section 2.3.2) starts. During standard settings, the target cell is filled until it reaches a pressure of 19 psi. The liquid inside the cell cools down to about 20.1 K. This temperature, 1 K below the saturation point of H_2, eliminates boiling in the target. The density of H_2 at this temperature is 71.2 $\pm$ 0.3 mg/cm^3.

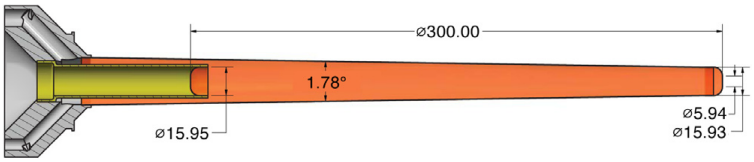

Figure 2.9: Diagram showing the target cell dimensions in mm.

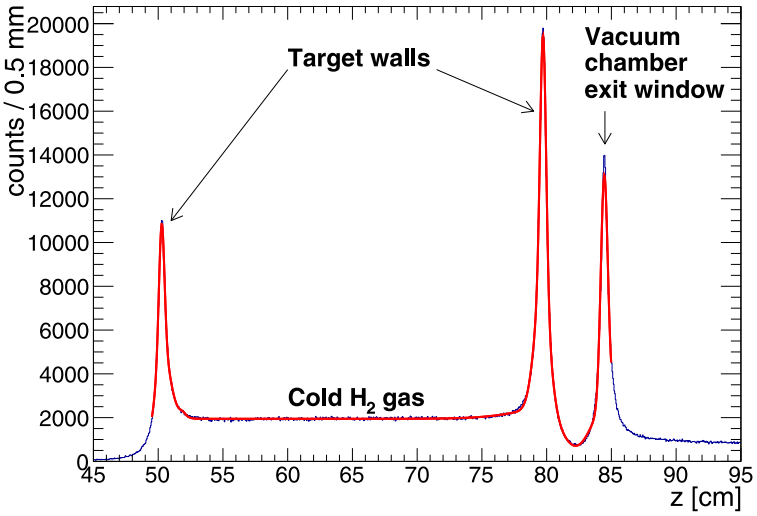

Figure 2.10: The target cell dimensions can be noticed on an empty target run.

2.3.2 Tracking Detectors

Solenoid. While not a detector, the superconducting solenoid works in conjunction with the tracking detectors Fig. 2.11. It makes charged particles travel helical paths from which their energy and momentum can be calculated. The solenoid has an inside diameter of about 2 m and a length of about 4.8 m. Its magnetic field of 2 T, when operated at the standard current of 1350 A, runs in the direction of the beam line.

Figure 2.11: GlueX solenoid in Hall D before full installation.

Central Drift Chambers. The Central Drift Chamber (CDC) measures the position, timing, and energy loss of charged particles. It is located inside the Barrel Calorimeter (Section 2.3.3) and surrounds the Start Counter. The CDC is able to track particles that leave the target with angles between 6° and 168°. It is made of 28 layers of Mylar tubes containing, in total, 3522 anode wires. The layers are divided as follow: 12 layers are axial and 16 are at stereo angles of ±6° Fig. 2.13. Inside the tubes, there is a mixture of gases at atmospheric pressure. About 50% is argon and the other 50% is carbon, a small admixture of isopropanol is added to the mixture to prevent loss of performance. This combination of gases provides drift time characteristics for good position resolution [24].

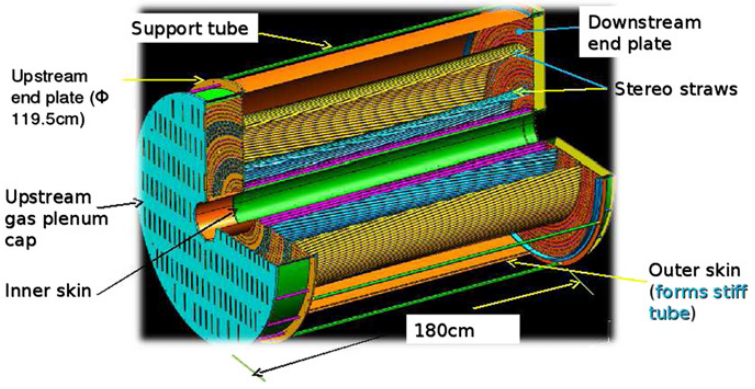

Figure 2.12: Diagram showing the different parts of the CDC.

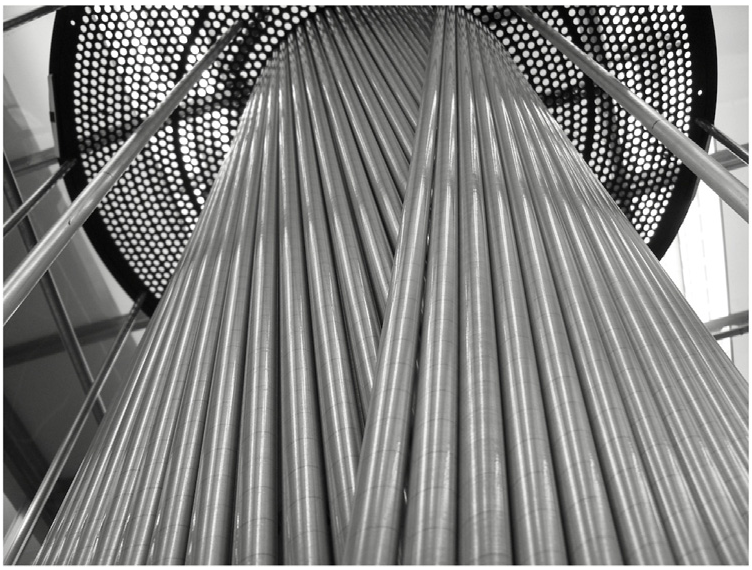

Figure 2.13: Picture showing the some of the tube layers of the CDC before full installation.

Forward Drift Chambers. The Forward Drift Chamber (FDC) consists of four groups with a total of 24 disc-shaped chambers Fig. 2.15. They are supplemented with cathode strips on both sides to aid reconstruction of a space point from each chamber. A particle leaving the target between 1° and 10° will be tracked through all the chambers. However, partial coverage is possible for angle up to 20°. Each chamber in the FDC consist of a wire plane with cathode planes Fig. 2.14. Inside the chamber, there is a mixture of 40% argon and 60% carbon dioxide to reduce the magnetic field effects produced by the chambers components.

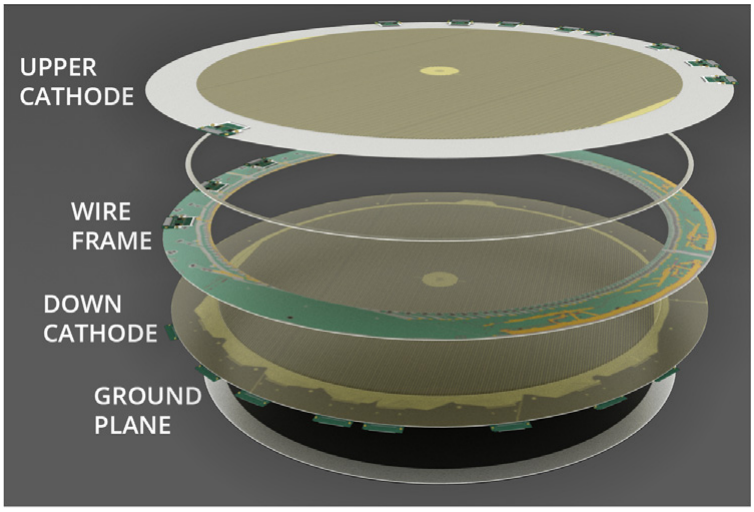

Figure 2.14: A diagram of an FDC chamber showing its different components.

Figure 2.15: FDC side view showing the installed chamber packages.

Reconstruction. GlueX follows a three step procedure to reconstruct charged particles. The first step consists of forming track segments and linking them together. In the FDC, particles hit the adjacent disk layers, and these hits form segments that are then linked together. A helical model calculates the track parameters, and track candidates are identified. Meanwhile, in the CDC, hits in the adjacent rings become track segments. Multiple segments are linked together and then fitted with circles perpendicular to the beam axis. To form a CDC track candidate, first the intersection between these circles and the stereo wires is found, and then a linear fit is performed to find the position along the z axis (direction of the beam) and the tangent to the magnetic field. The tracks that leave the target between 5° and 20° passing through the FDC and CDC are linked together. The second step aims to extract the track parameters. These are extracted from a fit at the position of closest approach of the track to the beam line. To perform the fit, GlueX uses a Kalman filter [37][36]. This algorithm works in multiple steps. It starts from the farthest point of the track and makes its way to the beam line. The energy loss and multiple scattering are taking into account in this procedure. During this reconstruction steps, the tracks are assumed to be pions, except for low momentum particles (momentum < 0.8 GeV) which are assumed to be protons. The drift times are not used in this step. The third step uses the information gathered from other detectors to assign a starting time. This way, the drift times can be used in the fit. The tracks are refitted,

but this time, besides the drift times, the track's fit switches the mass of the particle to e, π, K, and p.

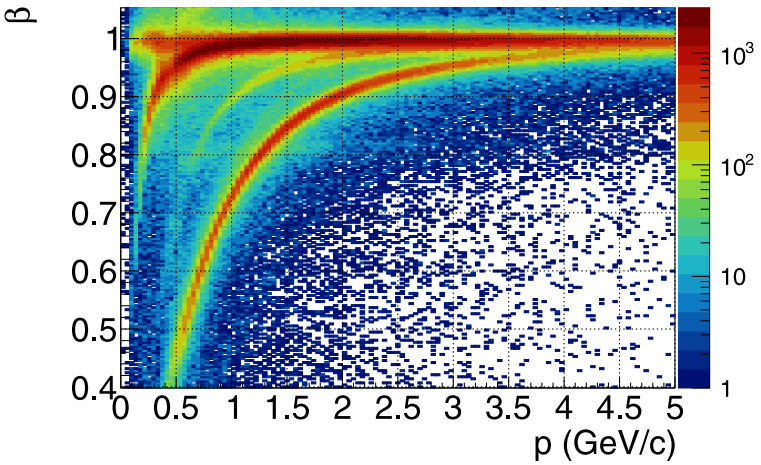

Figure 2.16: Using the reconstructed momentum of the particle and its timing one can distinguish between different particle hypothesis. The bands correspond to e^+, π^+, K^+, and proton.

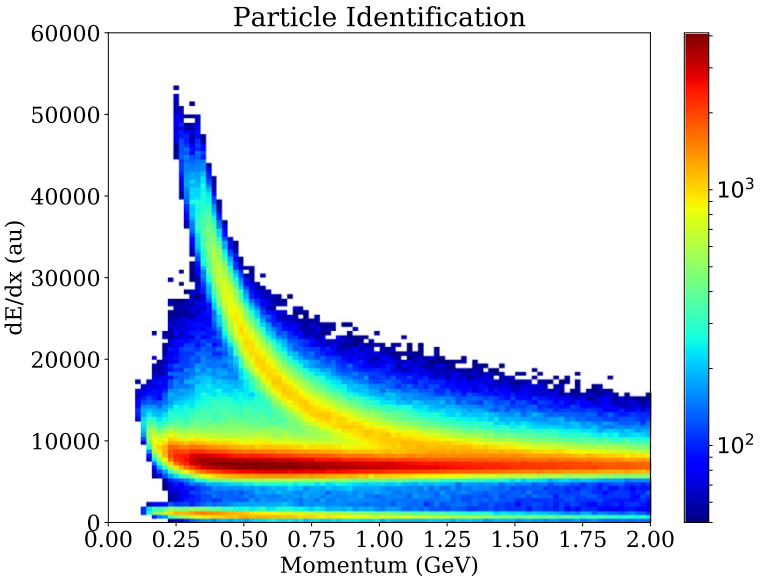

Figure 2.17: The energy deposited in the detector as a function of the momentum helps with particle identification. The curved band comes from protons while the horizontal comes from other charge particles.

2.3.3 Electromagnetic Detectors

Barrel Calorimeter. The Barrel Calorimeter (BCAL), as the name implies, is a barrel shaped electromagnetic calorimeter that surrounds the CDC. It can detect photons from 0° to

360° in the azimuthal angle and between 11° and 126° for the polar angle. The smallest shower energy that it can detect is 0.05 GeV. It is made with lead and scintillating fibers in a matrix, with the fibers running parallel to beam line. The BCAL is broken down into 48 optically isolated modules. Each module has 185 lead sheet layers and 15,000 fibers. Light produced by the fibers is transported through light guides to silicon photomultipliers (SiPMs). These are located at the end of each module.

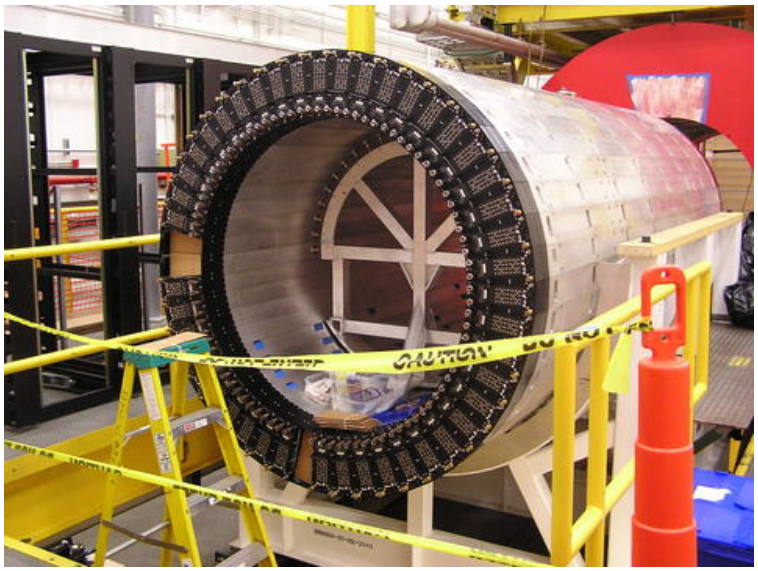

Figure 2.18: BCAL in Hall D before installation

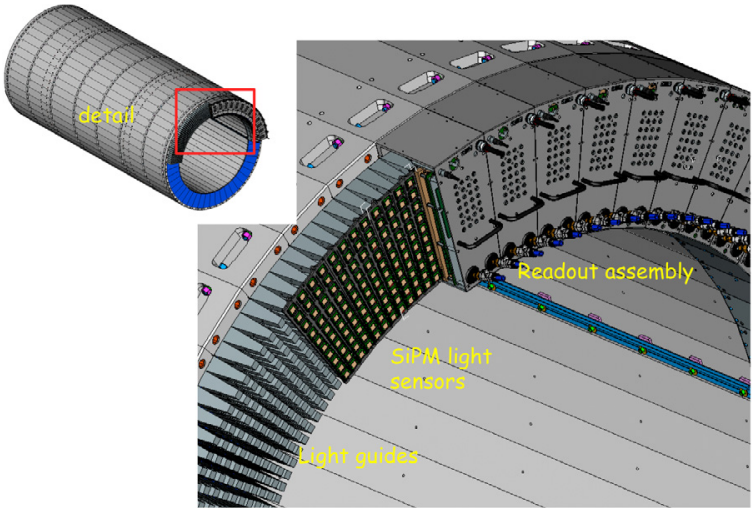

Figure 2.19: BCAL diagram showing details of the readout assembly.

Forward Calorimeter. The Forward Calorimeter (FCAL) is at the end of the GlueX spectrometer. It can read showers with energies starting at 0.1 GeV. The FCAL can detect photons with polar angles between 1° to 11°. It consists of 2,800 lead glass blocks stacked in a circular array. The blocks and most of the photo-multipliers (PMTs) come from either the E852 experiment at Brookhaven National Laboratory or the RadPhi Experiment at JLab.

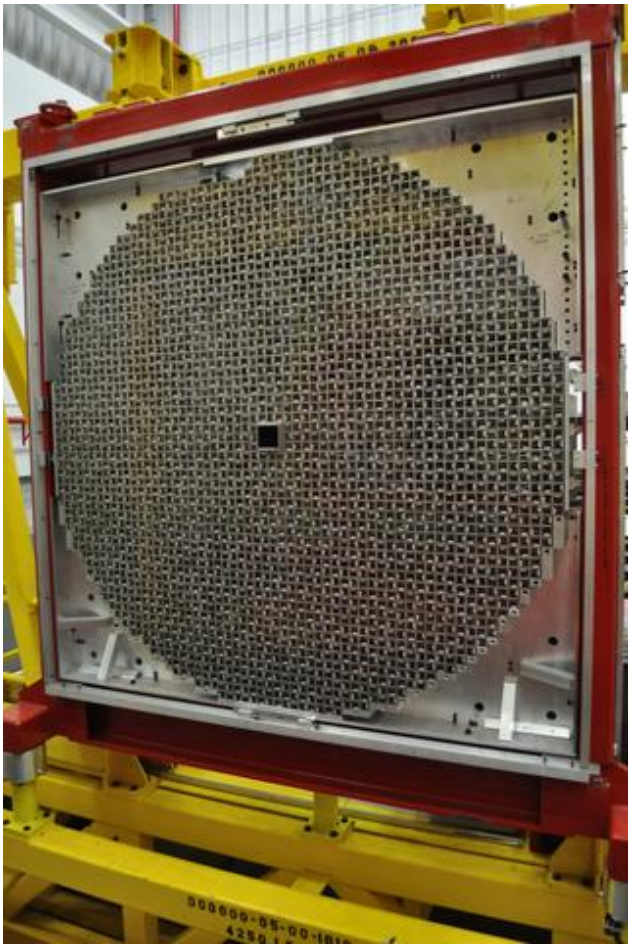

Figure 2.20: FCAL in Hall D front view.

2.3.4 Scintillation Detectors

The last two detectors are used mainly for calculating the time of flight of particles. The Start Counter provides the initial time a particle leaves the target; the Time-of-Flight detector provides the end time. These detectors can also be used to calculate energy loss of particles.

Start Counter. The Start Counter (ST) encloses the target and detects particles within 90% of the solid angle from the target. It made of 30 scintillator paddles in the shape of a cylinder. The

paddles are bent at the end to form with a pointed head, and wrapped in Tedlar to prevent light from escaping them. SiPMs are also used here to detect photons that traveled through the paddles. The ST was build to operate at photon beam intensities of about 10^8 photons per second. The timing that the ST provides is independent of the particle type and trajectory. Its time resolution is able to match the photon beam with the electron beam bunch it was originated.

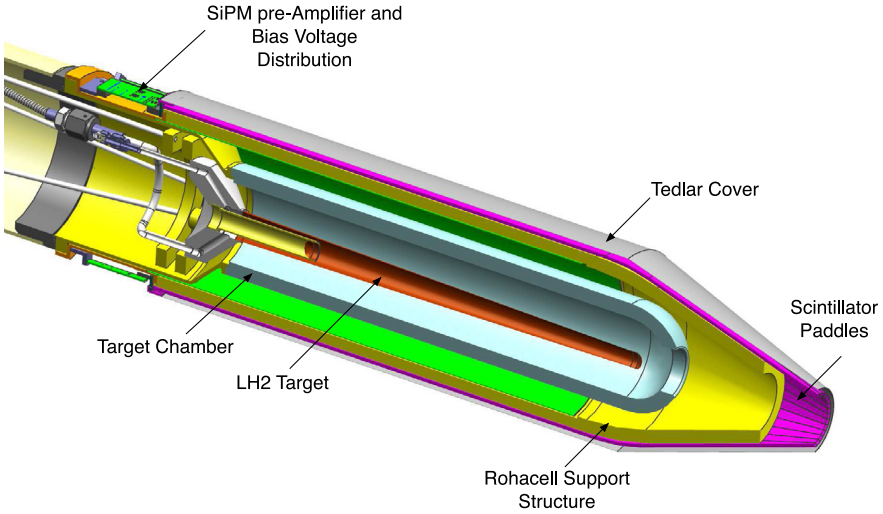

Figure 2.21: Diagram showing the different components of the ST.

Time-of-Flight. The Time-of-Flight (TOF) detector was built at Florida State University. It is located 5.5 m ahead from the target. It can detect charge particles between the polar angle 0.6° and 13°. The detector has two planes of scintillator paddles; one plane stacks the paddles vertically and the other horizontally. At the center of each plane there are four shorter paddles to accommodate an aperture for the beam. Furthermore, to keep count rates lower than 2 MHz, the two full-length paddles closest to the beam aperture have their width cut in half. Plastic light guides connect the paddles with the photo multipliers (PMTs). The paddles are wrapped in a highly reflective material followed by Tedlar.

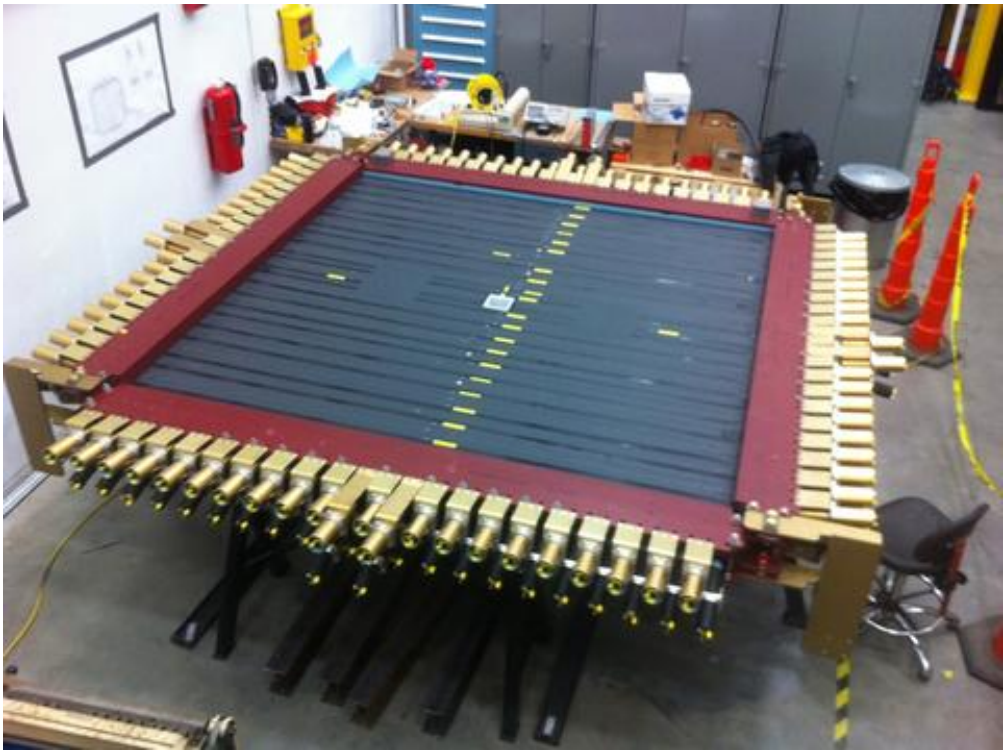

Figure 2.22: TOF in Hall D before its full installation.

2.3.5 Trigger

To record the interactions of particles with the detector, GlueX uses a criterion, or trigger. The trigger aims to accept high energy hadronic interactions and reduce the background coming from electromagnetic and low energy hadronic interactions. The physics trigger is based on energy deposited in the FCAL and BCAL [54]. For it to activate, the following two conditions must be met:

1. There must be energy deposited in the FCAL (EFCAL) and the sum of twice the amount of that energy plus the energy deposited in the BCAL (EBCAL) has to be greater than 1 GeV: $2 \times EFCAL + EBCAL > 1$
2. The energy of the BCAL has to be greater than 1.2 GeV

The first condition uses the knowledge that most physics events are expected to be produced with a forward momentum, while the second aims to take into account events with large transverse momentum. Other triggers that use the information from other detectors, such as the ST or TOF, can also be used. In addition, the PS is used as trigger for the photon flux. This trigger requires a hit coincidence on the two arms of the PS.

2.3.6 Data Acquisition

GlueX collected at a rate between 500-900 MB/s using the CEBAF Data Acquisition (CODA) frame work. This frame work encompasses a set of application an libraries that allows for customized data acquisition systems (DAQ) [21]. The GlueX DAQ has standard live time between 92-100% time; in other words it is recording events most of the time.

2.3.7 Simulations

GlueX simulation packages for the spectrometer are based on GEANT software[14][1][20]. The simulation software uses the geometrical definitions and magnetic field maps used during reconstruction. The framework supports a plethora of event generators. Inputs should specify a particular reaction to be simulated. This vertex is chosen randomly to be along the target and given a timing matching the beam timing. The rest of the simulation process uses the following steps:

1. Events are generated through one of many generators in the GlueX library [8].
2. The events are used as input in the GEANT software to simulate how they will interact with the different GlueX detectors. This stage uses information from the conditions during the real data collection.
3. The output of the previous step is processed by *mcsmear*. This software, maintained by the GlueX collaboration, applies corrections that take into account the detectors' inefficiencies and resolution. It also add hits from uncorrelated background events.

A simulation that has passed through all these three stages is considered to be a good representation of how the spectrometer would have reacted.

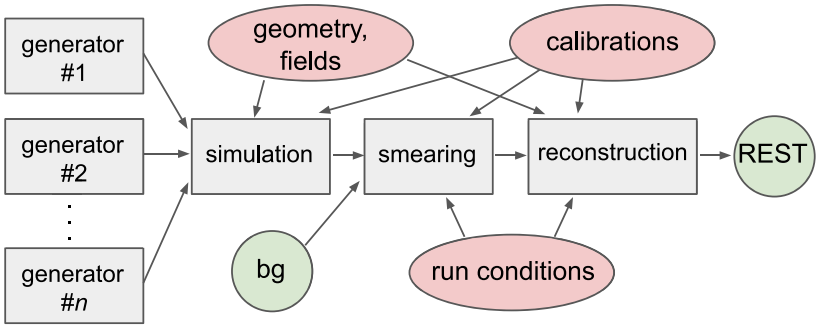

Figure 2.23: Diagram of the MC generation flow. The ovals are data bases that aid in the process. The green bg oval are real collected events used as random background triggers.

2.3.8 Kinematic Fitting

After reconstruction, most GlueX analyses will use a Kinematic Fit (KinFit) to improve the resolution of the measured data. Moreover, this tool also helps as a figure of merit to distinguish between different reactions. This is thanks to the improvement made in the final state particles for exclusive reactions, given that the details of the initial state are very well measured. The confidence level or the χ^2 are used to determine the quality of the fit. These two quantities have a one to one relationship. The χ^2 is calculated by comparing the measured and fitted vectors:

$$\chi^2 = \epsilon^T \hat{V}^{-1} \epsilon + \lambda F \tag{2.3}$$

where $\epsilon = \vec{x}_{fit} - \vec{x}_{measured}$ and $\vec{x}$ is a three dimensional vector containing the momentum components of the particle. Lagrange multipliers are added to better address the underlying physics. If there is a good agreement between the hypothesis used in the KinFit and the data, then the χ^2 is small. A large χ^2 could be caused caused by background events or poorly measured events. The performance of the fits can be studied by looking at the "pull distributions" of the variables. These distributions compare the measured value and its uncertainties to those obtained from the KinFit. For fits performed properly, and assuming that the parameters of the reconstructed particles are Gaussian, the pull values will also have a Gaussian distribution centred at 0 with $\sigma = 1$. Distributions with an offset may have a bias on the measurements or the fit. If the covariance matrix for the parameters is not estimated properly, then σ will be different from 1.

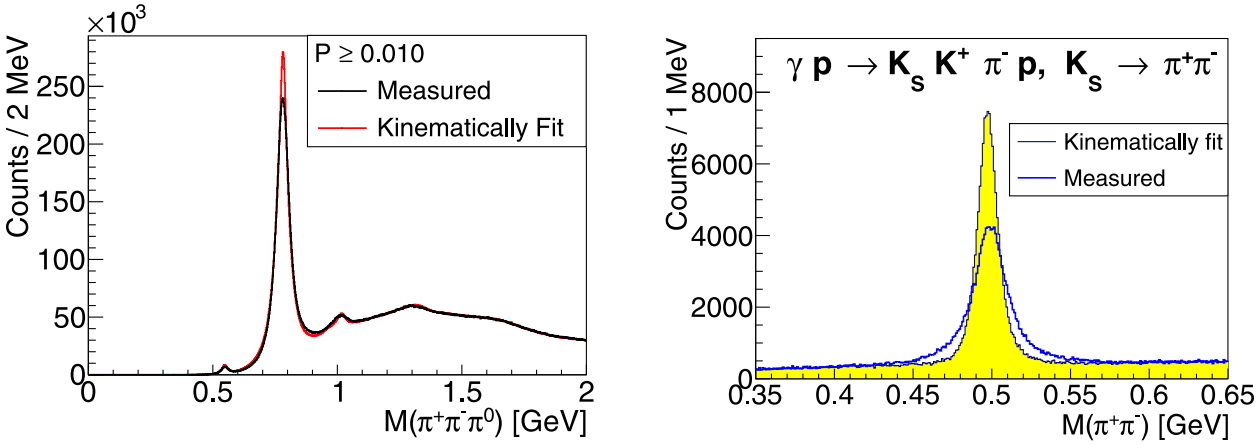

Figure 2.24: Plots showing the improvement in the resolution when using kinematic fitted vectors.

2.3.9 Overall Detector Resolution

This section summarizes the resolution of the detector. The energy resolution for beam photons around the coherent peak, 8-9 GeV, is ∼0.1%; their degree polarization is known up to 1%. For the momentum of charge particles the resolution is 1-3%. It changes for very forward high momentum particles to a resolution of 8-9%. Protons with a momenta below 250 MeV are not detected, as they are absorbed withing the target. It is challenging to reconstruct pion with momenta under 200 MeV becasue of their spiral trajectories. Nonetheless, pions and protons can be separated by the energy deposited in the CDC up to energies ∼800 MeV. In the case of pions and kaons, they can be separated by the TOF up to energies ∼2 GeV. Typical energy resolution for photons is 5-6%/$\sqrt{E_\gamma}$. The FCAL can detect photons with energies greater than 100 MeV. While the BCAL can detect photons with energies greter than 60 MeV. There is a gap between these two calorimeters around 11° where energy can be lost due to shower leakage.

2.3.10 Summary Phase I

GlueX Phase I recorded 1400 data runs for physics study. In terms of disk space, this corresponds to about 3 petabytes. The experiment had a photon flux of 2×10^7 photons/s in the coherent peak. It accumulated 121.5 pb^{-1} in the coherent peak and 319.4 pb^{-1} for energies greater than 8.1 GeV. Two sets of orthogonal linear polarization for the photon beam were used. The first pair corresponds to 0° and 90°, while the second pair corresponds to 45° and 135°. These orientations were defined by the diamond crystal oriantation with respect to the inicident electron beam. Each orientation corresponds to approximately 23% of the data taken. The rest of the data came from unpolarized photons.

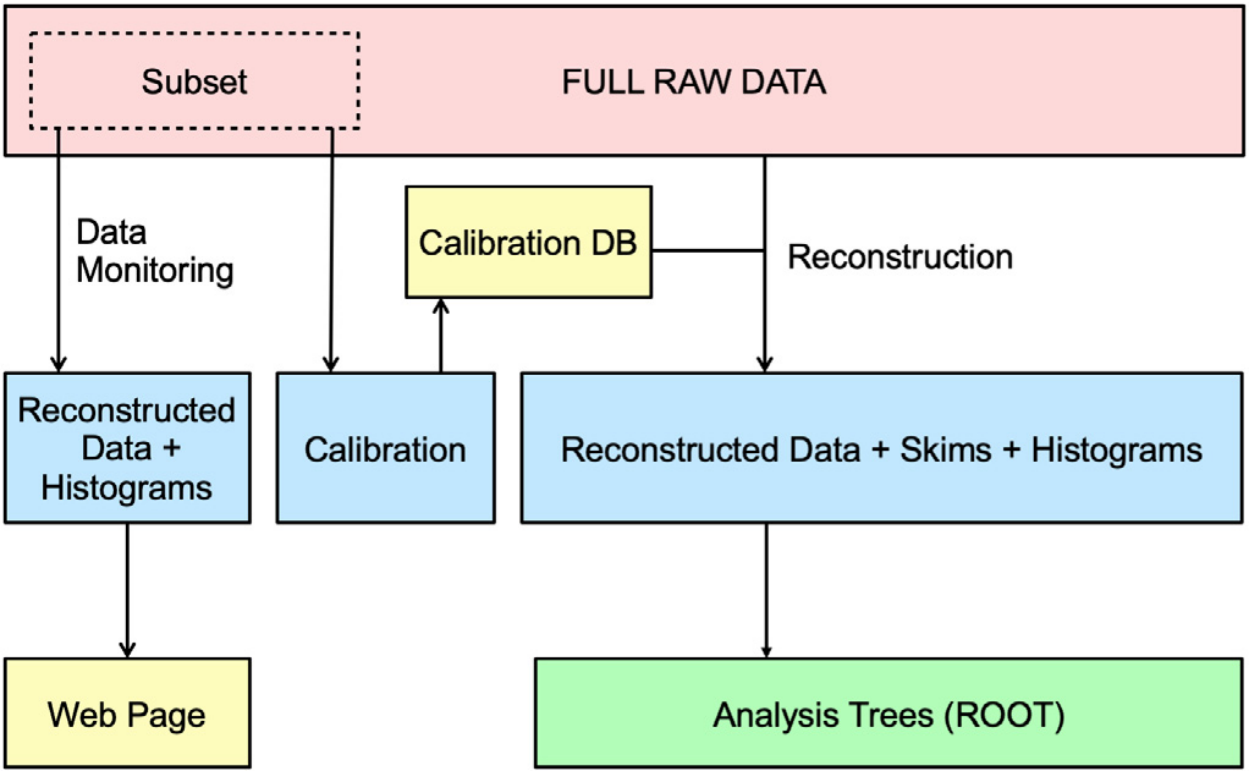

Figure 2.25: Flow of the data taking in GlueX.

CHAPTER 3

EVENT SELECTION

The analysis begins with processed data, in ROOT TTree format, for the reaction $\gamma p \to \pi^+\pi^-\pi^0\eta p$. The π^0 and η decay to two photons. The KinFit used for this reaction include four-momentum conservation, vertex, and uses a mass constraint on the π^0. This was decided after noticing the π^0 candidates of the final $\omega\eta$ events had almost no background in them Fig. 3.1. The trees contain general collaboration standard cuts that are meant to reduce background and disk space [9]. Nonetheless, other data selections are necessary to properly identify events that have the properties of the reaction of interest. The selection process will be described in different stages. At each stage a group of cuts or a single significant cut will be applied. Arguments are provided to justify the selection for the stage and include relevant plots.

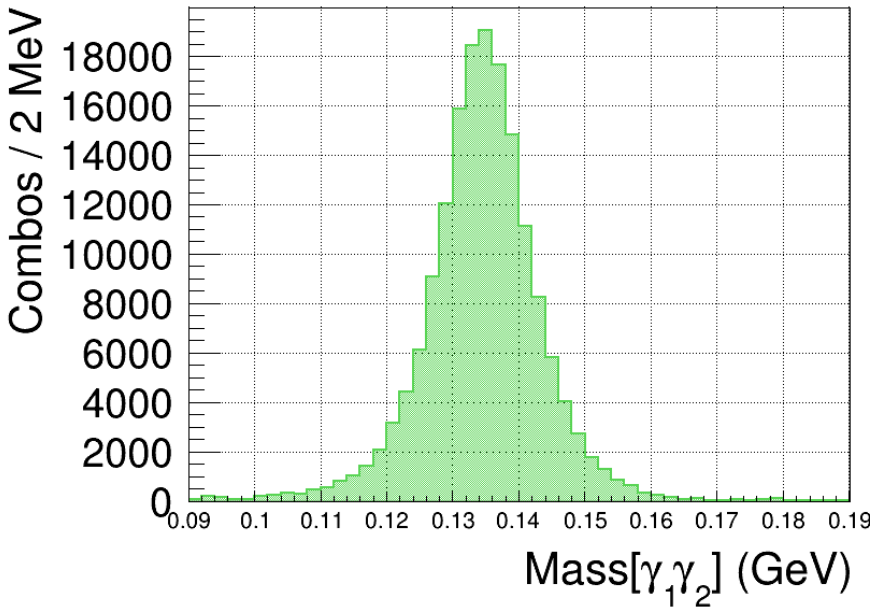

Figure 3.1: Mass distribution for π^0 once all data selection, including sideband subtraction was performed. Since there is not a noticeable background, it was decided to constraint the mass to the PDG value.

3.1 Collaboration Accepted Selection and Lose Selections

The first set of cuts is composed of a cut on the confidence level (CL), measured recoiled proton vertex, and shower quality factor in the FCAL. This group is a good starting point because they are either loose and can be optimized, or they are standard cuts across the collaboration. The CL cut is necessary since events removed are predominately badly reconstructed events or events that do not originate from the reaction of interest. The cut throws away more than half of the events Fig. 3.2. To confirm the cut does not throws more than necessary, the CL cut is optimized after the final particles are selected. The recoiled proton vertex cut selects events within the length of the target Fig. 3.3. It also avoids the target's edges that can be challenging to simulate. Lastly, the cut on the FCAL shower quality factor keeps events where there is a moderate confidence that the electromagnetic showers come from photons, as opposed to background Fig. 3.4 [3].

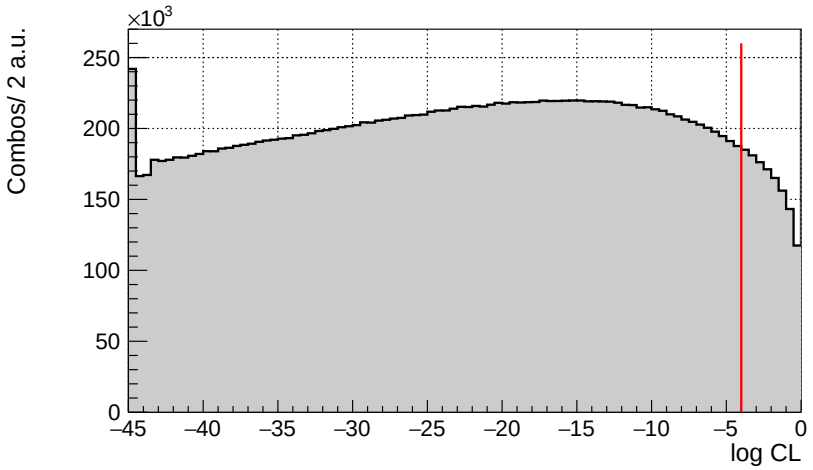

Figure 3.2: The red line shows the value of the CL cut. This value is optimized later.

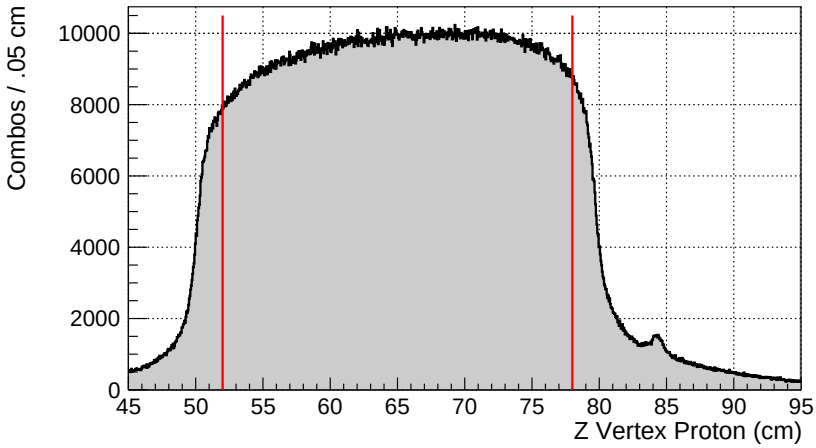

Figure 3.3: Avoiding the edges of the target imrpoves agreement with MC since the edges are not well simulated. The accepted events lie within the red lines.

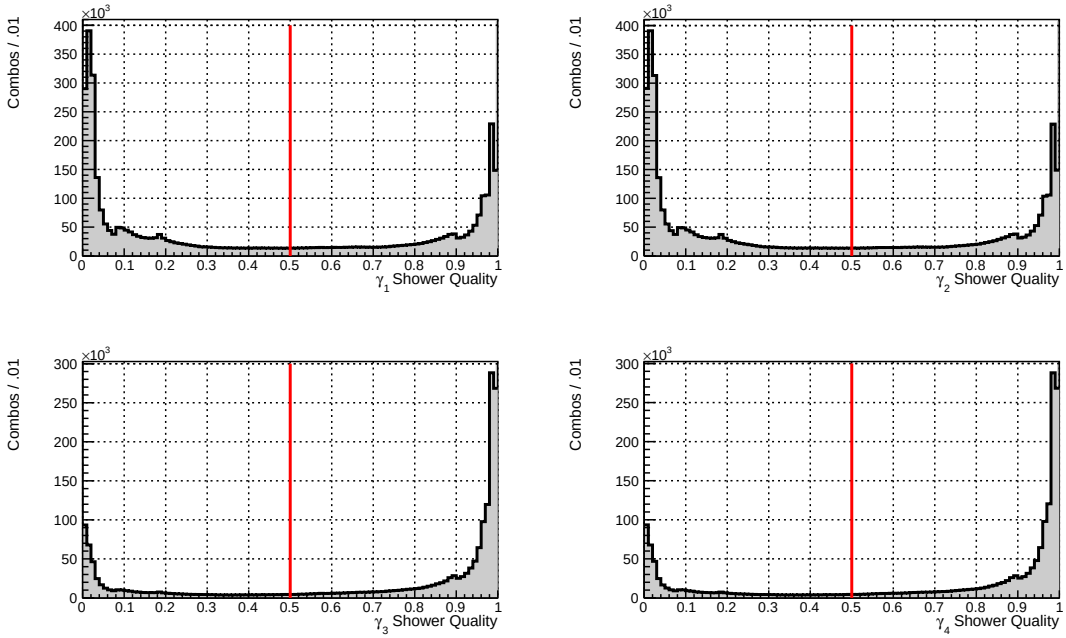

Figure 3.4: The shower quality help select showers with a higher confidence that they come from photons. The events on the right side of the distributions were kept.

3.2 Selecting Prompt Beam Bunch

At this stage, the data is separated into two sets based on the beam timing. The division separates combinations coming from in-time beam candidates as they tend to have different distributions from the ones coming from out-of-time beam candidates Fig. 3.6. The beam candidates within 2 ns from 0 are considered to be in-time; beam candidates that are farther than 6 ns away are used to study accidentals. The peaks adjacent to the in-time peak Fig. 3.5 are skipped as they can affect the study of accidentals. The beam accidental subtraction and other statistical methods for background removal will be discussed in a different section. The data plots shown here and onward will contain only in-time beam candidates unless otherwise mentioned.

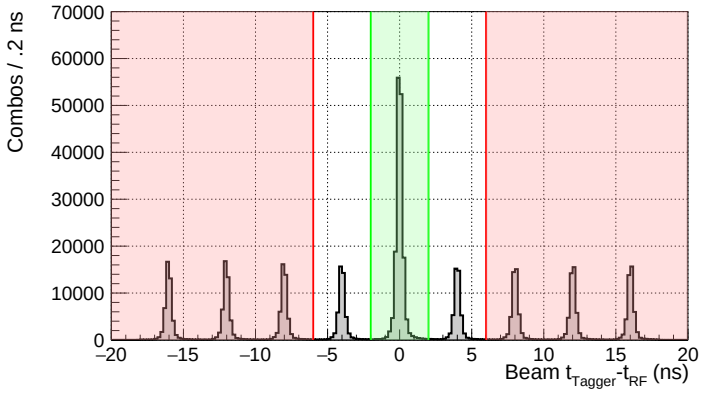

Figure 3.5: The in-time events are those in the green area, while the off-time events are in the red. The off-time events give a good estimate of how many accidentals are within the in-time peak.

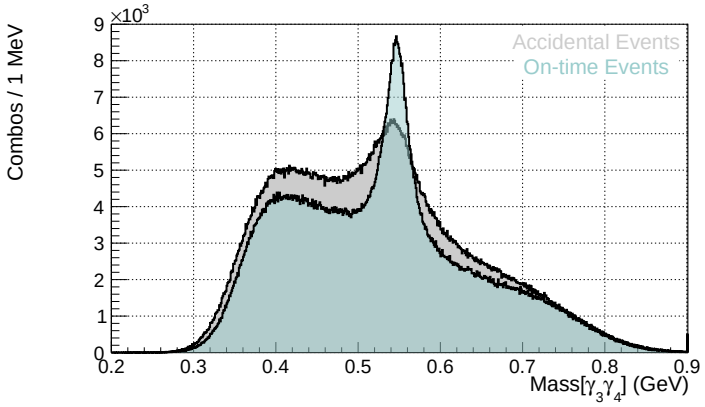

Figure 3.6: The mass distribution of the photon candidates for π^0 ($\gamma_1\gamma_2$) and η ($\gamma_3\gamma_4$) show different characteristics depending their beam timing.

3.3 Elimination of Reactions Contaminating Data

One of the biggest backgrounds in this data sample comes from events with two π^0. The data already includes a mass selection for π^0 and η candidates [9]. This means that a pair of photons that lies within the mass window, becomes a candidate for this particle. Looking at the off-candidate photons allows for the investigation of the two π^0. In other words, these combinations are formed by pairing a photon from a π^0 candidate with a photon from an η candidate. The goal is to veto combinations where the off-candidate photons overlap in the mass of the π^0. While there are a few states that produce this background, one of the more noticeable is the b_1 (Fig. 3.11). The veto area was calculated in two steps. First, an unbinned fit is performed to the mass distribution from off-candidate photon distributions, in the range between .09 GeV and .19 GeV Fig. 3.9. The fit used 2 Gaussian and a Chebyshev polynomial function for background. Then, an elliptical region, using the standard deviations, is calculated from the previous step as the radii. All the events that fall within the elliptical region get vetoed from the analysis Fig. 3.8. The signal to background ratio for the η, the figure-of-merit (FOM) for this cut, helped optimize the region of the veto. The η is particularly insightful since it is greatly affected by this background. Moreover, it is good to use the η as a discriminator since the signal peak should be minimally affected by a good veto. To calculate this ratio, an unbinned fit of the η candidates in the range 0.4 GeV - 0.75 GeV was performed. This fit used two Gaussians and a Bernstein polynomial function. Different values of σ for the value of the ellipse's radii were tested for this veto Fig. 3.10. The value of 3σ for the

radii was chosen for the cut based on the FOM Table 3.1. After applying this veto, ∼35% of the coombinations were lost and the b_1 events are practically gone Figs. 3.11 to 3.12. Note: a window matching the measured mass selection was used for η candidates that have the kinematically fitted vectors to allow for a smoother fitting Fig. 3.7.

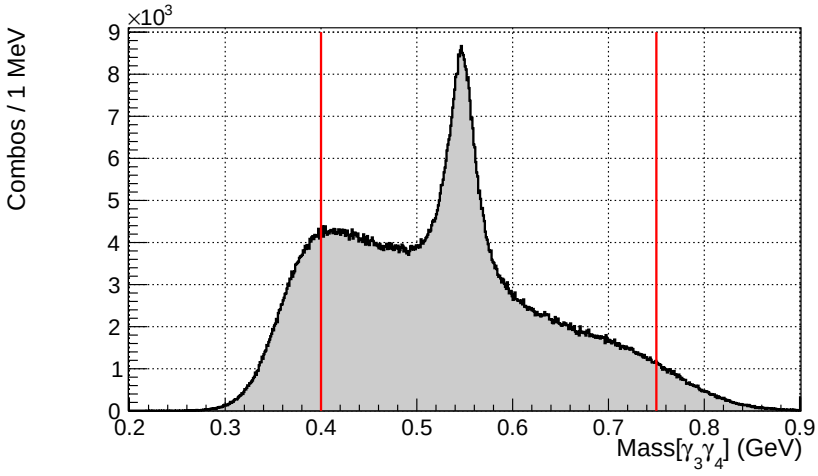

Figure 3.7: The kinematic fitted 4-vectors of the photons candidates have a selections that will allow help fit a background distribution better. The cut aims to get rid of the edge effects created by the kinematic fit.

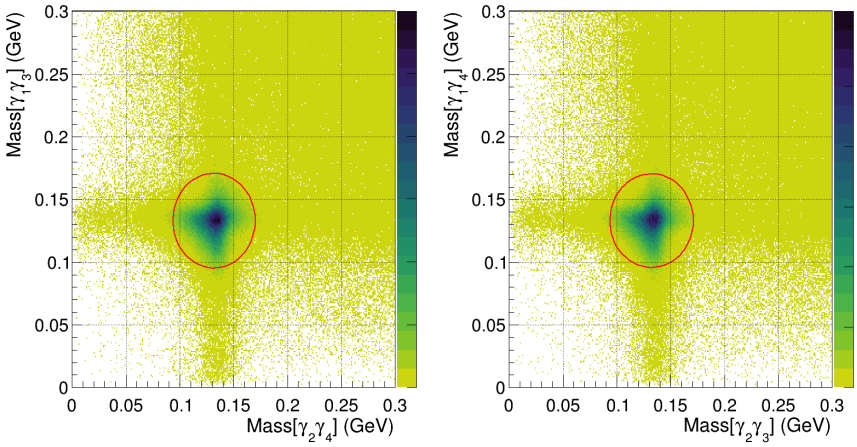

Figure 3.8: The plots show a high concentration of $\pi^0\pi^0$ events. The red line encompassing these events is the ellipse calculated with the values from the fits.

Table 3.1: The FOM Sig/Bkg changes drastically at 2σ. However, a slight improvement can be seen in lower M[$\gamma\gamma$] plot Fig. 3.10 if 3σ is used instead. There is not a big change between 3σ and 4σ

Cut	Combination Lost	Sig/Bkg
No Cut	0	.138
1σ	17.5%	.180
2σ	28.8%	.215
3σ	32.6%	.229
4σ	34.6%	.237

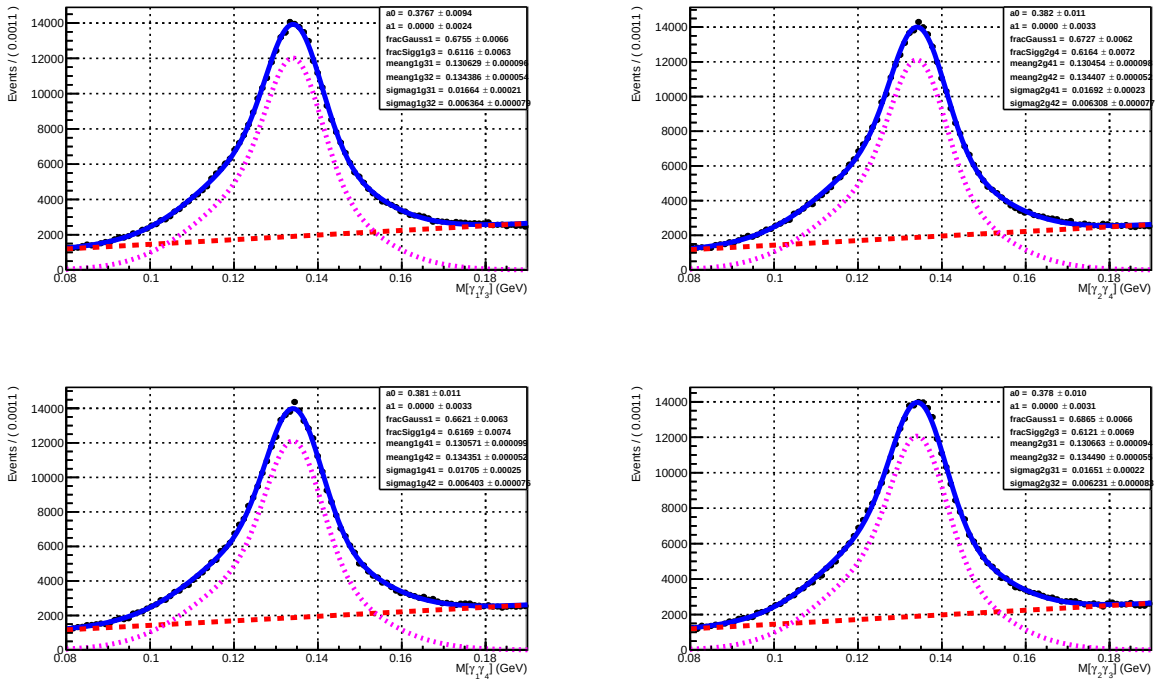

Figure 3.9: These are the fits of the off-candidate combinations. Note that the fit is only within the region where the π^0 is expected.

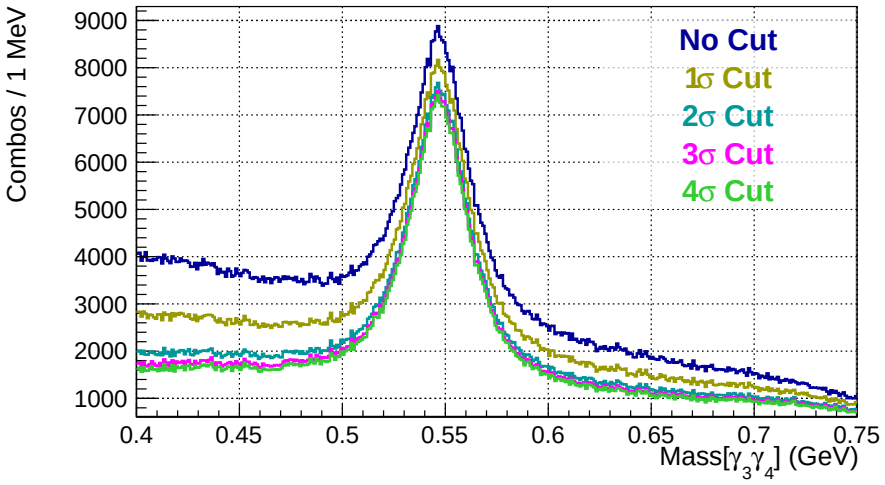

Figure 3.10: The mass distribution for η candidates changes as the radii of the ellipse increases based on the calculated σ.

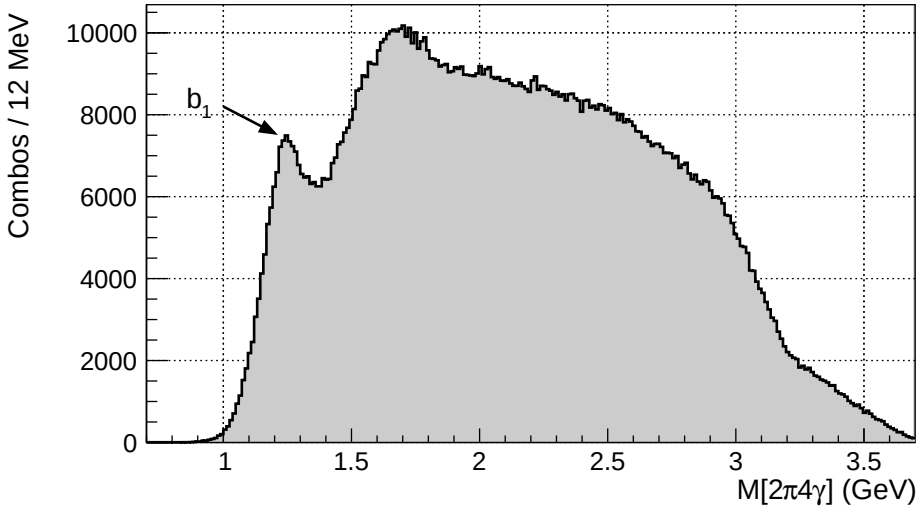

Figure 3.11: Notice the b_1 contribution. These are some of the events targeted with the $2\pi^0$ veto.

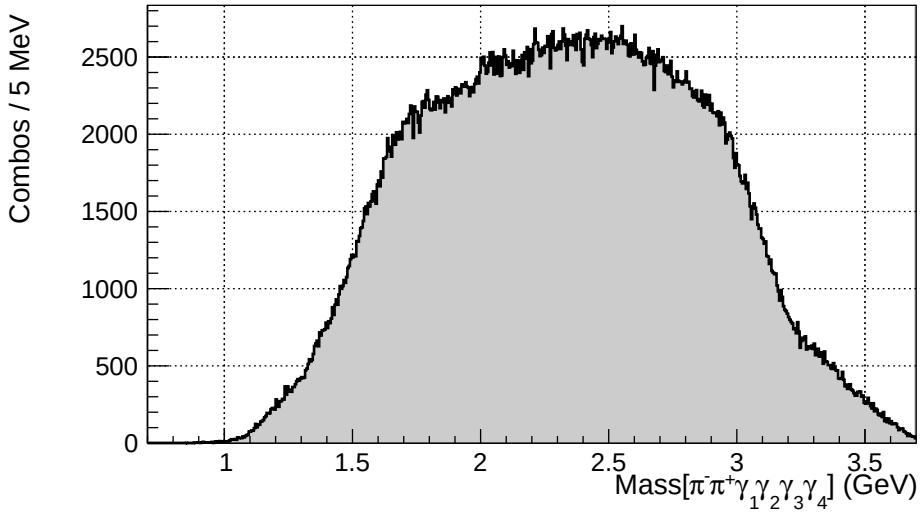

Figure 3.12: The $2\pi^0$ veto leaves no obvious sign of the b_1 events.

3.4 Selection of Phasespace

The next selection will limit the phase space of the data. First, the tails of the missing mass squared and missing energy distributions are removed. The tail events are not significant for the analysis Figs. 3.13a to 3.13b. Next, events were selected within a mass window for the three pions from .66 - .9 GeV Fig. 3.14. Since the only relevant events for this analysis contain an ω, this selection focuses on those events. The window is chosen wide enough to allow for a sideband subtraction, which will be discussed in detail later. Lastly, the beam energy was selected to be within the coherent peak (8.2 - 8.8 GeV) Fig. 3.15. The combination of these selections reduces the presence of the other resonances in this channel considerably.

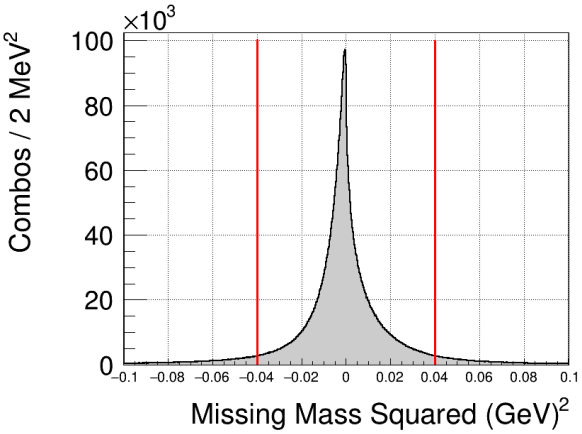

(a) This distribution uses the measured 4-vectors since the kinematic fit constraints it to 0.

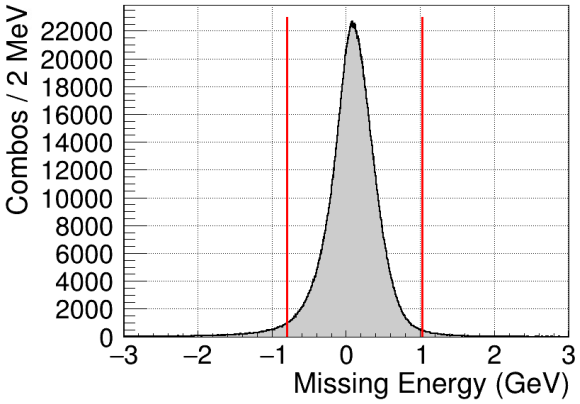

(b) This distribution is also constrained to 0 in the kinematic fit.

Figure 3.13: The tails in these distributions are removed. The shape of the missing mass squared and the missing energy are correlated to the CL selection.

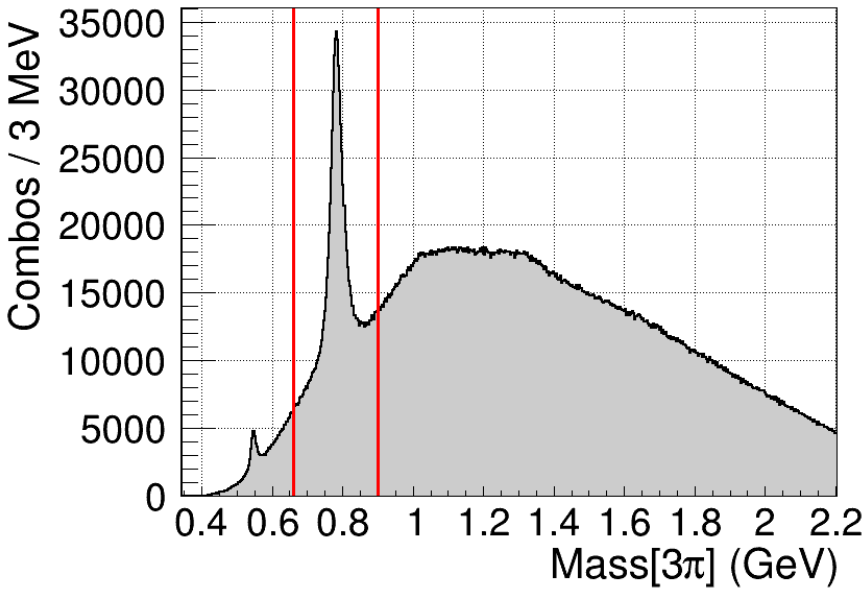

Figure 3.14: The phasespace of the reaction is reduced by focusing on 3π events within the vicinity of the ω mass.

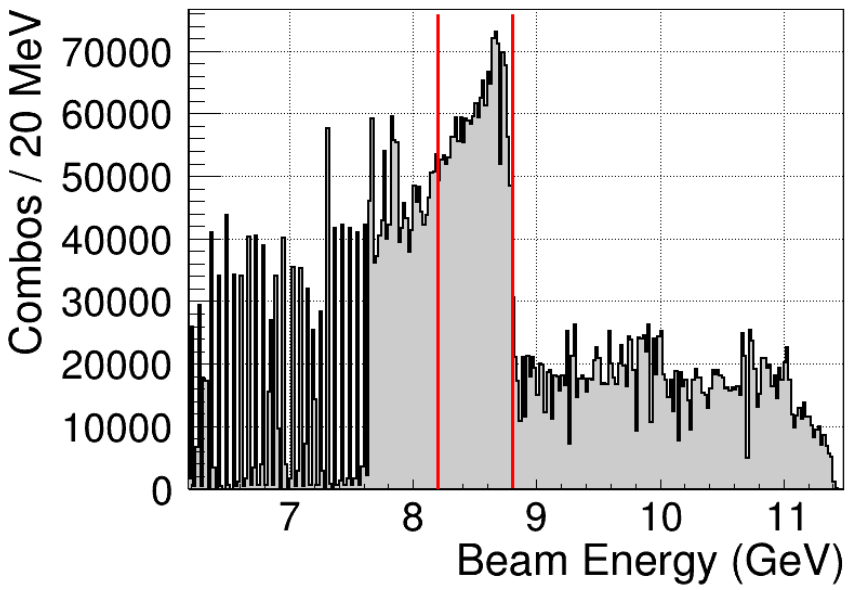

Figure 3.15: This selection withing the coherent peak ensure that the beam photons used have an average of 40% polarization.

The phasespace is further limited by selecting a region in the momentum transfer t for the $\omega\eta$ system. This selection can be particularly useful given that different reactions have slightly different t distributions. For example, meson production tends to concentrate in low t values, while baryon production is expected at higher t values. With this in mind, the optimal value for t will be search in the range between 0 and 1 GeV^2. The distributions for M[$\omega\eta$] and M[ηp] in bins of .1 GeV^2 for t were explored in this interval (Fig. 3.18). Events $t < .6$ GeV^2 (Fig. 3.21fig:metaPT) were selected as they display structure beneath 2 GeV in the M[$2\pi 4\gamma$] plot. It was also noticed that events with t $< .3$ GeV^2 show the least amount of baryonic events (Fig. 3.19).

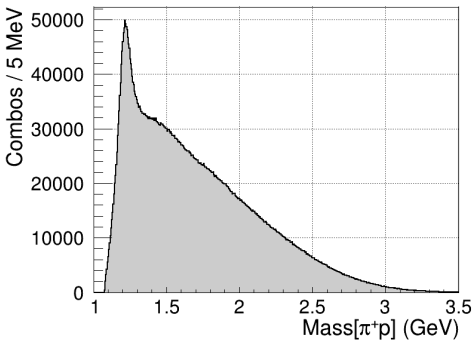

(a) A clear Δ^{++} is seen a threshold.

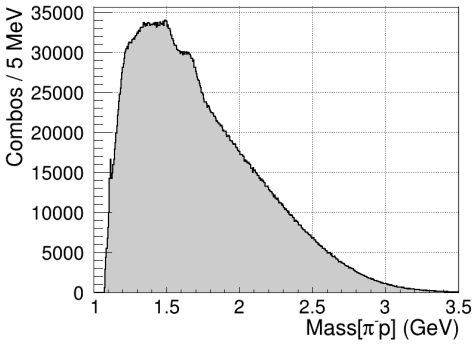

(b) While no clear peak is seen, there seems to be significant structure below 2GeV.

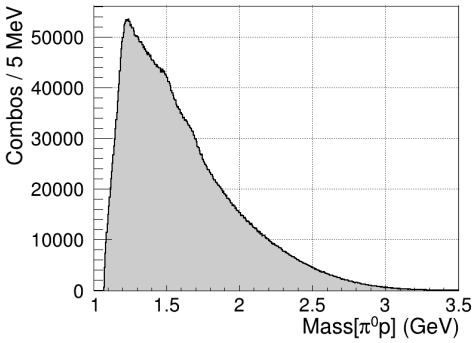

(c) A Δ^{+} seems to be present at threshold accompanied by other structures.

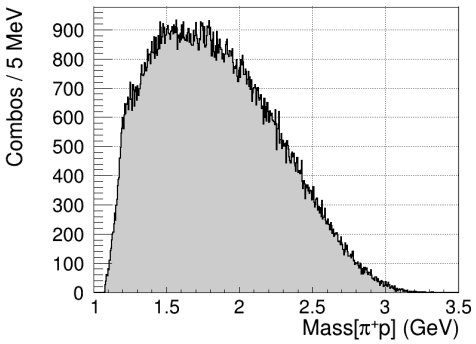

(d) The Δ^{++} contribution has almost disappeared.

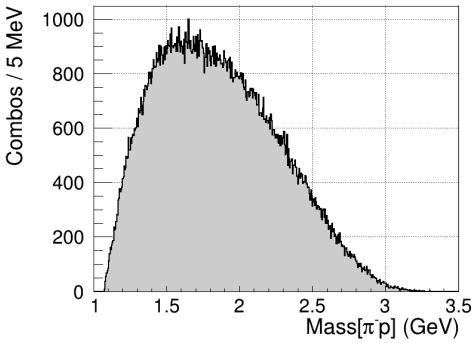

(e) The distribution has no indications of resonances structures.

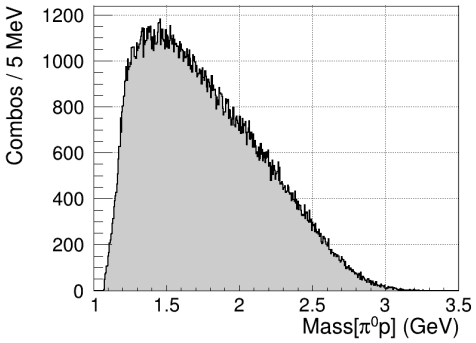

(f) No clear contribution from the Δ^{+} or the other structure is seen.

Figure 3.16: Figure on the left shows the plots where Δ particles and other baryons are expected before the phase space selection and figure on the right shows the plots after the selection.

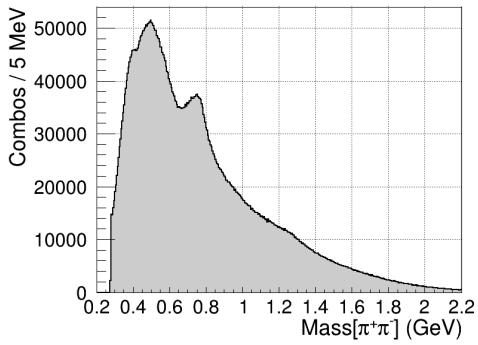

(a) A ρ peak can be seen ∼0.8 GeV.

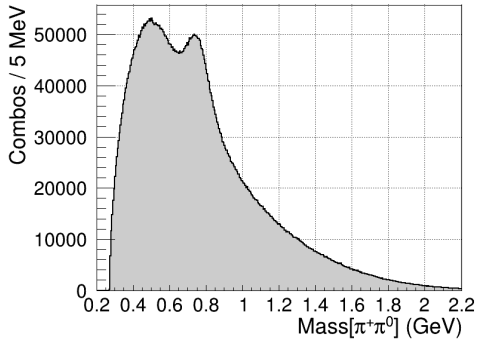

(b) A ρ peak can be seen ∼0.8 GeV.

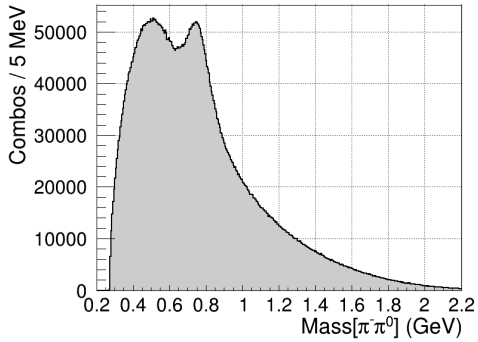

(c) A ρ peak can be seen ∼0.8 GeV.

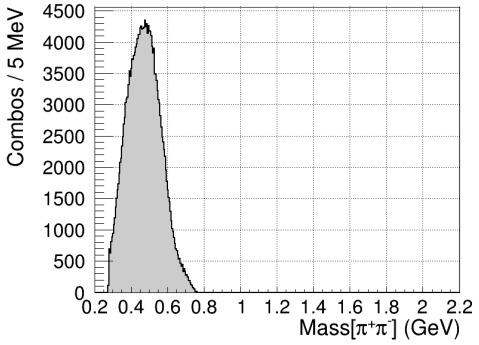

(d) Not only did the ρ is gone, but also all of the events above 0.8 GeV

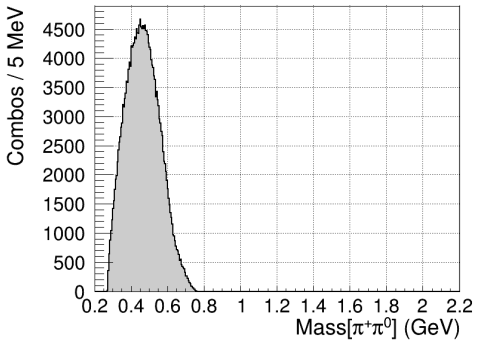

(e) Not only did the ρ is gone, but also all of the events above 0.8 GeV

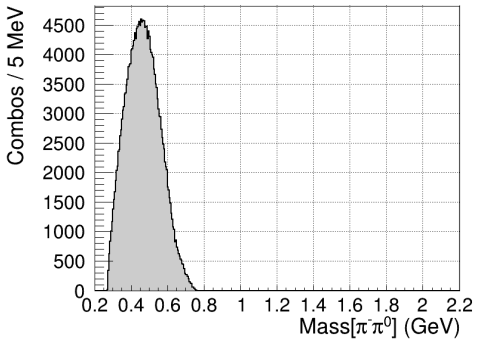

(f) Not only did the ρ is gone, but also all of the events above 0.8 GeV

Figure 3.17: Figure on the left shows the plots where ρ particles are expected before the phase space selection and figure on the right shows the plots after the selection.

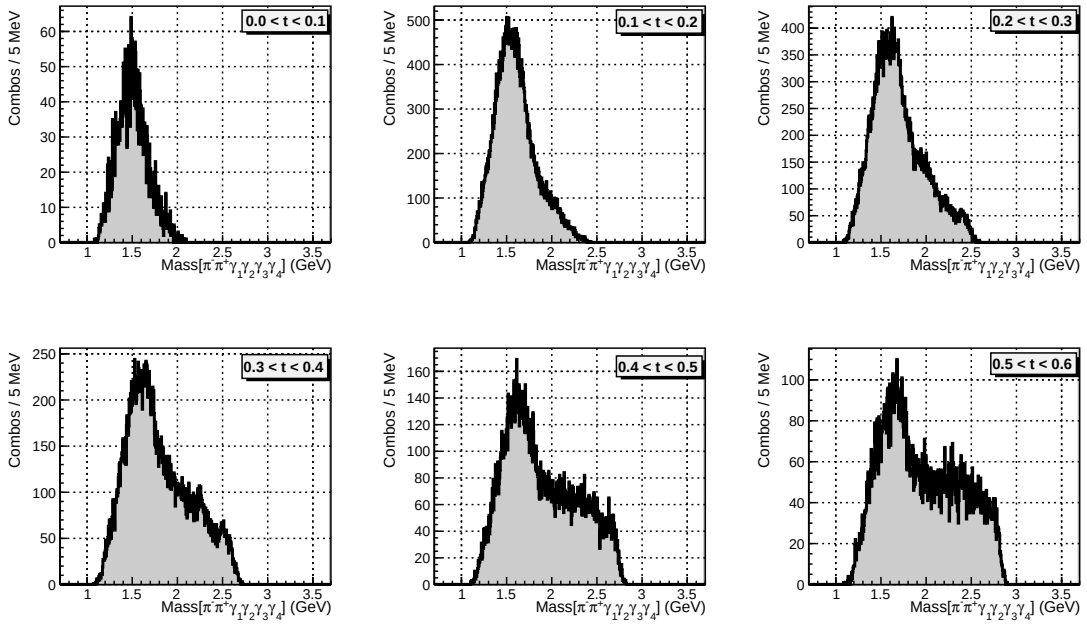

Figure 3.18: As the bins of t increase in value, the plot shows structure in the upper mass region.

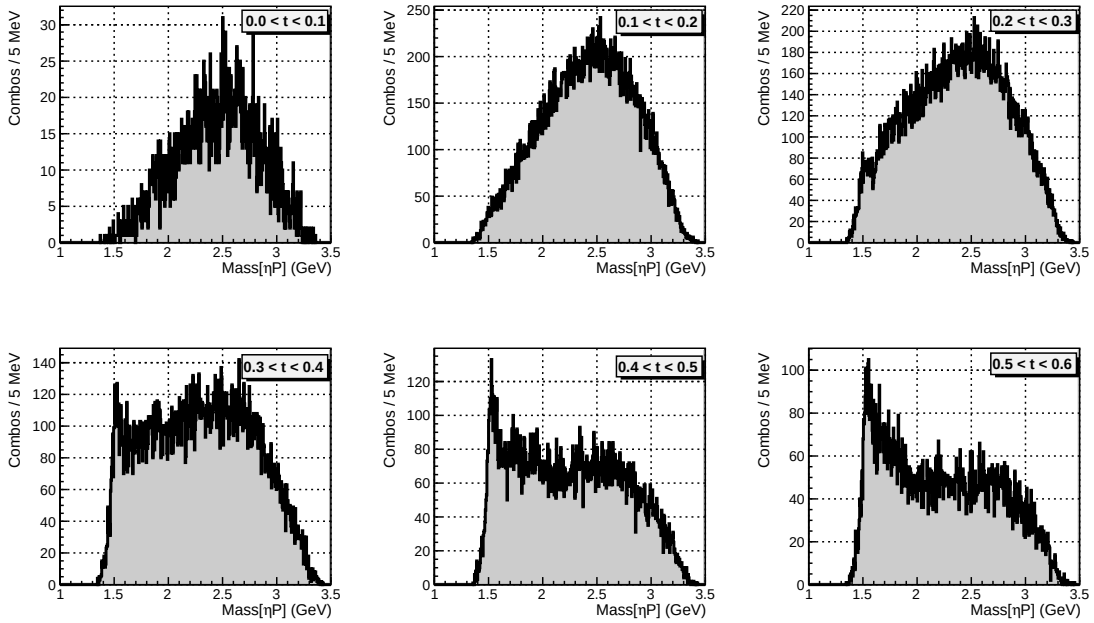

Figure 3.19: With higher t values, the N(1535) signal peak becomes clearer.

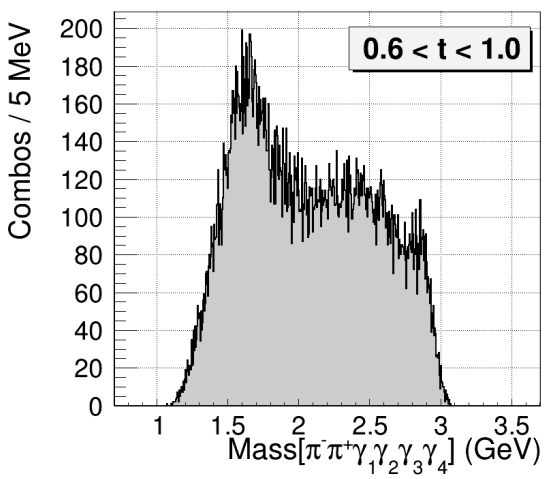

(a) The structure beneath 2 GeV is not very prominent as in other t regions.

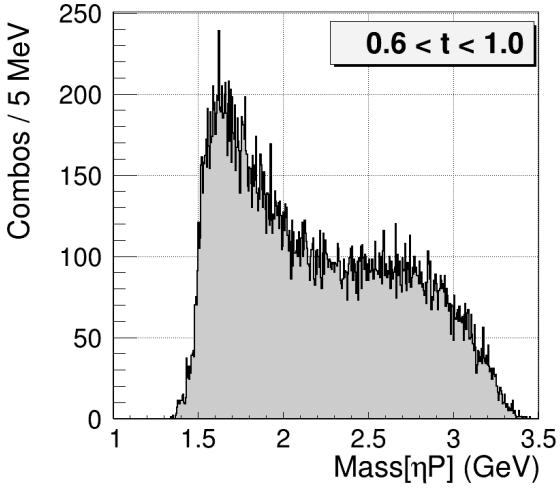

(b) The peak associated with N(1535) is the dominant structure in this t region.

Figure 3.20: Mass distribution of $\omega\eta$ (a) and ηp (b) for t between 0.6 and 1 GeV^2

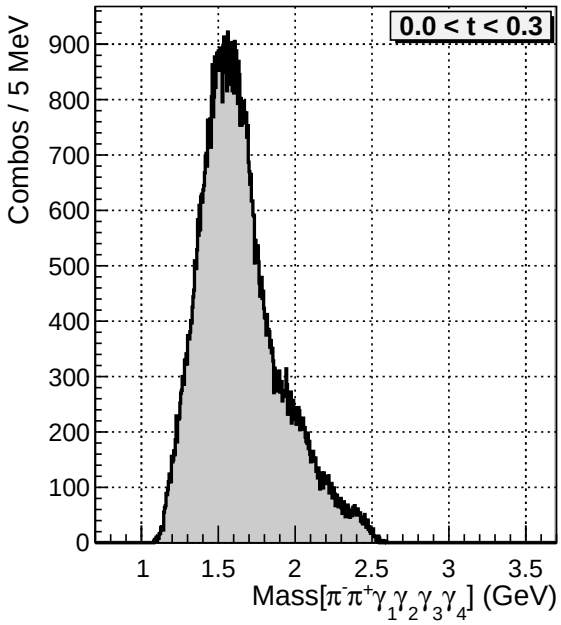

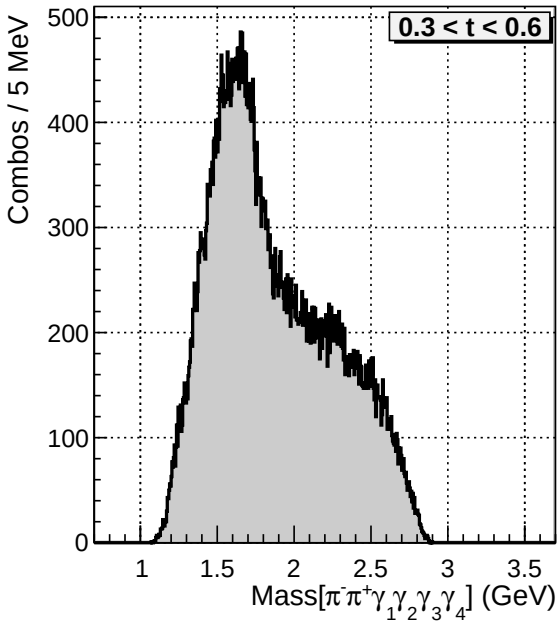

Figure 3.21: Both distributions have structure around 1.6 GeV. However, only the low t plot shows structure in the upper mass range.

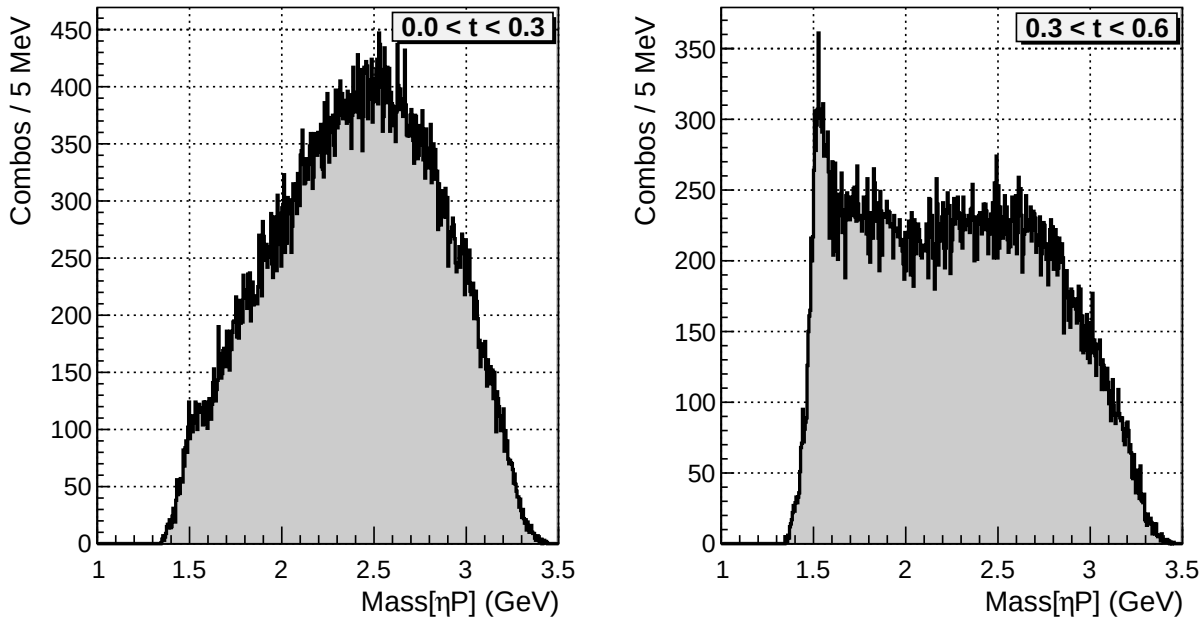

Figure 3.22: The peak associated with N(1535) is clear in the high t region and almost absent in the low t region

3.5 Fine Tuning Kinematic Fit Selection

Having reduced the phasespace, removed some of the main backgrounds, and selected a mass window for the final state particle candidates, it is time to optimize the CL value. For this exploration, all the cuts discussed so far were implemented. The exploration window consisted of different CL values. The first set of values was from 10^{-40} to 10^{-10} in steps of 10^{-10}. The subsequent range, from 10^{-10} to 10^{-1}, had smaller steps of 10^{-1} Figs. 3.23a to 3.23c. An unbinned fit for the η candidates and ω candidates was performed. There is no need to look at the π^0 candidates since the mass of the π^0 was constrained in the KinFit, meaning that all the π^0 have the same mass. Moreover, in principle, a good ω candidate should come with a good π^0. After looking at the significance as the FOM, the best for the CL cut is 10^{-3}.

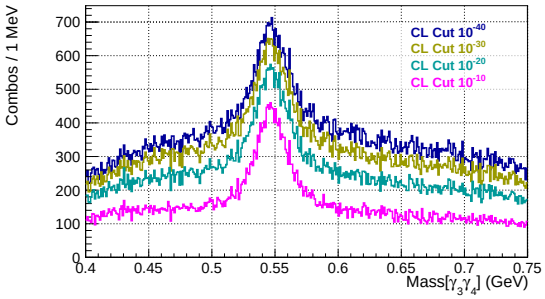

(a) Mass distribution for η candidates with upper CL cut values

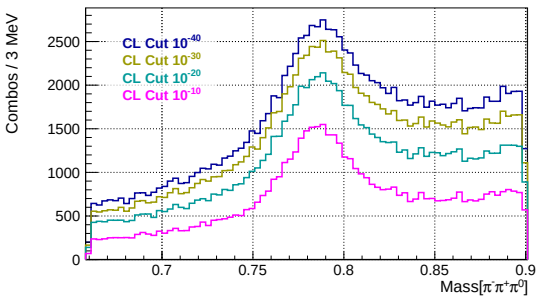

(b) Mass distribution for ω candidates with lower CL cut values

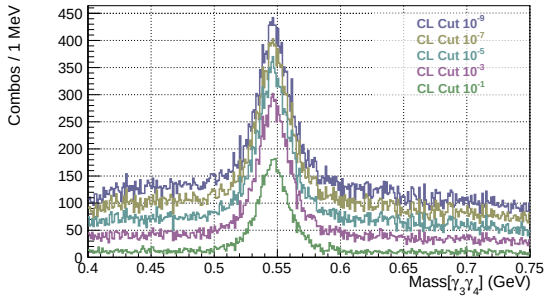

(c) Mass distribution for η candidates with upper CL cut values

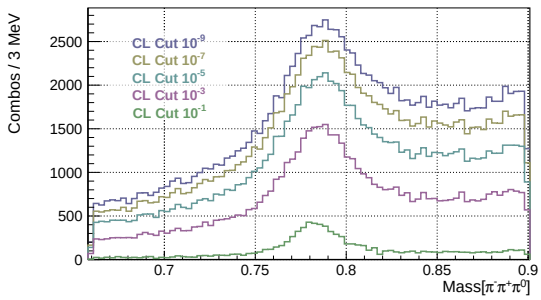

(d) Mass distribution for ω candidates with lower CL cut values

Figure 3.23: Plots show the different effect for the multiple CL selection.

Table 3.2: While there are events with a CL less than 10^{-40}, this value was chosen as the first reference point. The value chosen for the cut was 10^{-3} as it is the on with the maximum η significance.

CL Cut Value	Combination Lost	ω sig/bkg	ω Significance	η sig/bkg	η Significance
10^{-40}	0	0.4857	149.07	0.3966	110.80
10^{-30}	9.2%	0.5190	149.20	0.4345	113.40
10^{-20}	23.4%	0.5756	147.81	0.5023	116.47
10^{-10}	47.4%	0.7097	141.61	0.7018	122.93
10^{-9}	50.8%	0.7431	141.27	0.7433	123.83
10^{-8}	54.4%	0.7732	139.32	0.7872	124.11
10^{-7}	58.3%	0.8048	137.08	0.8498	125.01
10^{-6}	62.5%	0.8511	134.79	0.9339	126.12
10^{-5}	66.9%	0.9109	131.97	1.0539	127.74
10^{-4}	71.9%	0.9787	127.12	1.2370	129.55
10^{-3}	77.3%	1.0729	120.71	1.5077	130.00
10^{-2}	83.3%	1.2297	111.86	1.9749	127.97
10^{-1}	99.0%	1.4643	29.59	2.9557	36.71

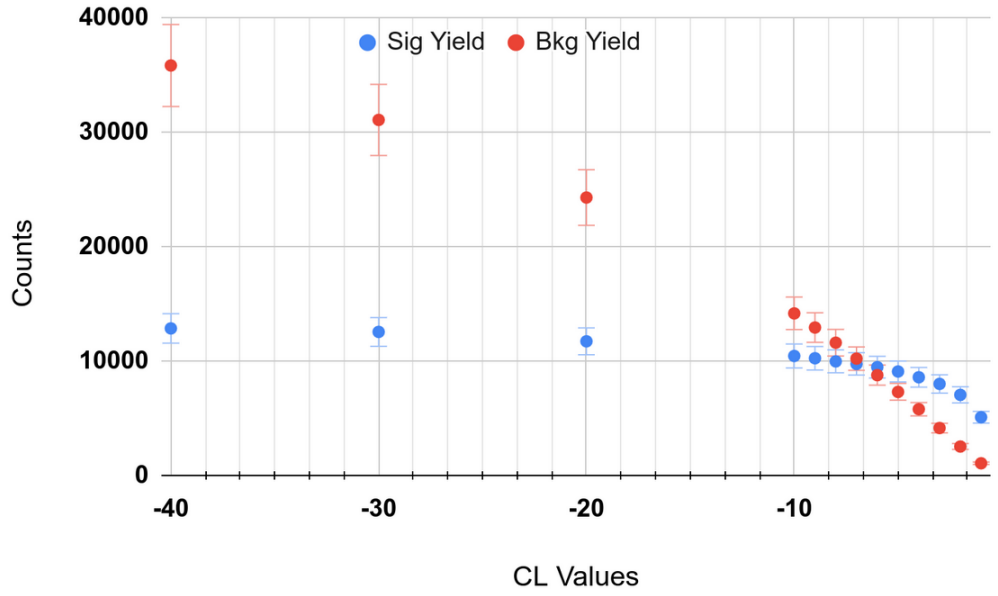

Figure 3.24: At lower CL cut values, the yield for η is not affected as much as the background yield.

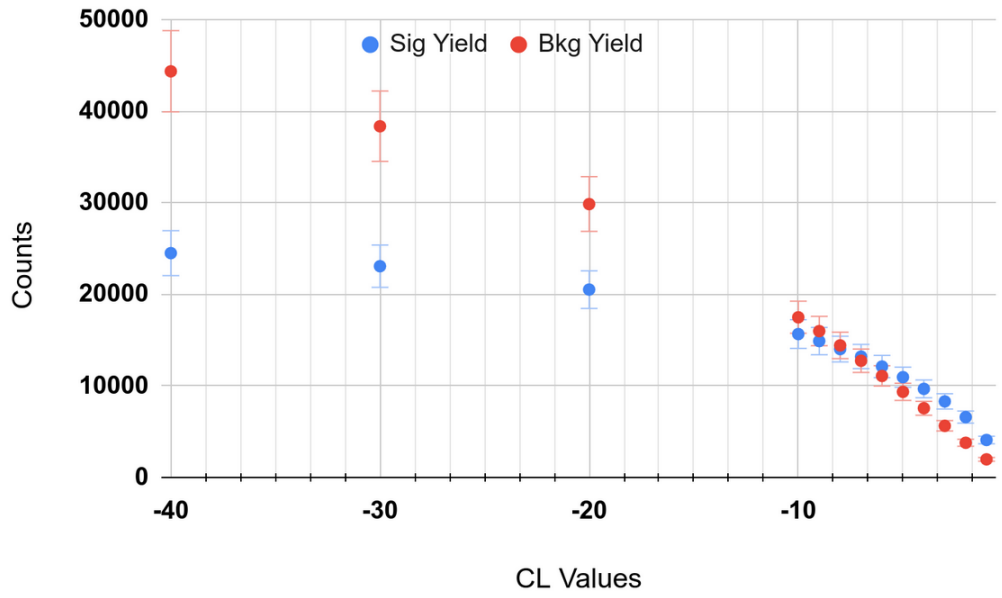

Figure 3.25: Unlike η, at low CL cut values, the ω yield changes almost as fast as the background yield.

3.6 Selecting Best Combo Candidate

There is one more step left to perform. This study aims to be an event driven analysis by selecting the best combination from each event. An event is defined by the "event number", a number provided in the Root TTree. Using different particle candidates for the event or permuting the particles within the event generates different combinations. At this stage, ∼28% of the events have more than one combination. The multiplicity comes primarily from the beam photon or a different permutation of the four final state photons Fig. 3.26. Since the KinFit used the information of the missing energy, missing mass, and the mass of π^0, it can be used to reduce the number of combinations to one. That is to say, for events with multiple combinations the combination whose CL was the highest was kept.

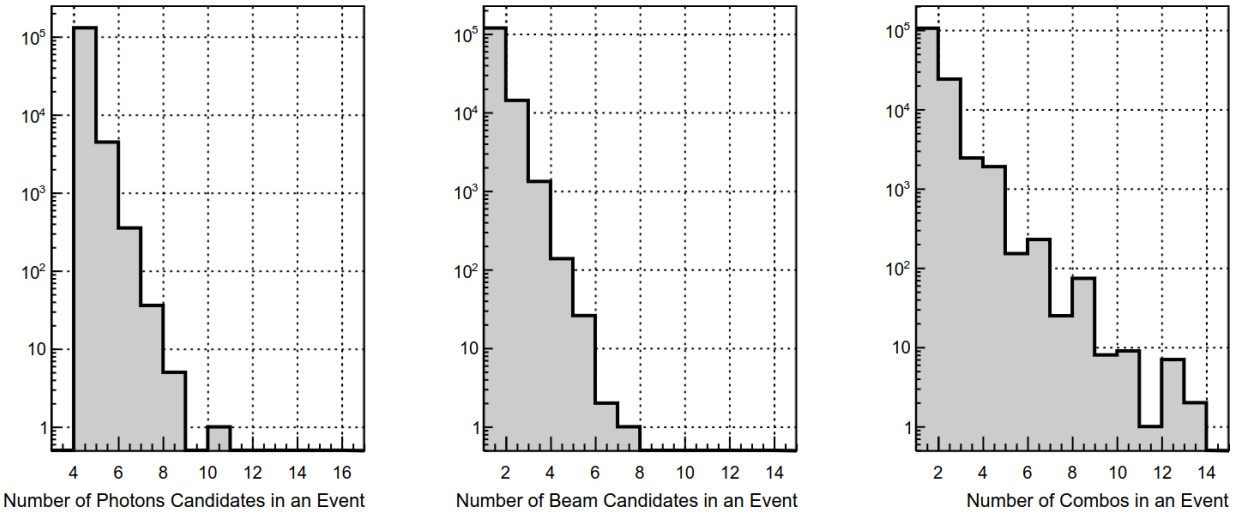

Figure 3.26: About 5% of the events have multiple photon candidates. The number of beam candidates is almost double with about 12% of events having multiple combinations.

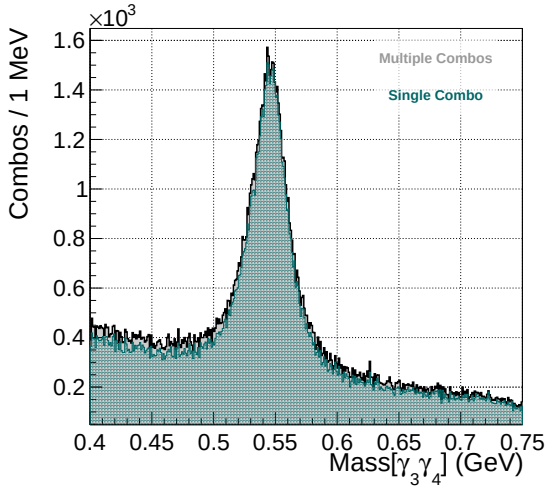

(a) The lower mass η candidates are affected the most when selecting the best combo

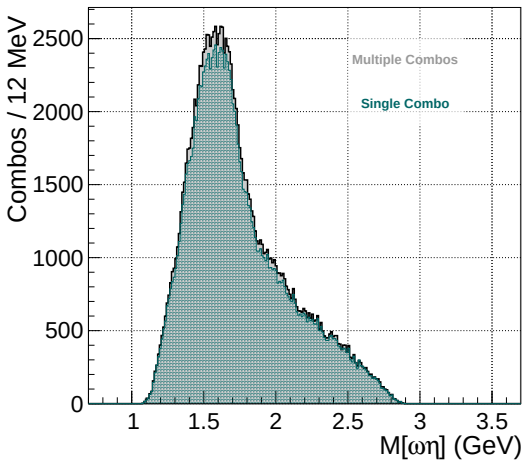

(b) The mass distribution for $\omega\eta$ does not change too much when selecting the best combo

Figure 3.27: Selecting the best combination from an event has no effect on the overall shape of the distributions.

3.7 Summary: Selection Table

Table 3.3: Table showing the different values for the data selection.

Name of the Cut	**Events Kept**
Confidence Level	CL $> 10^{-3}$
Beam Timing	$\lvert$BT$\rvert < 2$ ns
Proton z Vertex	52 cm $<$ z $<$ 78 cm
Photon Shower Quality Factor	SQ > 0.5
Missing Mass Squared	$\lvert$MMS$\rvert < 0.04$ GeV
Missing Energy	.115 - 3 (.303) GeV $<$ ME $<$ .115 + 3 (.303) GeV
Beam Energy	8.2 GeV $<$ BE $<$ 8.8 GeV
-t	-t $< .6$ GeV^2
Double π^0 (A)	$\frac{M(\gamma_1\gamma_3)^2}{(3\times.0126)^2} + \frac{M(\gamma_2\gamma_4)^2}{(3\times.0128)^2} > 1$
Double π^0 (B)	$\frac{M(\gamma_1\gamma_4)^2}{(3\times.0129)^2} + \frac{M(\gamma_2\gamma_3)^2}{(3\times.0125)^2} > 1$

Table 3.4: Selection performed in the invariant mass of 3π and η photon candidates for fitting purposes.

Mass Selection for Candidates	
Name of the Cut	**Events Kept**
η Selection	0.4 GeV $<$ M[η] $<$ 0.75 GeV
ω Selection	0.66 GeV $<$ M[ω] $<$ 0.9 GeV

3.8 Statistical Methods for Background Subtraction

3.9 Beam Accidental Subtraction

When an electron hits the diamond radiator, it produces a photon which may cause a reaction at the proton target inside the hall. However, that electron comes together with many more. These other electrons may also produce a photon. Some of the recoiled electrons are tagged with similar energy. This produces a complication since it is difficult to single out the electron that parented the photon that produced an event at the hall. The tagged electrons that did not produce the reaction are called "accidentals". The accidentals introduce combinations in the recorded event. The standard way to address these accidentals combinations is by performing an "accidental subtraction". This is accomplished by artificially pairing photons that are out-of-time with an event. This provides a good estimation of the number of accidentals that are in the in-time combinations. To statistically remove their contribution, a negative weight is provided to these out-of-time events and subsequently subtracted from the in-time peak events. A second alternative, and the one chosen in the previous section consists of choosing the best combination based on the kinematic fit. This method assumes that the discarded extra beam candidates in the in-time peak are accidentals. However, this method can benefit from further scrutiny. As an example, for the partial wave analysis, one would like to estimate the number of non-polarized photons that gets picked if the best combination is to be selected. This is important since a high number of non-polarized photons labeled as polarized could throw off the fit as it would directly overestimate the polarization fraction. Since the impact of this selection (Fig. 3.27b) affects less than 10% of the events, these type of studies were postponed.

3.10 Sideband Subtraction

A sideband subtraction helps deal with the background that sits beneath a resonance peak; a region where the signal and background events are indistinguishable. This method does not get

rid off the background, it only estimates the contribution that comes from the background. The sidebands, regions where the signal is not present, are subtracted from the region that contains the signal. For this procedure to be valid, some criteria needs to be fulfilled. First, the signal and background needs to be described by a continuous function in the region of interest. Second, to make sure that there is a proper subtraction, the average number of events in the sidebands needs to be equal to the estimated number of background events in the signal region. For one dimension, this procedure is intuitive. This study extends this process to perform a sideband subtraction in two dimensions. The main reason a two dimensional sidebands are needed is because the signal is considered to be an event with both an ω and an η particle. Performing the subtraction in one dimension for each of the particles is erroneous, since it could lead to an over subtraction of events.

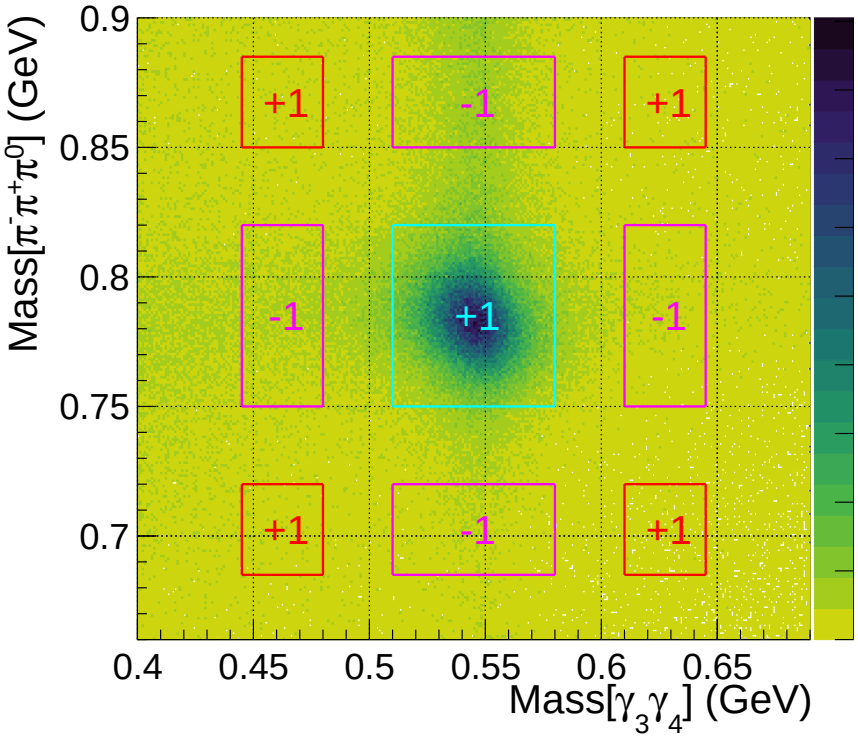

Figure 3.28: Selection of "signal" and "sidebands" and their weight.

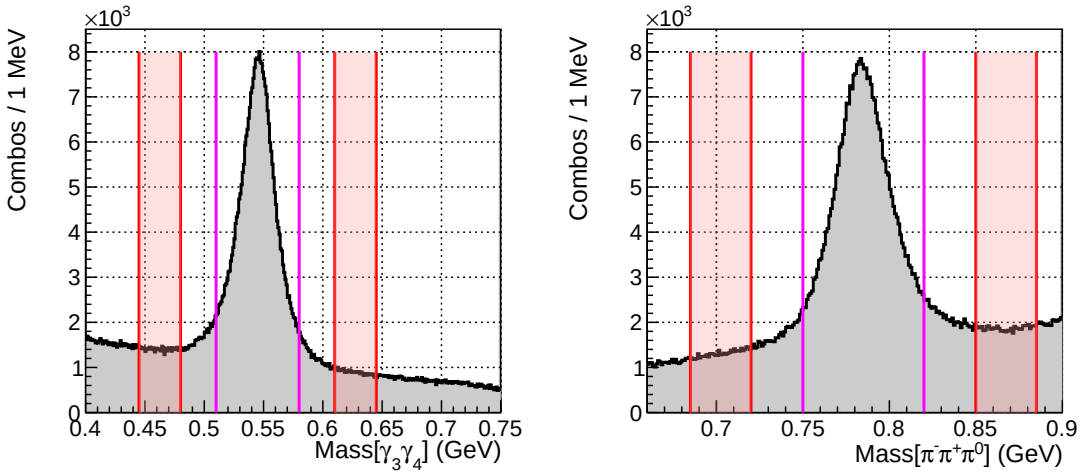

Figure 3.29: Projection of the selection of "signal" and "sidebands".

There are three types of backgrounds that are expected in the data. The first type is an event that does not have an η nor an ω. These are present in all the mass region. Then, events with an η but not an ω. Lastly, events with an ω but not η. These last two only exist in the magenta boxes in Fig. 3.28. To subtract these two backgrounds one needs to calculate the total area of the sideband for each background, to be equal to the area of our "signal" region. By doing this events of the first type are also subtracted, which means that this subtraction happens twice. For this reason events coming from not η and not ω are added back, otherwise there would be an over subtraction. The correction is made by adding the events in the corner regions. To test if this procedure works, there are three characteristics to focus on: how much η' is removed, how much background in the λ distribution is removed, and whether the N* in ηp is affected by the procedure Fig. 3.30.

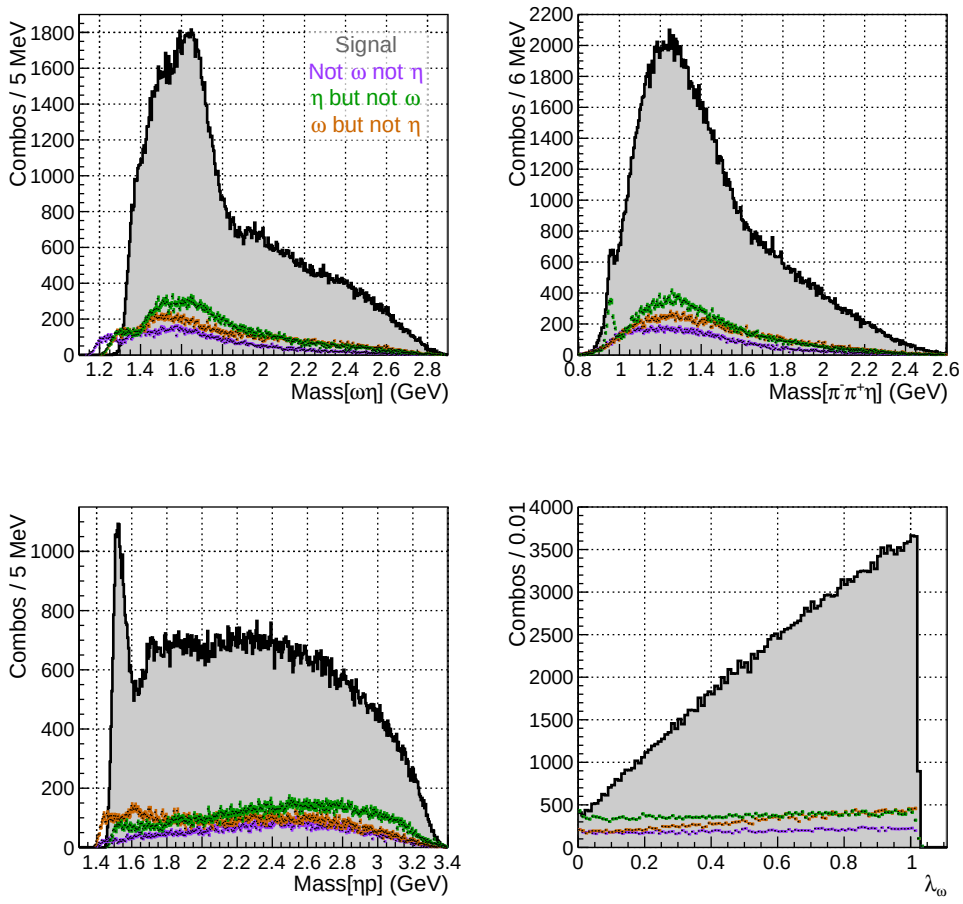

Figure 3.30: The signal region and different sidebands are plotted in these four distributions. Three of them are used to look at the effects of the sidebands.

$\boldsymbol{\eta'}$. This is a resonance that can be identified in the M$[\pi^+\pi^-\eta]$ plot. This background should be addressed only by the η but not ω sideband. As seen in Fig. 3.30, the green histogram is the only one that contains such peaking structure. Not much can be said for the rest of the distribution since no other resonance structure is seen.

$\boldsymbol{\lambda}$. The quantity λ is related to the distance to the center of the Dalitz plot for the 3π and it provides a great way to distinguish ω events [28]. The formula to calculate lambda is given by:

$$\lambda = \frac{|\vec{\pi}^+ \times \vec{\pi}^-|^2}{\frac{3}{4}(\frac{1}{9}M_{3\pi}^2 - M_\pi^2)^2} \tag{3.1}$$

In the plot of λ, the non-ω events offset the slope and have a constant flat distribution. This is because the ω are vector particles and the background is not. The λ plot in Fig. 3.30 demonstrates

this division. The grey histogram has a triangle-like form with an offset below 500. This offset is a good estimation of the non-ω events in the signal region. The green histogram, having no linearly rising events, fully addresses this offset. This indicates that the η but not ω sideband does not contain any ω events on it. In contrast, the orange histogram has both an offset and linearly rising events. This is a good indication that the ω but not η sideband contains some ω and not ω events. As mentioned earlier, the not ω events comes from a general background that permeates all the regions. Moreover, if only the green and orange histograms are subtracted from the grey histogram, then the offset in the λ distribution would be negative. This is why it is crucial that the purple histogram is added back. This histogram corresponds to the not η not ω background, and it completely matches the non-ω background in the red histogram.

N* . The N*, which corresponds to the N(1535), is a state comes from the reaction $\gamma p \to \omega N^*$; where the N* decays to ηp. These type of events live in the "signal" region since they contain both an η and an ω. While this state is considered background for the PWA, it helps in the to monitor good events lost from the sideband subtraction. The sidebands in the M[ηp] from Fig. 3.30 does not have a clear peaking structure where the N* is expected. This is a good sign as it indicates that the sidebands are not removing signal like events.

The effects of the sideband subtraction can be seen in Fig. 3.31. Here, it can be seen that in the M[$\pi^+\pi^-\eta$] plot no longer has the peaking structure associated with the η'. The λ plot has no offset indicating that the non-ω background has been removed. There is only one thing to note, this sideband subtraction method comes with a handicap. Since some selected events have a lower mass for ω or η, there will be some negative entries below thresholds Fig. 3.31. This is, however, not a problem for the PWA. The main analysis will be performed on the M[$\omega\eta$] region above the $\omega\eta$ threshold where these negative values are not present. The resulting sideband subtracted data for GlueX-I has an integral of $\sim$143 k events Fig. 3.32. This makes it the largest $\omega\eta$ data set that has been studied.

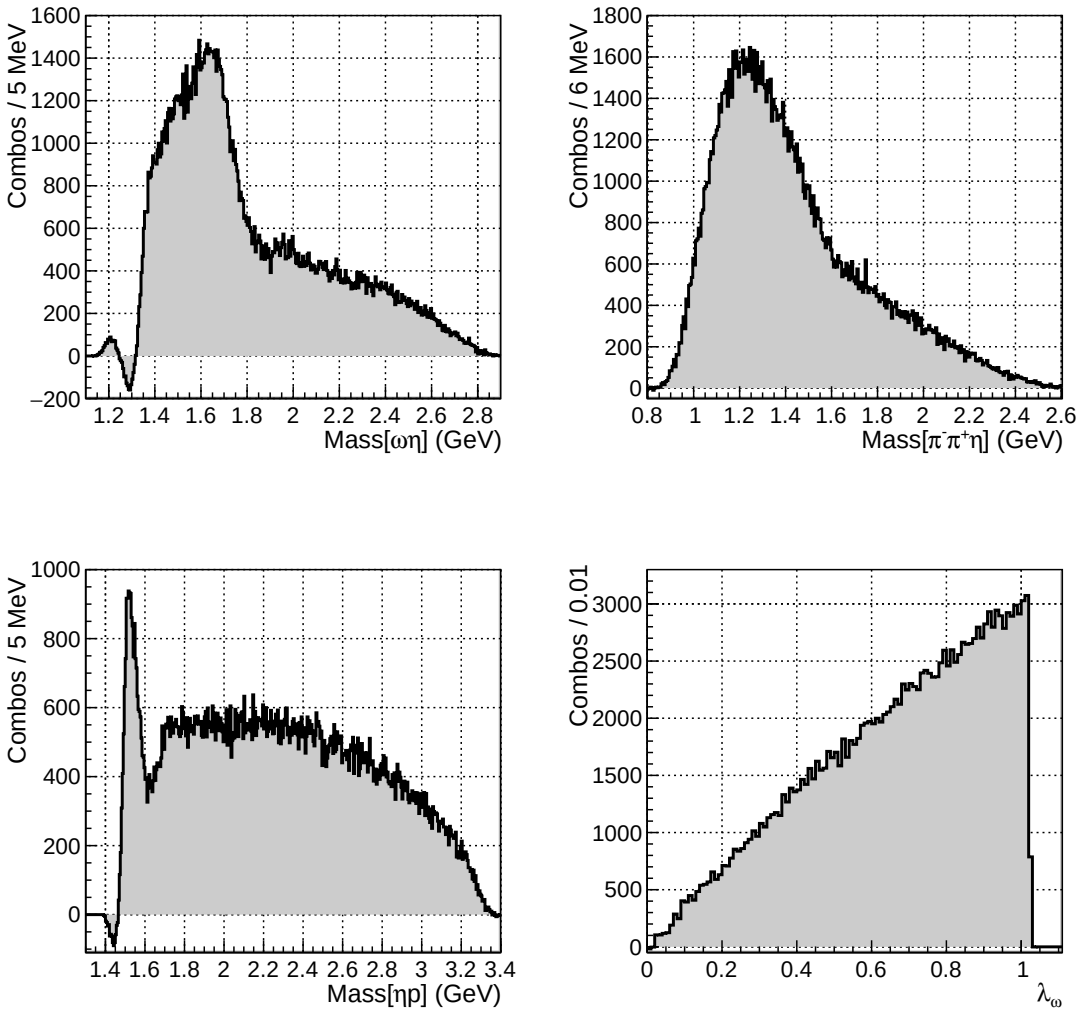

Figure 3.31: The sideband subtraction addressed the background from these distributions. However, threshold effects can be seen created by events that lie below the $\omega\eta$ mass threshold.

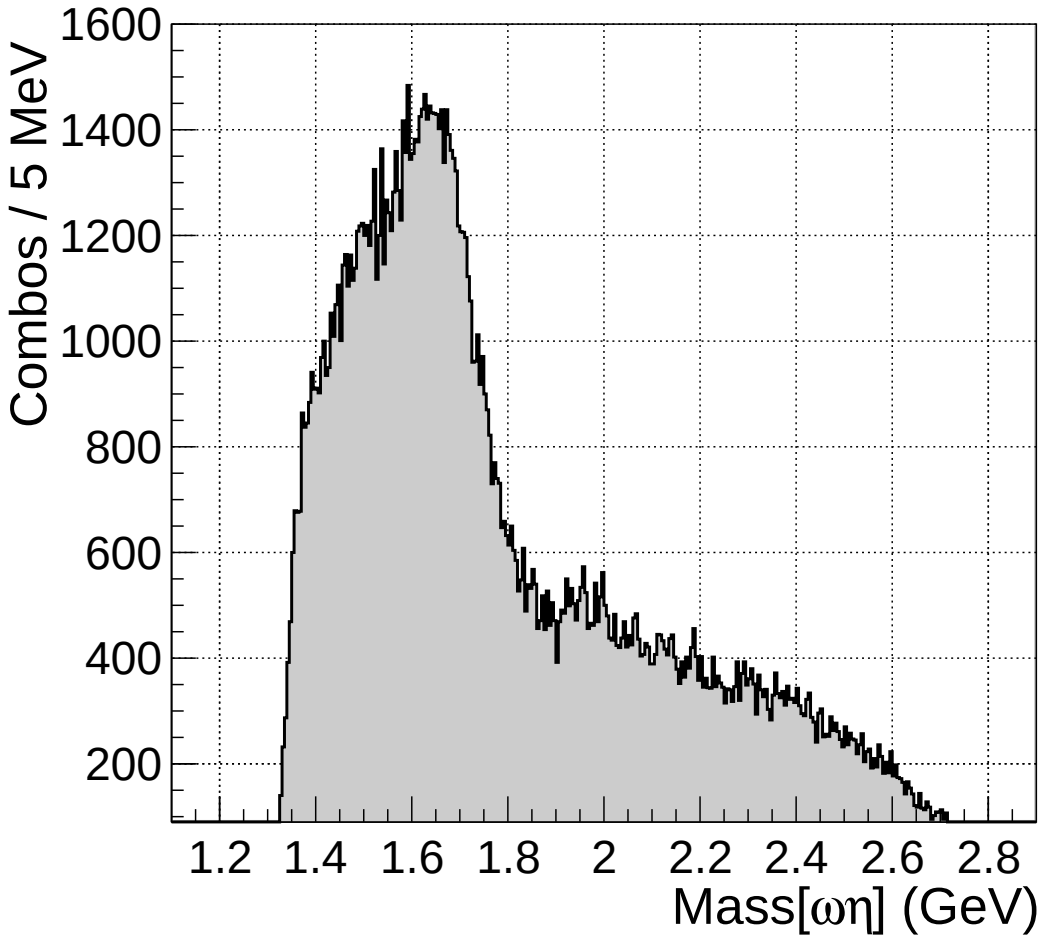

Figure 3.32: Sideband subtracted distribution for M[$\omega\eta$] for GlueX-I. This is the largest $\omega\eta$ data sample with ∼143k events.

3.10.1 MC Test for Sideband Subtraction

A MC sample using the generator *bggen*, which generates different reactions using PYTHIA [53][23], was reconstructed for the $\omega\eta$ final state. This sample not only shows what are the major background contributors, but also allows to test the sideband subtraction procedure. The bggen sample data was reduced using the same data selections from the previous sections. The biggest remaining background corresponds to the $\omega 3\pi^0 p$ channel followed by non resonant $\pi^+\pi^-\pi^0\eta p$ events. Unlike the data, only two distributions can be used to see the effects of the sideband subtraction.

This is because the bggen sample does not include N* events. This sideband subtraction test yielded similar results that for data removing significant contribution from the backgrounds.

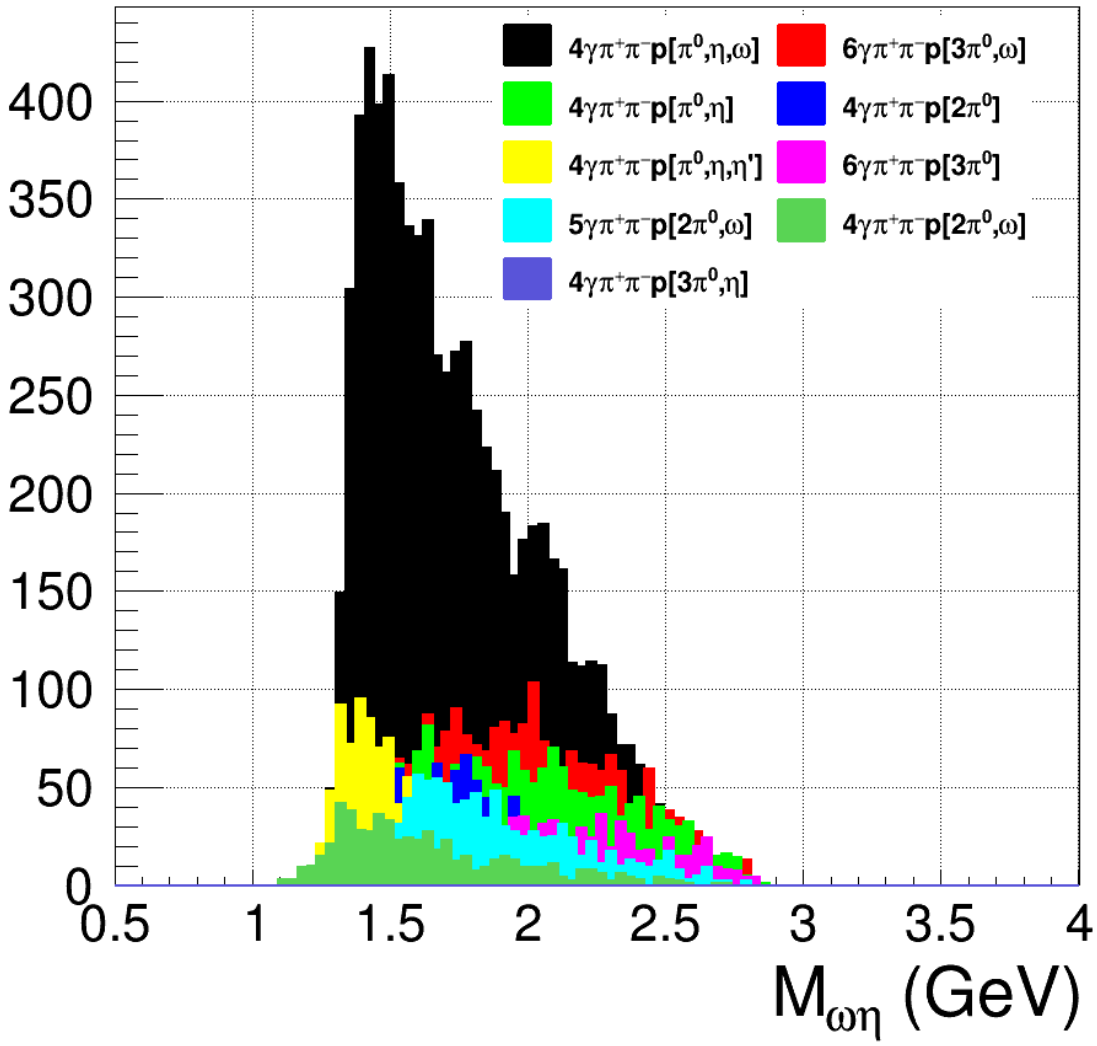

Figure 3.33: In black is the $\omega\eta$ channel. The rest are the top backgrounds that contribute to this reaction.

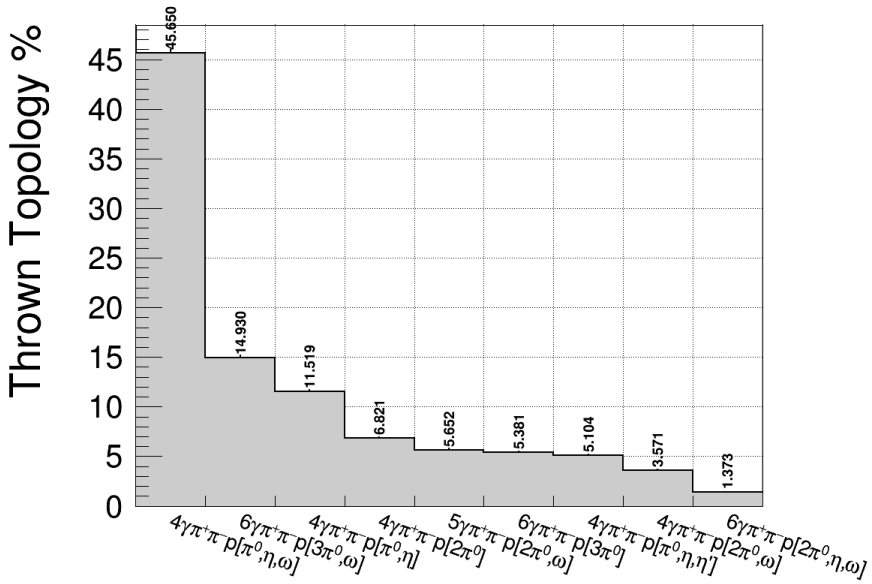

Figure 3.34: The histogram show how much each reaction from plot (a) contributes to the total.

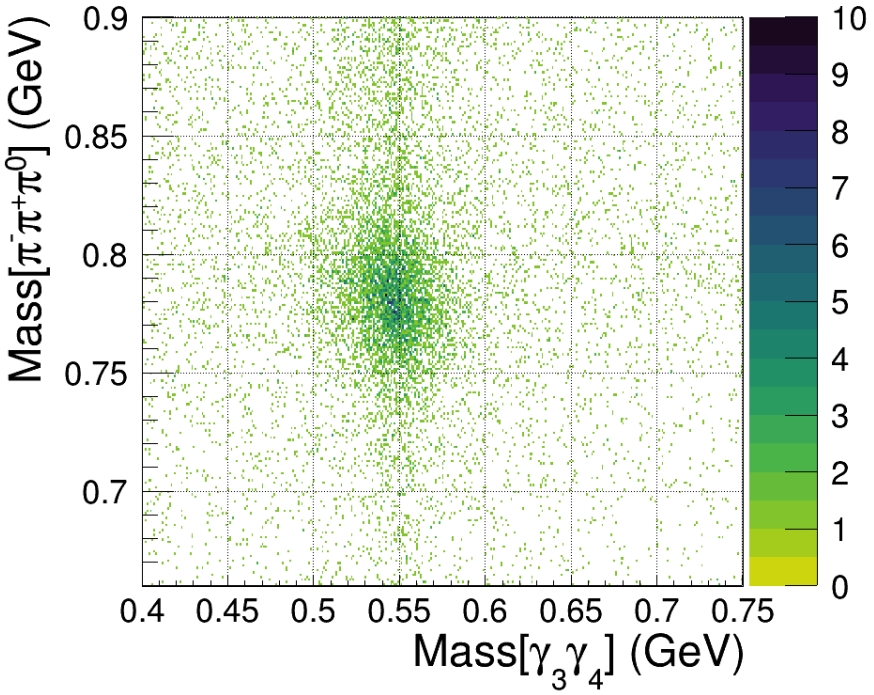

Figure 3.35: Unlike the data where a cross is slightly more visible, the bggen sample has a more η but not ω events.

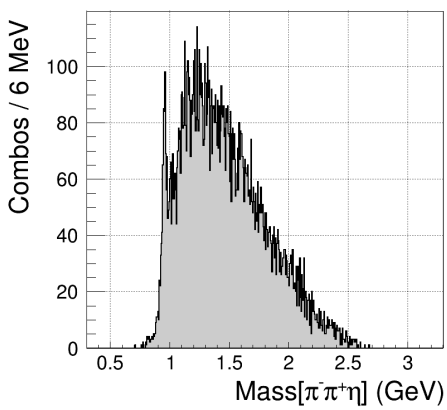

(a) A clear η' signal can be seen in around .9 GeV.

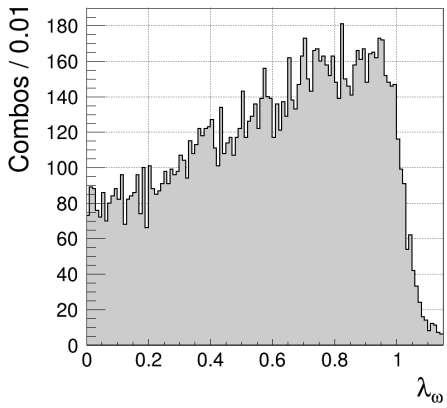

(b) A large offset is seen around 80.

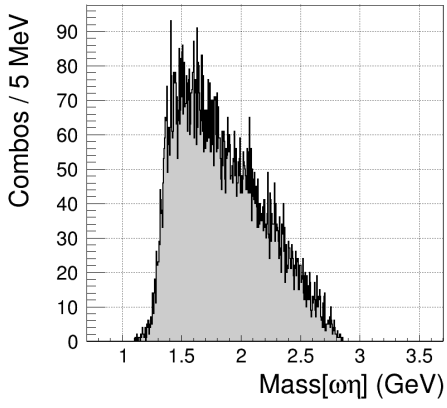

(c) A large offset is seen around 80.

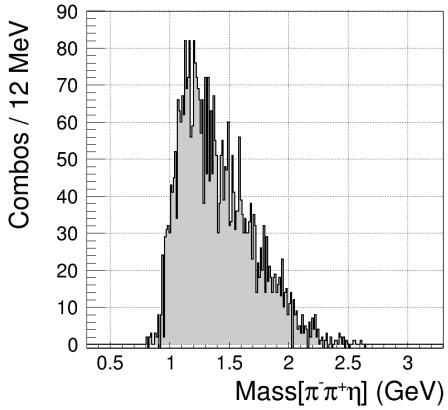

(d) The η' contribution has been removed.

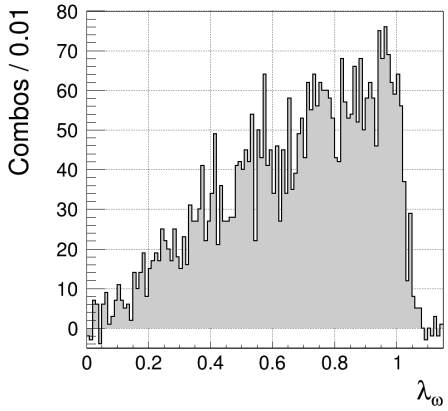

(e) The offset is gone leaving only linearly rising events.

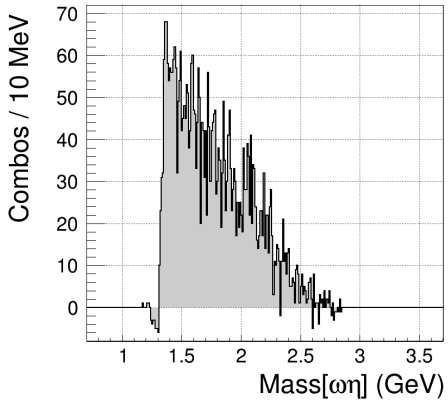

(f) The offset is gone leaving only linearly rising events.

Figure 3.36: Figure on the left shows the plots before and figure on the right shows the plots after the sideband subtraction.

CHAPTER 4

ANALYSIS

4.1 Partial Wave Analysis of $\omega\eta$

Having performed all the selections and statistically negated the contribution from background, it is time to perform the Partial Wave Analysis (PWA) on the data. The fits will be performed using AmpTools [51]; a set of libraries which allow to calculate unbinned maximum likelihood fits. The intensity for vector-pseudoscalar decays is described by expanding the polarized photoproduction intensity model used for two pseudoscalar decays. This is described in section 3.1.2 of Reference [49]. The full derivation to obtain Eq. (4.1) can be found in Reference [50]:

$$\begin{aligned} I(\Phi, \{c^{\epsilon}, Z\}_{J,m}) = 2\sum_{k} \Bigg\{ (1-P_{\gamma}) \Bigg[\Bigg| \sum_{i,m} [c_i]^{-}_{m,k} \mathrm{Im}(Z^{i}_{m}) \Bigg|^2 + \Bigg| \sum_{i,m} [c_i]^{+}_{m,k} \mathrm{Re}(Z^{i}_{m}) \Bigg|^2 \Bigg] \\ + (1+P_{\gamma}) \Bigg[\Bigg| \sum_{i,m} [c_i]^{+}_{m,k} \mathrm{Im}(Z^{i}_{m}) \Bigg|^2 + \Bigg| \sum_{i,m} [c_i]^{-}_{m,k} \mathrm{Re}(Z^{i}_{m}) \Bigg|^2 \Bigg] \Bigg\} \end{aligned} \tag{4.1}$$

The intensity depends on the production angle Φ, a set of amplitudes Z, and the beam polarization fraction P_{γ}. The intensity sums over both spins of the target k. It also sums over all angular momentum l for a particle and their different m projections. The upper script ϵ in the complex coefficients c stands for the reflectivity. The reflectivity is related to the exchange particle at the production vertex. A positive reflectivity is the result of a natural exchange, while a negative reflectivity results from an unnatural exchange. Natural exchange corresponds to J^P of 0^+,1^-,2^+, etc., while unnatural exchange corresponds to J^P of 0^-,1^+,2^-, etc. It is possible to describe the intensity in other basis [48]; however, the reflectivity basis used here allows for clear separation between positive and negative reflectivity.

$$\begin{aligned} Z^{i}_{m} &= e^{-i\Phi} X^{i}_{m}(l, \Omega, \Omega_H) \\ &= e^{-i\Phi} \sum_{\lambda_v=-1}^{1} D^{J_i *}_{m,\lambda_v}(\Omega) F^{i}_{\lambda_v}(l) D^{1*}_{\lambda_v,0}(\Omega_H) G_{Dalitz} \end{aligned} \tag{4.2}$$

The dependence on Φ is made explicitly in the amplitudes. The relationship of the other set of angles comes from the Wigner D functions. F is a function that pairs the parent particle with a

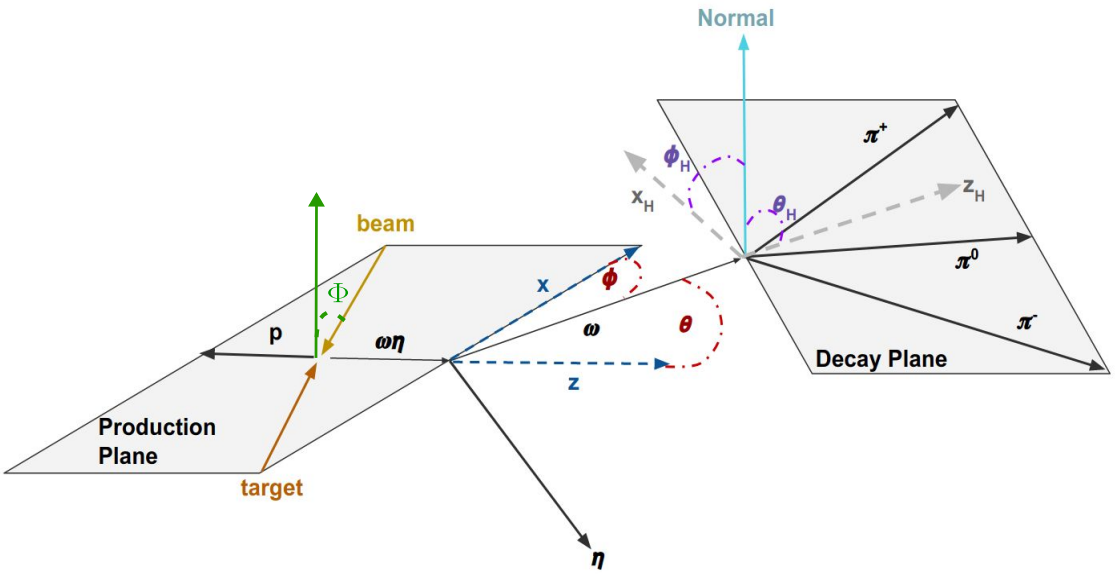

Figure 4.1: Angles used for the intensity formula

value of total angular momentum J and angular momentum l with the ω. This function introduces the Clebsch-Gordon factors as they are summed over the helicities (λ) of the ω. The final term in the amplitude is a constant obtained from the Dalitz decay of the $\omega \to 3\pi$. One of the biggest challenges in PWA is choosing the wave set for the fit. A common approach is to start with a fit containing big number of waves. After looking at the fit results, the waves that have little to no contribution are removed. The fit is performed again with the new wave set, and the process is repeated until only waves that are significant are left in the model. This was the approach used by the E852 collaboration [28]. Their final wave set contained 11 waves. This could be a starting point for the analysis, however, since the intensity formula for vector-pseudoscalar photoproduction is still in the process to be fully understood, this study followed a different approach.

The first fit consists of a model that includes the waves that have been seen in other experiments: 1^{--} and 1^{+-}. This model is not a complete description of the data, but aims to extract the expected major characteristics of it. The model has enough complexity to learn about complications and challenges, and at the same time, it is simple enough to write the intensity by hand. Once there is a better grasp of how the intensity model behaves, it is expected that one can use the same approach as E852 did. The fit in this study was performed in a mass window between 1.325 GeV and 2.0 GeV. The range resembles the one used by E852 collaboration which was between 1.32 GeV and 2.07 GeV. This range also avoids contamination from baryonic resonances such as N(1535) 4.2. Two different

fit methods were performed: a mass independent and a mass dependent. The former consists of dividing the data in mass bins and performing a fit to each mass bin. The latter fits the whole mass range and introduces Breit-Wigner amplitudes that hopes to address the expected particle contributions. A mass independent fit has the advantage to be model independent. Any structure seen in the partial waves can later be fitted by a Breit-Wigner. The mass dependent is a more stable fit since there is an external constraint that enforces continuity across the mass spectrum. Unfortunately, this makes the fit heavily model dependent. The main reason for performing the mass dependent fit was to obtain a good-enough description of the data to be used for simulation studies that provide the particles with some angular distributions.

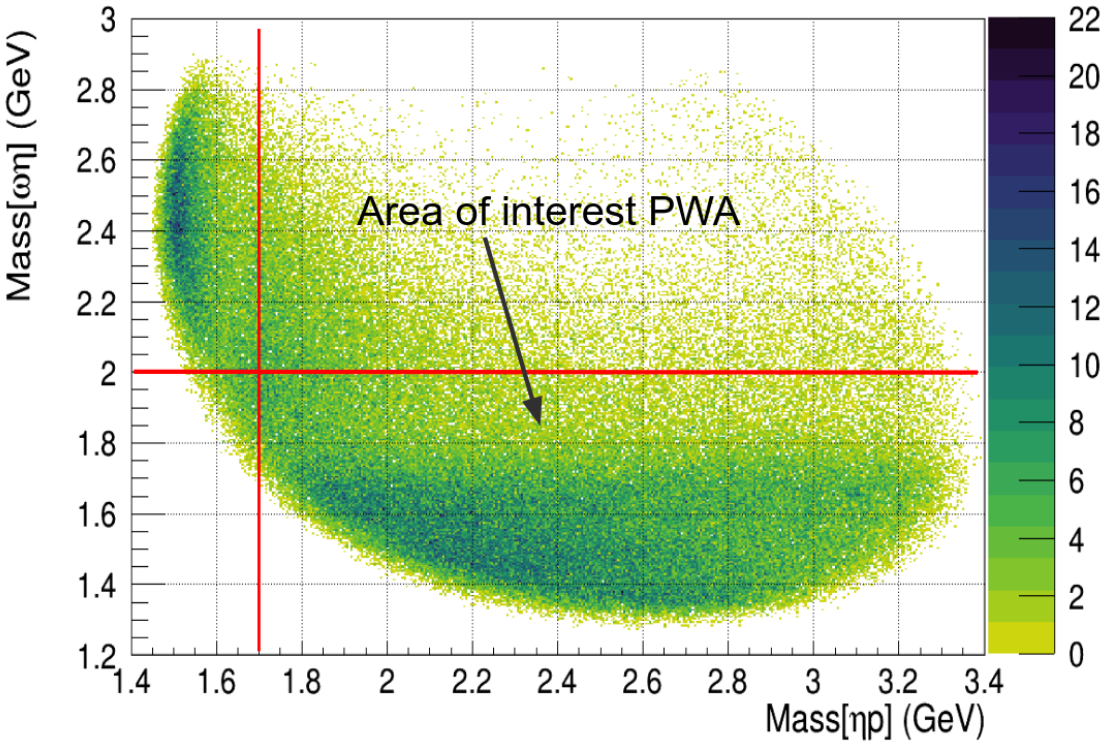

Figure 4.2: The N(1535) and the area of interest for the PWA are in two different kinematic regions.

The mass independent fits show little variation from bin to bin Fig. 4.3. This suggests a the model describes the angular distributions from the data. The S-wave seems to have bigger variation from bin to bin in some areas, which is a sign that a model that includes a bigger wave set should be attempted. There are three prominent structures worth mentioning. Two of them are in the area where the $\omega(1420)$ and $\omega(1650)$ are expected for the P-wave. The other is an unexpected S-wave contribution in the region where the $h_1(1415)$ has been seen. The $h_1(1415)$ is expected prefer

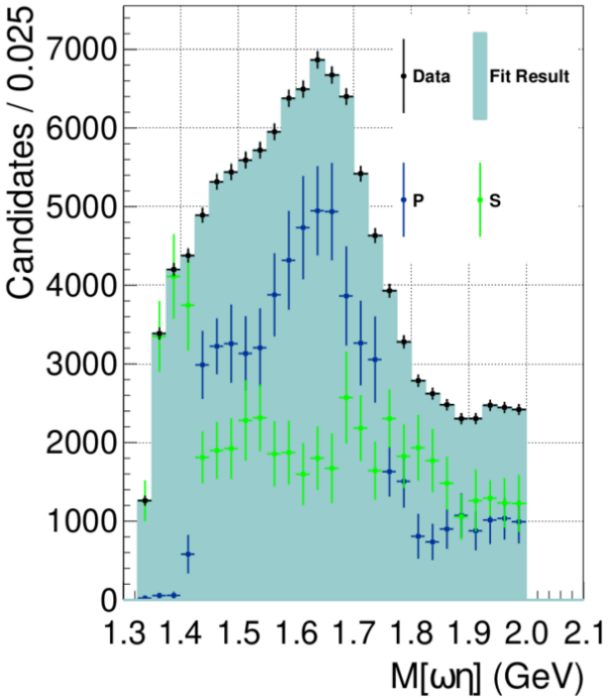

Figure 4.3: PWA mass independent fit in bins of 25 MeV. The contribution for the S-wave is shown in light green and the contribution for the P-wave is shown in blue. The error are given by MINUIT.

another decay mode rather than the $\omega\eta$ since it might be an ideal mixed $s\bar{s}$ state [28][12]. This aligns with what is reported in the PDG [19], where only the $K\bar{K}^*$ decay has been reported. Note that in the lQCD calculations Fig. 1.2, only a single isoscalar state made of non strange quarks is predicted in the lower mass nonet. This is reinforced by Fig. 1.4 which suggest that the $h_1(1115)$ is the other h_1 that belongs to this nonet, and has only been observe to decay to $\rho\pi$. Some structure is seen where the $h_1(1595)$ is expected, but the fit increases in instability right after. The instability could come from lack of partial waves to properly describe the data. Hints of the incompleteness of the model are more visible as the fit approaches the 2GeV mass limit Fig. 4.7. This is also the range where the effects of baryon resonances or double Regge exchange [52][4] starts to contribute to the intensity. Finding a more optimal wave set, or addressing these type of backgrounds would rectify the structures allowing to better judge if there are hints of resonances in this mass region. One can also plot the individual contributions for each m projection. Unfortunately, the fits are unstable except for the m_0 partial waves Fig. 4.8. The instability comes from mathematical ambiguity in the model. This is the topic of the next subsection.

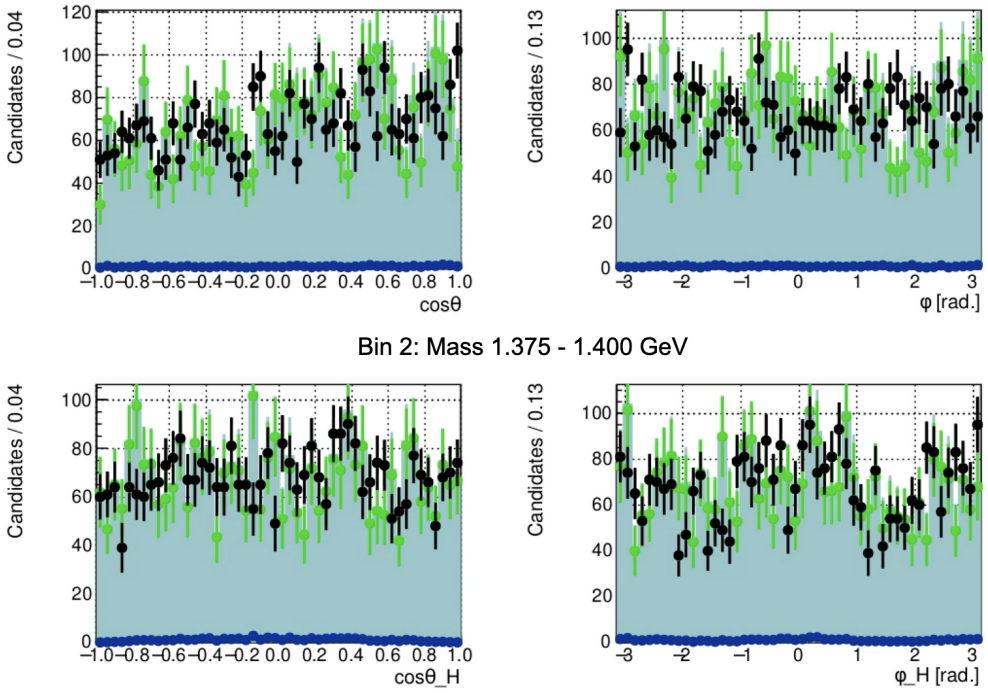

Figure 4.4: The total fit, the dark aquamarine color histogram, does a good job describing the angles. Notice that only the S-wave contributes in this bin.

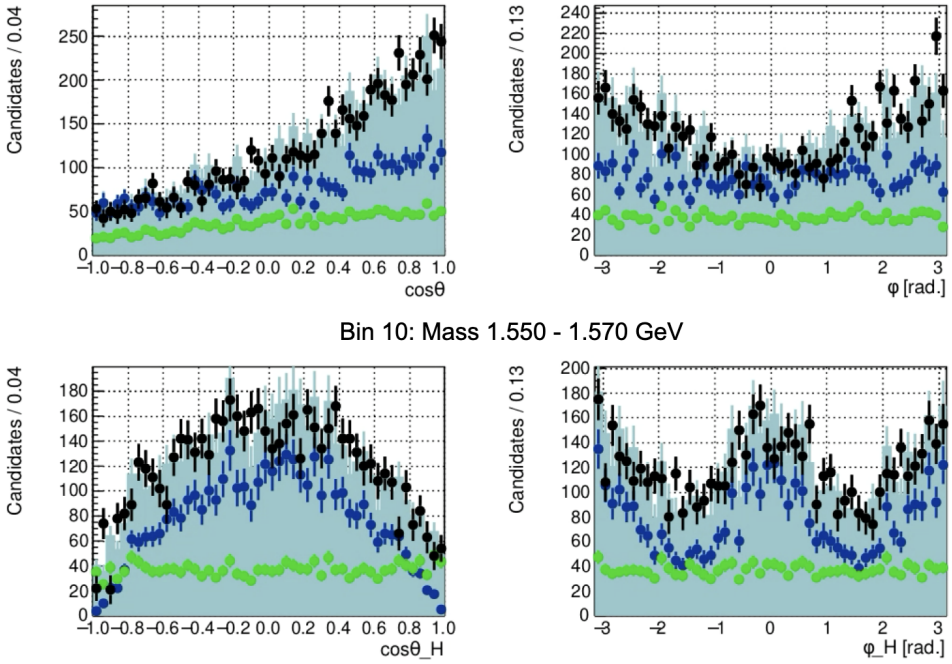

Figure 4.5: The total fit still does a good job describing the angles. However, the P-wave seems to be the dominant contribution in this bin.

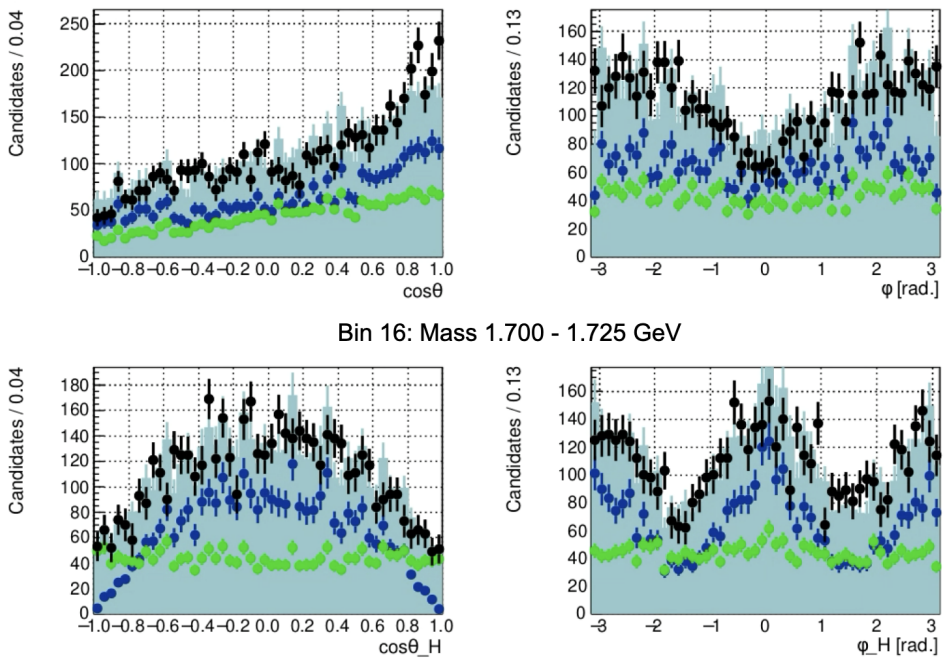

Figure 4.6: The total fit is starting to not fully describe some angles. Notice the white space around the peak at 1 in $cos\theta$. This effect is small in this bin.

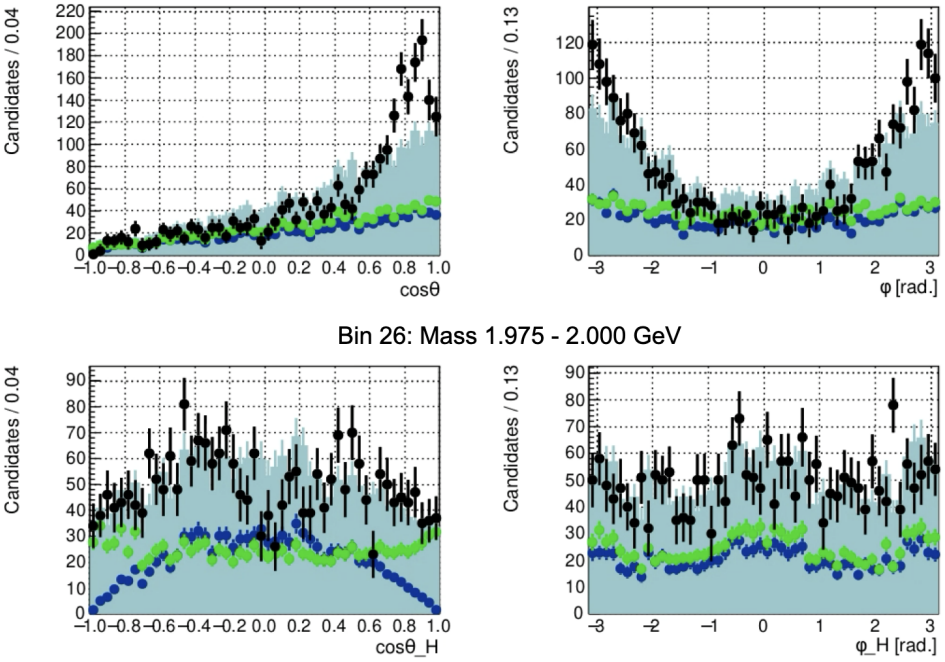

Figure 4.7: The lack of proper description in $cos\theta$ is drastic here. This is a good indication that a wave set with only S and P waves is insufficient to describe the data.

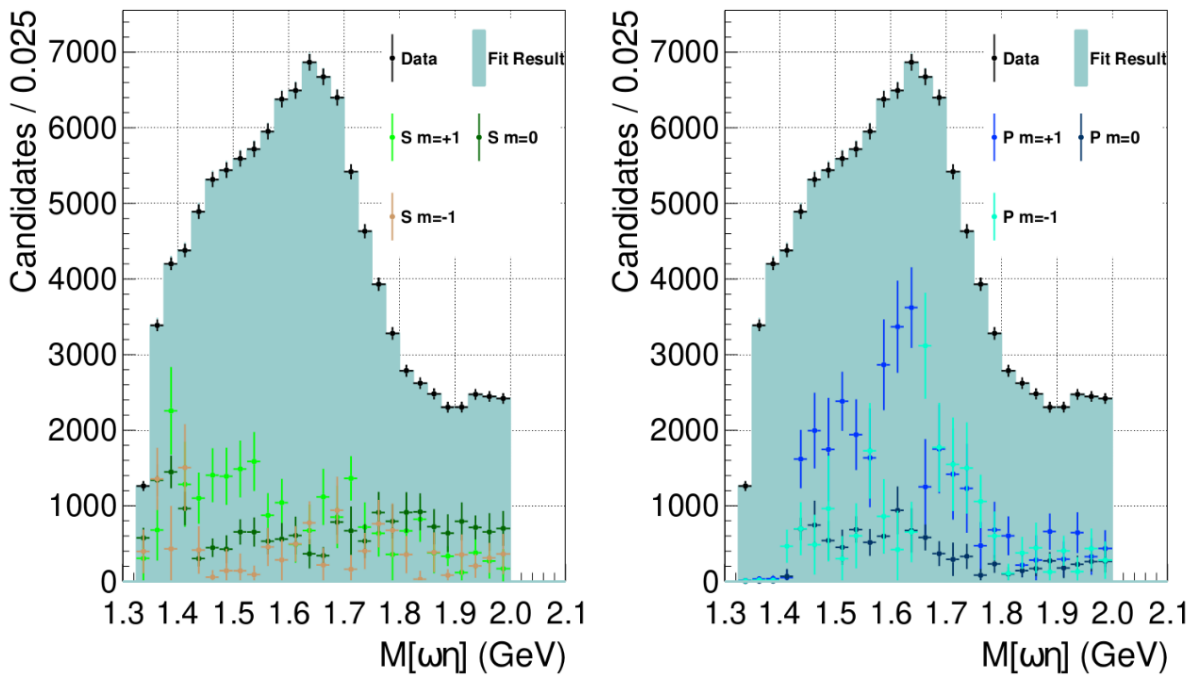

(a) The three m projection plotted individually for the S wave.

(b) The three m projection plotted individually for the P wave.

Figure 4.8: Notice that for both waves, the $m = -1$ and $m = +1$ projections are not stable from one bin to the next. In contrast, the $m = 0$ is quite stable

The results of the preliminary mass independent fit inspired the Breit-Wigner amplitudes that were used for the mass dependent fit. This fit does not aim to assert or predict any resonances in the mass distribution. The goal is to have an amplitude model that can be used to test signal contribution for the $\omega\eta$ decay. In principle, other channels that have $\omega\eta$ as a background could benefit from this type of MC too. However, the fit could give hints that could help improve the mass independent fit model. This is because once there is a working model, it can be used for input/output test. This type of testing allows one to see if there are leakage due to acceptance effects or other technicalities in the fitting process. The fit presented here does a good job describing the invariant mass of $\omega\eta$ but, similar to the high mass bins in the mass independent fit, it does not describes properly $\cos(\theta)$ values close between .7 and 1. The fact that the fit does a similar job describing the data to the mass independent fit suggest that the P wave might be the dominant contribution in this mass range.

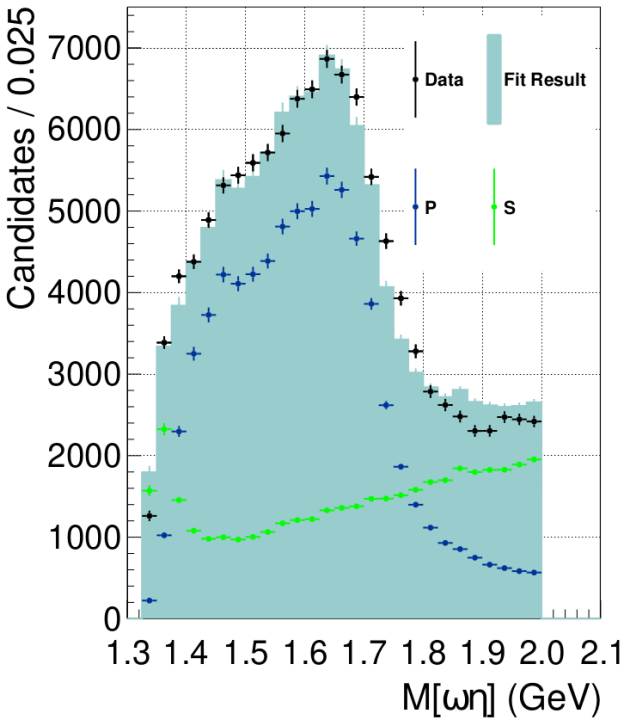

Figure 4.9: PWA mass dependent fit. The contribution for the S-wave is shown in light green and the contribution for the P-wave is shown in blue. The error are only statistical. This model did not include the $h_1(1595)$. Notice that the fit result closely matches the data.

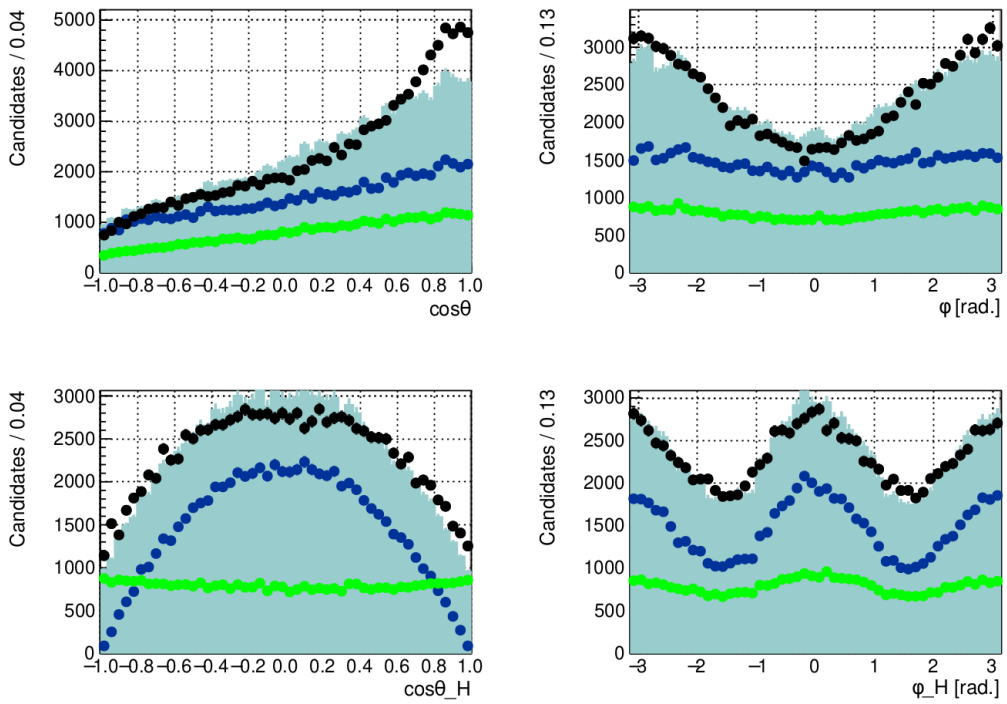

Figure 4.10: Angles for the PWA mass dependent fit. The contribution for the S-wave is shown in light green and the contribution for the P-wave is shown in blue. The error are only statistical. This model did not included the $h_1(1595)$. Similar to the mass independent fit, this model does not fully describe the angle $\cos(\theta)$ close to 1.

4.1.1 Explanation for PWA Instability

The intensities for the S and P waves were fully expanded (Appendix ##)[2] . Each intensity contains only the contribution of $m = 1$ and $m = +1$. This is because the $m = 0$ looked stable in the fits.

S-Wave Intensity. The final form of the intensity (Eq. (4.1)) of the S-wave reduced to the following formula:

$$
\begin{aligned}
I = {} & [(\rho_1^+)^2 + (\rho_1^-)^2 + (\rho_{-1}^+)^2 + (\rho_{-1}^-)^2]\,[(A+C)^2 + B^2] \\
& + 2[\rho_{-1}^+\rho_1^+ \cos\eta^+ + \rho_{-1}^-\rho_1^- \cos\eta^-]\Big(\cos 2\phi\big(-(A+C)^2 + B^2\big) + 2B(A+C)\sin 2\phi\Big) \\
& + P_\gamma\Bigg\{\Big[(\rho_1^+)^2 - (\rho_1^-)^2\Big]\cos 2\Psi\Big(-(A+C)^2 + B^2 + 2B(A+C)\tan 2\Psi\Big) \\
& + \Big[(\rho_{-1}^+)^2 - (\rho_{-1}^-)^2\Big]\cos 2\Psi'\Big(-(A+C)^2 + B^2 + 2B(A+C)\tan 2\Psi'\Big) \\
& + 2[\rho_{-1}^+\rho_1^+ \cos\eta^+ - \rho_{-1}^-\rho_1^- \cos\eta^-]\cos 2\Phi\Big((A+C)^2 + B^2\Big)\Bigg\}
\end{aligned}
\tag{4.3}
$$

The A, B,and C are functions of angles used to reduce the visual complexity in the formula. They are defined as:

$$\begin{aligned} A &\equiv \sin\theta_H \cos\theta \cos\phi_H \\ B &\equiv \sin\theta_H \sin\phi_H \\ C &\equiv \sin\theta \cos\theta_H \end{aligned} \tag{4.4}$$

In the formula above, the ρ^{ϵ}_{m} are the magnitude of the complex coefficient for a given reflectivity ϵ and m wave projection. The η^{ϵ} are the phase difference between two m waves with the same reflectivity. The angle $\Psi = \phi - \Phi$; this is the difference between the azimuthal angle for the $\omega\eta$ system (ϕ) and the angle between the production plane and the beam polarization (Φ). The angle Ψ' is obtained by adding ϕ and Φ together. The angle θ is the polar angle of the $\omega\eta$ system. And, the angle θ_H and ϕ_H are the angles for the of the vector normal to the production plane for the ω decay Fig. 4.1.

P-Wave Intensity. A very similar formula was obtained for the P-Wave:

$$\begin{aligned} I = P_\gamma sin^2\theta_H \Bigg\{ & 2[\rho^-_1\rho^-_{-1}cos\eta_- - \rho^+_1\rho^+_{-1}cos\eta_+]cos(2\Phi)\Big(sin^2\phi_H cos^2\theta + cos^2\phi_H\Big) \\ & + [(\rho^+_1)^2 - (\rho^-_1)^2]cos(2\Psi)\Big(sin^2\phi_H cos^2\theta - cos^2\phi_H + tan(2\Psi)sin(2\phi_H)cos\theta\Big) \\ & + [(\rho^+_{-1})^2 - (\rho^-_{-1})^2]cos(2\Psi')\Big(sin^2\phi_H cos^2\theta - cos^2\phi_H + tan(2\Psi')sin(2\phi_H)cos\theta\Big)\Bigg\} \\ & + sin^2\theta_H\Bigg[[(\rho^+_1)^2 + (\rho^+_{-1})^2 + (\rho^-_1)^2 + (\rho^-_{-1})^2]\Big(cos^2\phi_H + sin^2\phi_H cos^2\theta\Big) \\ & + 2[\rho^+_1\rho^+_{-1}cos\eta_+ + \rho^-_1\rho^-_{-1}cos\eta_-]cos(2\phi)\Big(cos^2\phi_H - sin^2\phi_H cos^2 - 2sin(2\phi_H)cos\theta\Big)\Bigg] \end{aligned} \tag{4.5}$$

Lack of Constraints Causes Ambiguity in the Intensity. When performing a PWA, the ρ's and η's are the free parameters in the fit. In both intensity equations, the total number of free parameters is 8. However, one overall phase can be factored out for each reflectivity. This factorization is easier to understand from equation Eq. (4.1), where the coefficients are being added under the same modulus square. This reduces the numbers of free parameters to 6. Unfortunately, there are only 5 independent equations that make the intensity. One for each unique angular coefficient: no angular coefficient, $cos(2\Phi)$, $cos(2\Psi)$, $cos(2\Psi')$, and $cos(2\phi)$ The transition of a single equation to 5 is not obvious. The following simplified example should give a better insight of

the transition. In mathematics, two polynomials of n order are equal to each other if the coefficients of each term are equal. For example, two polynomials of first order with different coefficients,

$$f(x) = \quad a + bx \tag{4.6a}$$

$$g(x) = \quad a' + b'x \tag{4.6b}$$

$$\tag{4.6c}$$

are identical to each other when $a = a'$ and $b = b'$ for a given x value. Now, imagine that the coefficients of $f(x)$ can be expressed by some ρs:

$$f(x) = \quad (\rho_1 - \rho_2) + (\rho_1 + \rho_2)x \tag{4.7}$$

The previous equality statement between $f(x)$ and $g(x)$ still holds true. This means that one needs to solve the follow system of equations to get values for the different ρ coefficients:

$$a' = \quad (\rho_1 - \rho_2) \tag{4.8a}$$

$$b' = \quad (\rho_1 + \rho_2) \tag{4.8b}$$

$$\tag{4.8c}$$

To start connecting the example to the intensity, imagine that $f(x)$ is the function that is fitted to describe the measured values which are given by $g(x)$. Then, the fitter will extract unique values for the ρ coefficients since there are two free parameters, and two linearly independent equations. In a similar manner, the intensity equation can be described similar to this example. The only caveat is that $cos(\alpha)$ should be treated as "x", and not α. This is because the intensity function is closer to a Fourier series than to a polynomial. So, the current model for intensity is under constrained having 6 free parameters and 5 equations. For a single wave, it is easier to absorb all of the other angular coefficients in the "x" variable. Note that when having a multi wave fit, it is common practice to set to zero the contributions of all but one wave. This allows to plot the contribution of the wave whose coefficients were kept. Absorbing all the angular dependence in a single variable gives rise to the follow set of equations:

$$K \equiv (\rho_1^+)^2 + (\rho_1^-)^2 + (\rho_{-1}^+)^2 + (\rho_{-1}^-)^2 \tag{4.9a}$$

$$\beta_1 \equiv (\rho_1^+)^2 - (\rho_1^-)^2 \tag{4.9b}$$

$$\beta_{-1} \equiv (\rho_{-1}^+)^2 - (\rho_{-1}^-)^2 \tag{4.9c}$$

$$Y_\Phi \equiv 2\rho_{-1}^+\rho_1^+ \cos\eta^+ - 2\rho_{-1}^-\rho_1^- \cos\eta^- \tag{4.9d}$$

$$Y_\phi \equiv 2\rho_{-1}^+\rho_1^+ \cos\eta^+ + 2\rho_{-1}^-\rho_1^- \cos\eta^- \tag{4.9e}$$

Where K, β_1, β_{-1}, Y_Φ, and Y_Φ, are arbitrary symbols for the coefficients. They can be extracted from data. The above set of equations can be combined to reduce the number of variables. The variable $(\rho_1^+)^2$ was arbitrarily chosen to express the rest of the variables as follow:

$$(\rho_1^-)^2 = (\rho_1^+)^2 - \beta_1 \tag{4.10a}$$

$$(\rho_{-1}^+)^2 = \frac{K + \beta_{-1} + \beta_1}{2} - (\rho_1^+)^2 \tag{4.10b}$$

$$(\rho_{-1}^-)^2 = \frac{K - \beta_{-1} + \beta_1}{2} - (\rho_1^+)^2 \tag{4.10c}$$

$$(\rho_1^+)\sqrt{\frac{K + \beta_{-1} + \beta_1}{2} - (\rho_1^+)^2}\cos(\eta^+) = \frac{Y_\phi + Y_\Phi}{2} \tag{4.10d}$$

$$\sqrt{(\rho_1^+)^2 - \beta_1}\sqrt{\frac{K - \beta_{-1} + \beta_1}{2} - (\rho_1^+)^2}\cos(\eta^-) = \frac{Y_\phi - Y_\Phi}{4} \tag{4.10e}$$

These new set of equations was used to predict the ranges of the parameter allowed in the fit. Monte Carlo simulation for $\omega\eta$ were used for test the predictions.

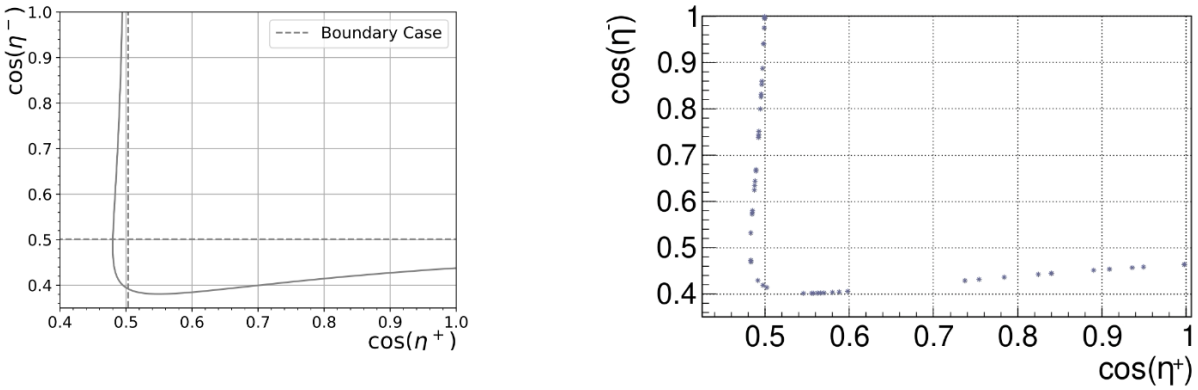

Figure 4.11: On the left is the predicted values of η for which the intensity would be yield the same value. On the right are fits to a MC toy model for 100 random starting seeds.

4.2 Extracting the Width of the N(1535)

The N(1535) is considered background in the main analysis. However, its signal appears to be strong and it is possible to extract this state's mass and width. The mass and width of the N(1535) has only been measured indirectly through PWA [19]. The data in this analysis allows one to directly fit this resonance. To do this, the mass of $p\eta$ was fitted with a convolution of a relativistic Breit-Wigner with a Gaussian (relativistic Voigt) plus the shape of phase space Monte Carlo for $\omega\eta$ to describe the background. The results of this fit suggest that the width of the N(1535) is narrower by almost half of the value cited by the PDG. This interesting result gives motivation to pursue a fit to the cross-section $\frac{d\sigma}{dm}$ to describe line shape of this resonance.

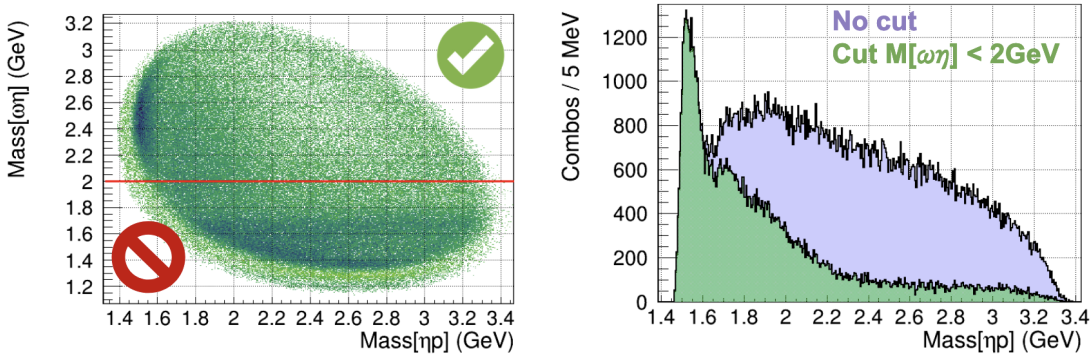

Figure 4.12: The meson system can be removed to focus only on the baryon contribution.

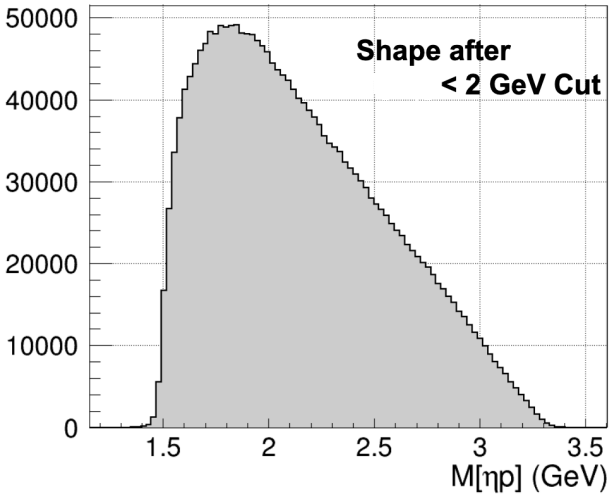

Figure 4.13: This is the shape of the MC after all the selections have been applied. For the fit only events up to 1.8 GeV were used.

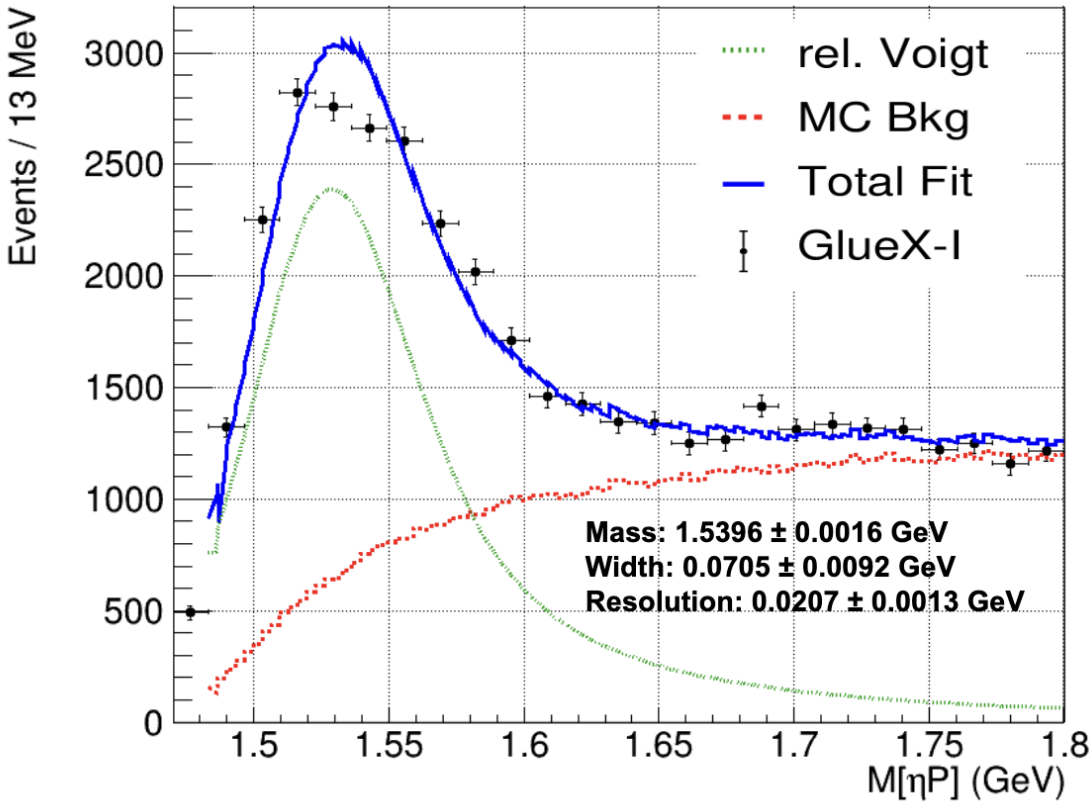

Figure 4.14: Fit using a relativistic Voigitan for signal and using the shape of $\omega\eta$ phasespace MC for the background. The width is half to what the 150 MeV reported in the PDG.

CHAPTER 5

RESULTS AND DISCUSSION

5.1 A Path Forward for the PWA

Stability of Coefficients. MC studies showed that the coefficients from Eq. (4.9) are stable, though they have a small Gaussian spread Fig. 5.1. In fact, the seem to be close to the generated value than what is obtained for the magnitude of the amplitudes Fig. 5.2. More studies are needed to understand how the coefficients behave when more than one wave is added. Nonetheless, it was decided to test this approach to the data set using the current PWA fit model (S and P waves). The results presented are only for the coefficients of a single wave since the calculation of cross terms of S and P wave is still undergoing.

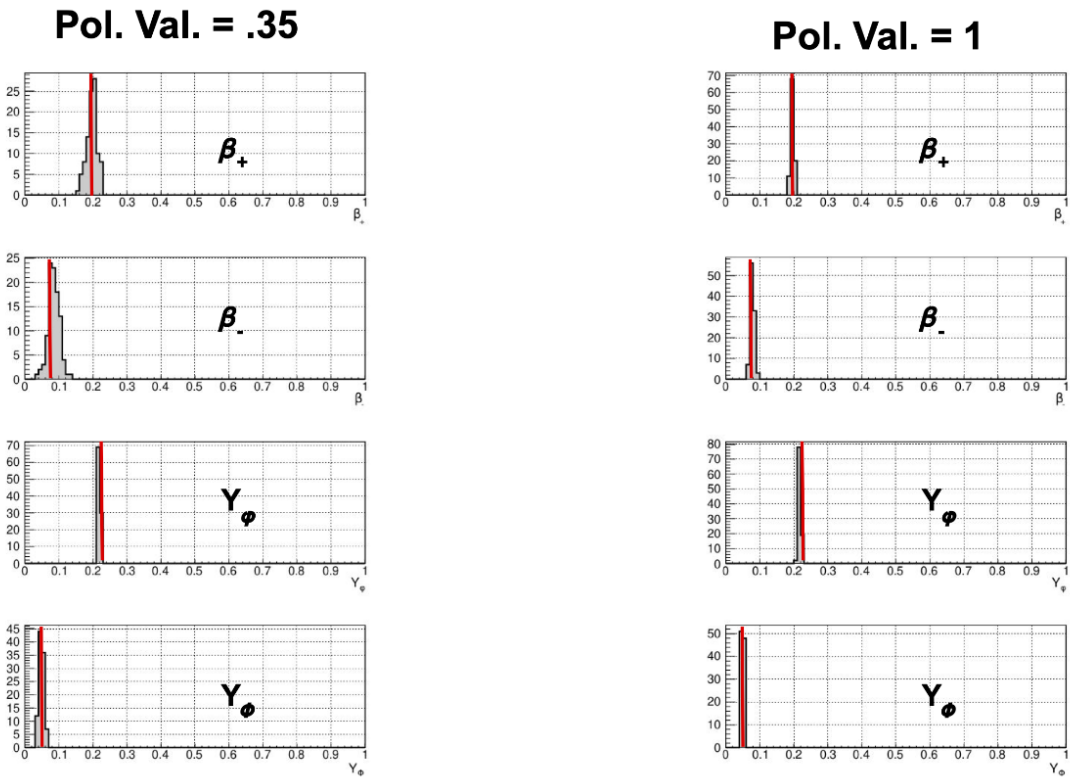

Figure 5.1: The generated value for the coefficient is at the location of the red line. Each entry in these histograms correspond to the result of one of the fifty randomized fits.

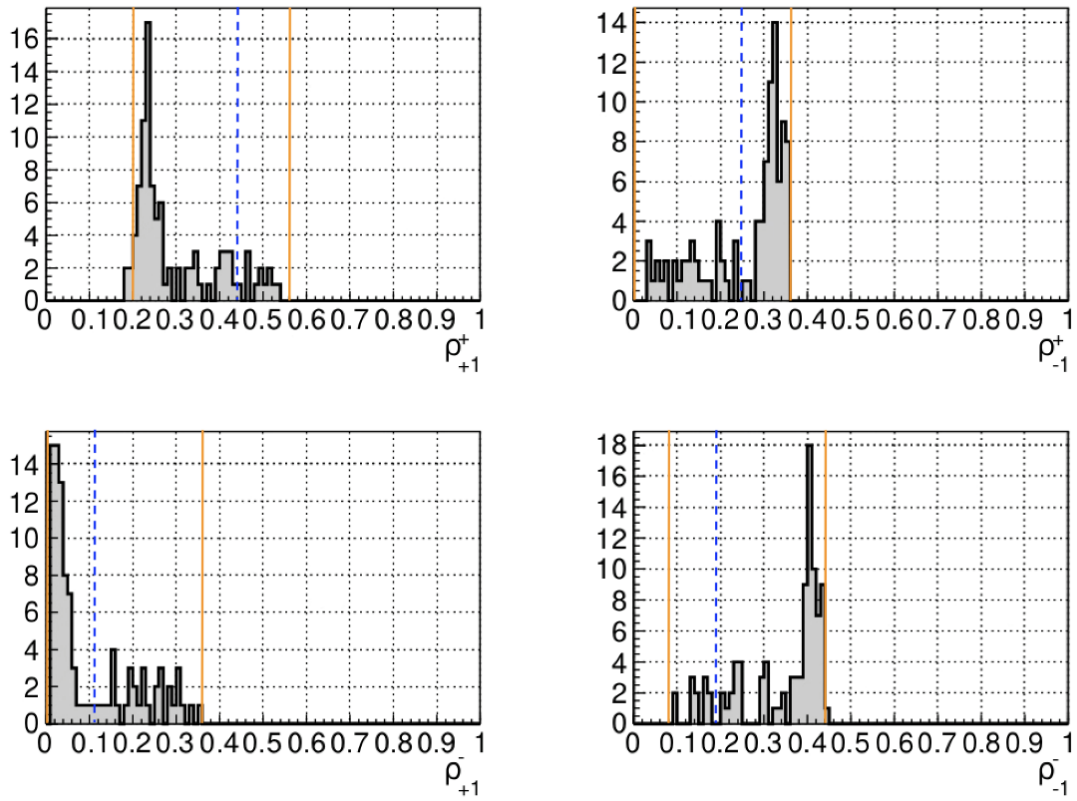

Figure 5.2: The magnitude of the amplitudes is shown here for the same data set as Fig. 5.1. The blue line shows where the generated value is located, while the orange lines show the limits that can be obtained from Eq. 4.10a - 4.10e

For both the S and P waves both β coefficient are always close to 0 as seen in Fig. 5.3. This suggest that both reflectivities are present with equal strength, and that ambiguities affect the plotted m=$\pm$1 projections in Fig. 4.8. Interesting exceptions happen at the mass of where the $\omega(1650)$ is expected. At this location there is a dominant reflectivity as suggested by the increase in the β values. This regions also seems to have a change in sign for the Y_ϕ term. A change in the sign of the phase difference vs mass is normally a sign for a resonance. This is normally tested for two different waves, i.e. S and P waves, and not for two projections of the same wave, e.g. m+ and m- from the P wave. Moreover, the Y terms do not map the whole phase difference space. These two main differences prevent from drawing conclusion regarding the presence of resonances.

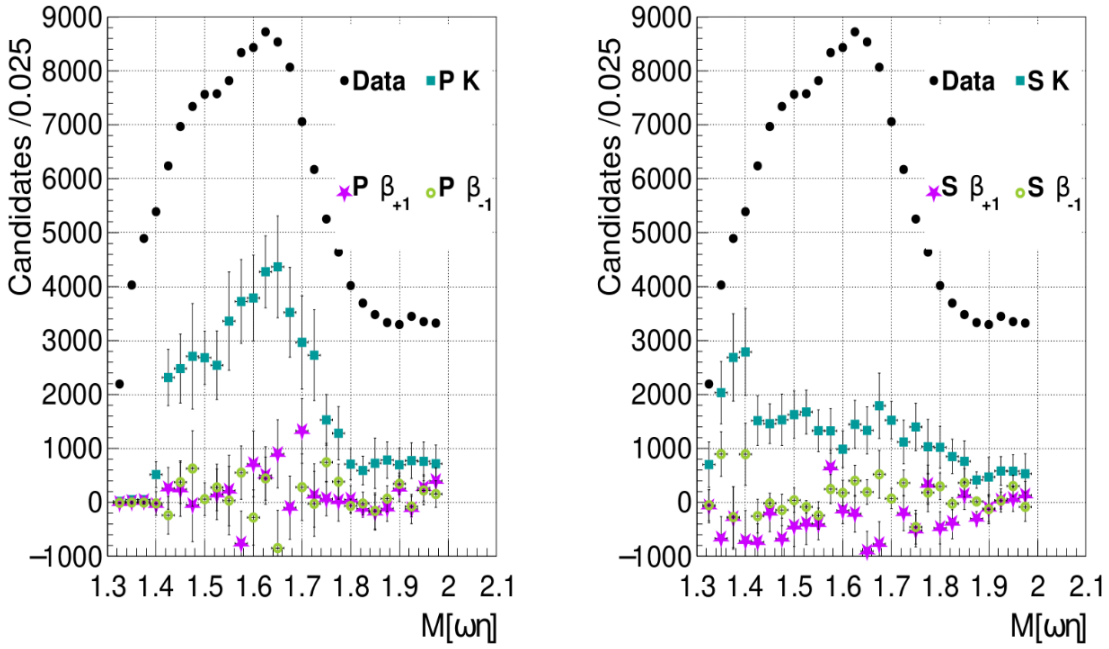

Figure 5.3: These are the β values obtained from data. They mostly consistent with 0 withing error.

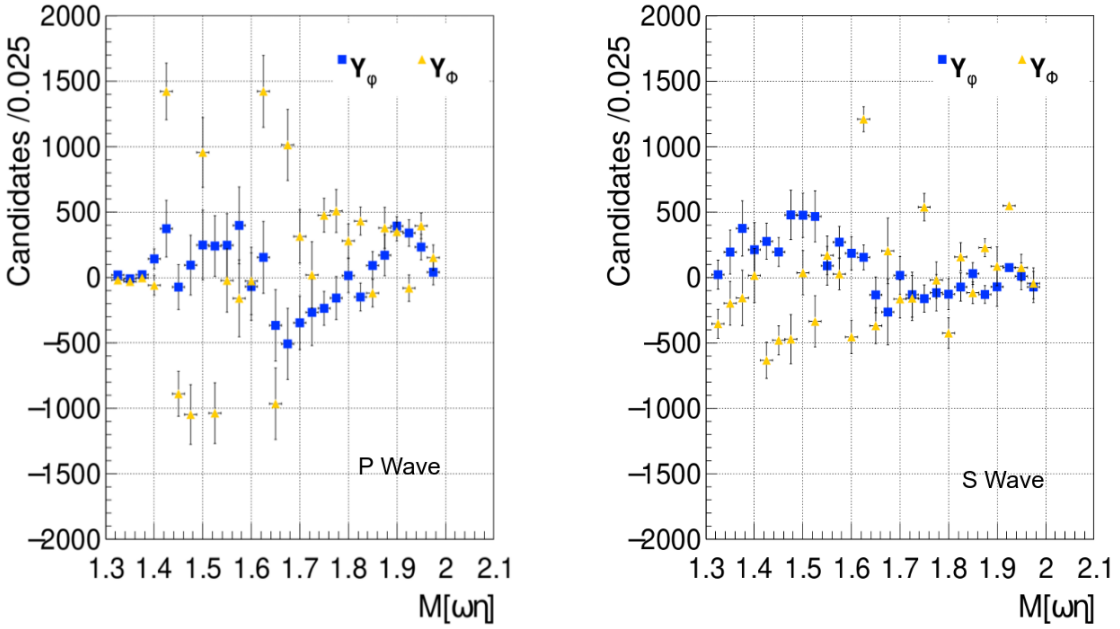

Figure 5.4: These are the Y values obtained from data. While there is not a clear interpretation for this coefficient, the change in sing around the mass of the $\omega(1650)$ is a puzzling characteristic.

5.1.1 Different Approaches to Study the Partial Waves

A PWA study is the ultimate goal for this channel. However, there are alternative methods that might help gather information from the data. These methods could solve the ambiguities on the data through external constraints or may help choose a wave set for the PWA.

Mass Semi-Independent Fits. If there is sufficient evidence for the presence of a resonance, the fit could include a Breit-Wigner amplitude. This amplitude would provide continuity on the phases across the mass and provide an external constraint to remove ambiguities. The caveat is that a good understanding of the resonance is needed to describe it with a Breit-Wigner amplitude. This is unfortunately difficult in this channel. The most likely candidate to for the use of this method is the $\omega(1650)$. Which, as mentioned in the motivation for this study, does not have a solid state in the PDG. The widths listed for different experiments in the PDG expand over a wide range [19]. Should this approach be used, one would need to carefully study the systematic errors of varying the different selected width of the particle.

Angular Moments. A second option is to study the angular distributions using angular moments. These are a set of orthogonal quantities that help describe the characteristics of the data. They are orthogonal since the intensity is decomposed following a generalization of Fourier series. Unfortunately, this mathematical quantities are difficult to give a direct physical meaning. One of the reasons is that the moments interpretation in terms of amplitudes is wave set dependent. The coefficients obtained from the ambiguity study could be directly related to these angular moments. For example, a quick look suggests that the β coefficients are related to angular moments with $M = 2$ and K to angular moments with $M = 0$. Correlating the moments to the coefficients could bridge a path for more physically meaningful interpretation of the moments.

5.2 Next Steps in the Study of N(1535)

New MC needs to be generated to better represent the backgrounds which should improve fit and help correct the acceptance of the data. Once the MC is ready, it will be possible to calculate the cross section of the reaction and fit a relativistic Voigtian to it. One of the things that this study could benefit is the correction of events below the pη threshold. This could be done by scaling the vectors such that they lie within the expected mass of the η, while at the same time not altering the angular distributions. A different approach would be to use kinematically fitted data with a mass constraint on η. The main disadvantage to this last approach is the inability to statistically

remove a background. The background from the η is estimated to be 30% of the total events. However, the events of the current data set with their sideband weights can be saved and matched to their mass constrained counter part Fig. 5.5. This should take care of the short coming of using the new KinFit. It is expected to lose some events that will not have converged in the more strict KinFit. In the early test performed, there seems to be more events lost than expected. This is most likely related to improper pairing of errors. This is under investigation and it is expected to be solved shortly.

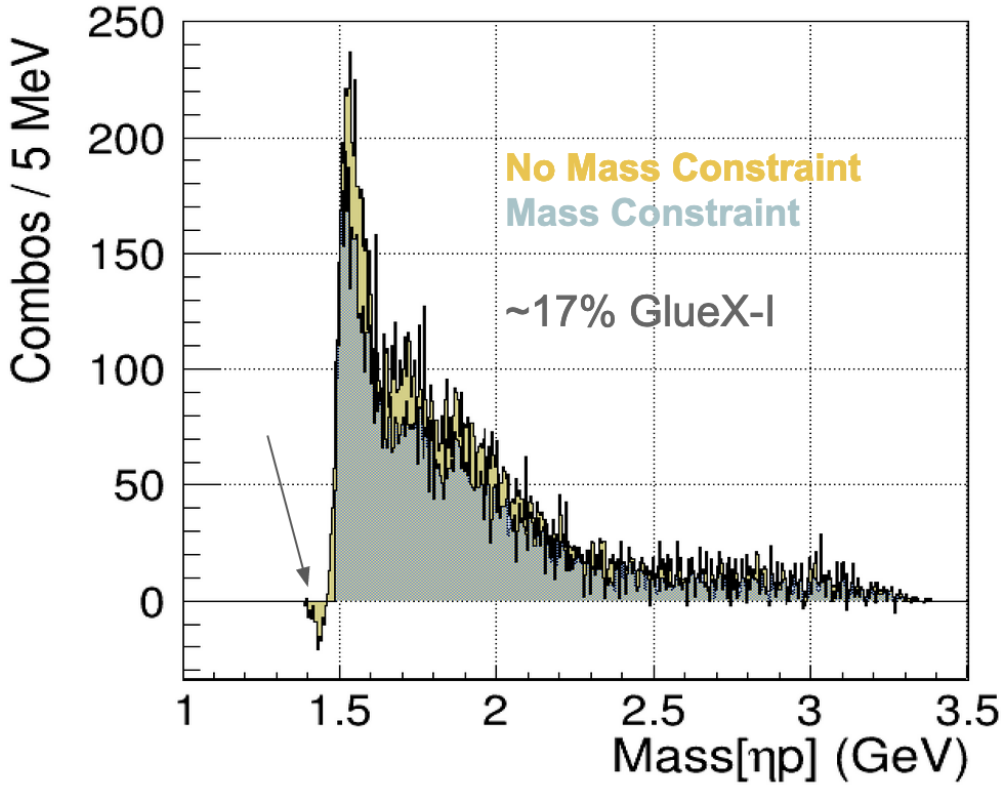

Figure 5.5: This is a preliminary test in which the events were matched between two different KinFit constraints. Notice that no events below the threshold are present in the mass constraint data.

5.3 Closing Remarks

GlueX-I, as the largest data set for photoproduced $\omega\eta$ provided meaningful insight in the search for isoscalar mesons. Using a model, in the PWA, which only includes the expected dominant waves already hints to resonant structures in the $\omega\eta$ mass. For the P wave (1^{--}), the two structures

are consistent with the $\omega(1420)$ and $\omega(1650)$. The structure at threshold for the S wave (1^{+-}), suggesting an h_1, needs to undergo a higher level of scrutiny. While the $h_1(1380)$ is a candidate for this structure, this particle has only been seen in $K\bar{K}^*$ indicating high amounts of $s\bar{s}$ content. With multiple complex phases and magnitues yielding a similar intensity description for the $m = \pm 1$ projections, the coherent sum of the waves is the most stable from the fit. While one could look at phase motion of the waves to see if these structures have a resonant behavior, the mathematical ambiguities will cause unexpected behavior. The computation of angular moments is one of the next step in the study, which will come with is own hurdles. While the general method is understood, its application to photoproduced vector-psuedoscalar final states is still in its infancy. Calculating the angular moments will not solve the ambiguity in the intensity, but it may provide a more reliable way to obtain information on the final state.

The tangential study of describing the line-shape of the N(1535) with Breit-Wigner yield a surprising result. With a direct fit of the resonance, the width was measured to be 70.5±9.2 GeV which is half of the accepted PDG value (≈150 GeV). The next steps will consist to perform the fit in the differential cross-section for M[ηp] and collaborate with theorist to seek a Breit-Wigner parameterization more suitable for the N(1535).

Both of this studies will be expanded with the GlueX-II data. It is expected that the number of statistics will increase by a factor three. With this statistics, the binning for the mass independent PWA could be made narrower. While the N(1535) differential cross-section bins could also be made narrower, perhaps the greatest benefit will be the ability to see if other N* resonances are present in the M[ηp].

APPENDIX A

Q-FACTOR STUDY

This section covers an alternative method to statistically negate the contribution of background. A more detailed description of the method can be found in the work by M. William et al. [55]. The alternative method assigns weights event by event with a quality factor (Q-factor). The closer the Q-factor of an event is to 1, the higher likelihood the event is signal. Similar to the method of sideband subtraction, the Q-factor approach is used when one cannot remove the background by some type of selection. However, unlike the sideband subtraction, the Q-factor approach uses multiple variables, not only the mass, to separate signal from background. To use the Q-factor method, there must be a variable in which one can distinguish signal from background; the *reference coordinate*. In other words, one should be able to fit the distribution on that variable with a signal and a background function. Yet, it is unnecessary to know how the signal and background are distributed in all other variables. The Q-factor approach assumes that signal and background do not quantum interfere between them and that they do not change rapidly in the variables. The method selects the nearest neighbors of an event to assign it a Q-factor. For this one computes a normalized Euclidean distance (Eq. A.1) between an event i, which will obtain a Q-factor weight, and an event j. Then, N closest neighbors to the event i are selected. The sum is over all variables (ξ_k) except for the reference coordinate (ξ_r).

$$d_{ij}^2 = \sum_{k \neq r} \left(\frac{\xi_k^i - \xi_k^j}{\sigma_k} \right)^2 \tag{A.1}$$

Once the N neighbors are selected, they are projected onto the reference coordinate along with the event for which one would like to calculate a Q-factor. Here, the distribution is fitted with a probability density function (PDF) for signal and one for background. The parameters for these functions (α) are determined for each set of neighbors according to the non-reference variables. The Q-factor of event i is calculated as the ratio between between the signal PDF and the sum of signal and background PDFs; all evaluated at the value for i in the ξ_r (Eq. A.2).

$$Q_i = \frac{F_s(\xi_r^i, \alpha_i)}{F_s(\xi_r^i, \alpha_i) + F_b(\xi_r^i, \alpha_i)} \tag{A.2}$$

It is considered a good sign if plotting in the reference coordinate the signal, events weighted by their Q value, and the background, events weighted by Q-1, the distributions follow a similar shape for the signal and background PDF (Fig. A.1).

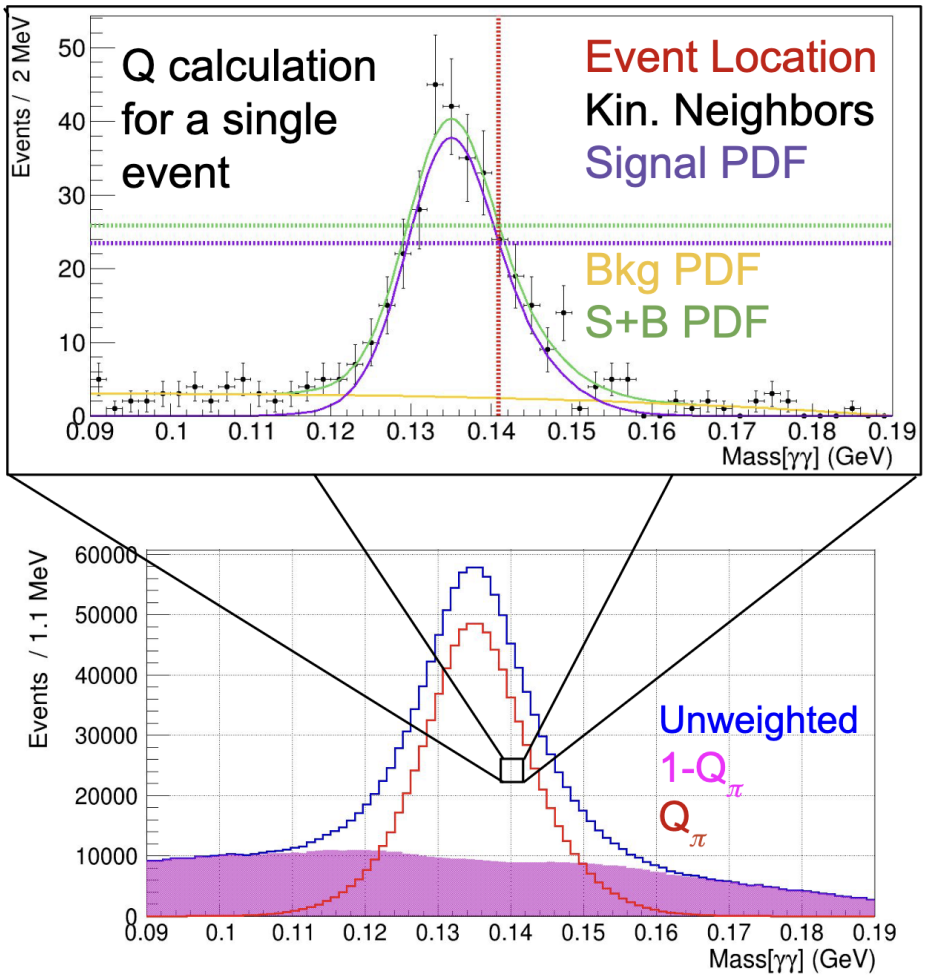

Figure A.1: Example of how an individual event gets its Q-factor

A.1 Conditional Approach for Q-Factor

The Q-factor method was designed for a 1D reference kinematic quantity (most of the time the mass) [55]. Many of the analysis done at GlueX require to take into account background in the distributions of more than one particle. There is no limitation in either the sideband subtraction or in the Q-factor that prevents them to achieve this goal. However, multiple complications can arise in either method since there could be some type of overlapping phasespace or correlation between

particles. This section briefly summarizes the study for conditional Q-factor method. While it still requires more scrutiny, the method could provide a simpler solution than a 2D fit when there is more than one reference coordinate.

When dealing with more than one reference coordinate one must first answer the question: are the distribution correlated? Any physical production of two particles must be correlated in some form. The only time where two particles in a recorded event are not correlated is when they come from different events. For example problems with timing or multiple reactions taking place at the same time. Assuming that there is a correlation, the second question one must answer is: how are the particles correlated? Many particle's mass distributions can be approximated with a Gaussian, and the 2D correlation between two particle's mass be approximates with a multivariate Gaussian distribution. However, the background in one of the reference coordinates could have a more complicated correlation to the signal or background in the other reference coordinate. There is also the possibility events that have been kinematically fitted develop a fake correlation. However, these type of events may be eliminated through a confidence level cut. Even though the 2D PDF is may be difficult to construct, one can reliably find a PDF for the 1D projection of each reference coordinate. It is possible to find the 2D PDF through the use of a copula [45]. A copula is a multivariate cumulative distribution function that describe the inter-correlation between the variables. For example, the copula that joins two Gaussian distributions is the Gaussian copula. Nonetheless, this brings the same problem as before: one needs to know the type of correlation between the distributions to properly join them.

Trying to find the type of correlation between the distributions could steer away of the main goal of estimating the amount of signal. For example, if there were red, blue, and background particles, one would like to find the amount of events in which both a red and a blue particle are present. This is the green region in Fig. A.3. If one were to use a Q-factor with two reference coordinates, this would be the region that would have a weight of Q.

This section proposes a method to calculate this area without the need of knowing how the particles are correlated through conditional probability. The only assumption made is that the Q-factor can accurately determine the signal contribution in each reference coordinate individually. This *conditional* approach, therefore, will only deal with 1D PDF, which is strongest advantage of the method. Moreover, if no correlation exists, then the method would still yield a valid answer and give the same results as a study assuming no correlation. The method consists on first calculating the Q-factor for a single particle. From the example above, assume that the Q-factor for the

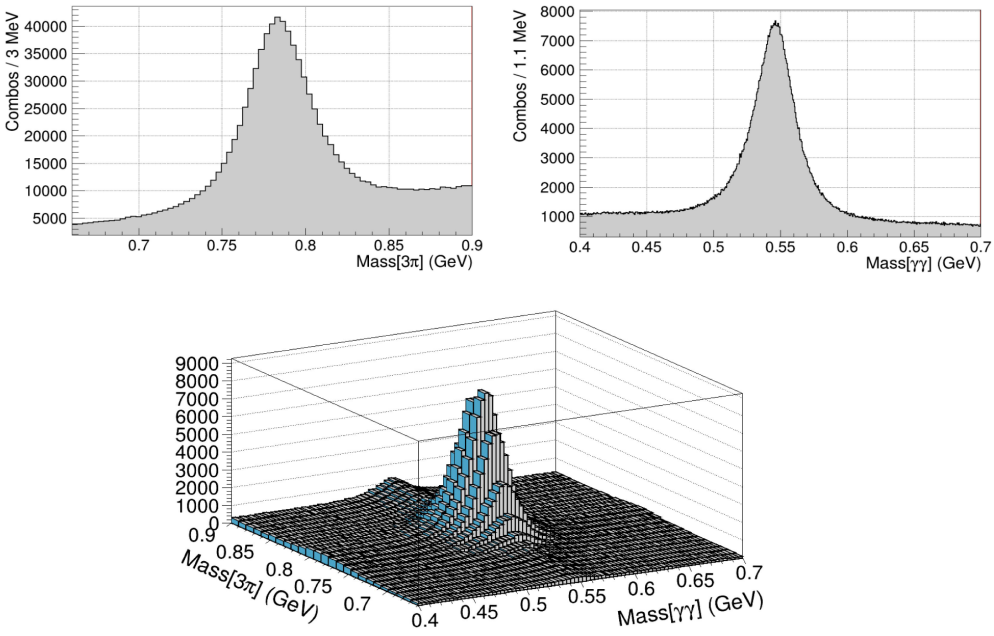

Figure A.2: The mass correlation of ω and η with the 1D projection for each particle.

blue particle is first calculated (Fig. A.4a). Then, the data is weighed by this value, and the Q-factor for the second particle (red) is calculated (Fig. A.4b). The second Q-factor calculated is the conditional probability of estimating how much red particles are given that there were only blue particles. This means that the Q-factor for the green region would be a product of the first Q-factor and the second Q-factor A.3. Note that one cannot just calculate the Q-factor for the blue particles and then calculate the Q-factor for the red particles without weighting them by the first Q-factor. This would imply that there is no correlation between the particles. The method can be repeated indefinitely for 2 or more particles by weighting the the data with the new Q-factor that was calculated. This is a great advantage since, for example, it might be extremely difficult to find a 3D PDF to perform the Q-factor directly.

$$Q_G = Q_{R\cap B} = Q_{R|B} \times Q_B \tag{A.3}$$

The figures above should help explaining the idea. What follows is a mathematical exercise to see if Eq. A.3 holds. That is, the exercise would like to show if the Q-factor for reference coordinates a and b (Q_{ab}) is equal to the conditional Q-factor approach (Eq.A.4).

$$Q_{ab} \stackrel{?}{=} Q_a Q_{b|a} \tag{A.4}$$

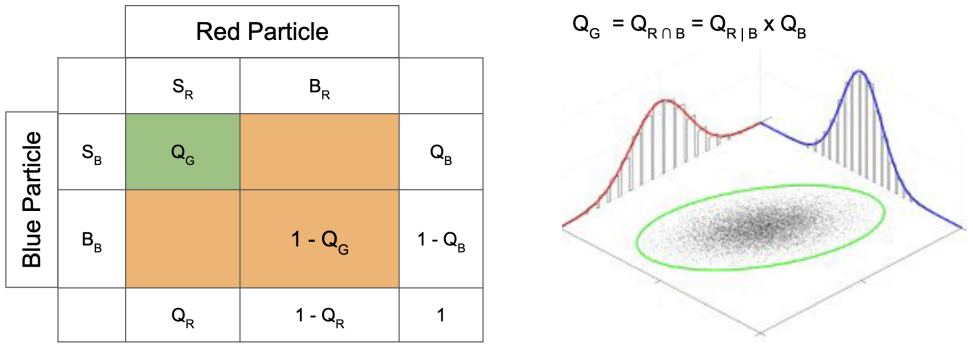

Figure A.3: The goal of the Q-factor method is to estimate the number of events that are both a blue and red particle (green region). The background will be given a weight of $1 - Q$ (orange region)

The first step is to solve the left hand side of Eq. A.4:

$$Q_{ab} = \frac{S_{ab}}{S_{ab+B_{ab}}} = \frac{P(a \cap b)}{P(a \cap b) + P(\neg a \cup \neg b)} \tag{A.5}$$

The form of $P(\neg a \cup \neg b)$ can also be expressed as:

$$\begin{aligned} P(\neg a \cup \neg b) &= P(\neg a \cap b) + P(\neg a \cap \neg b) + P(\neg b \cap a) \\ &= P(\neg a)P(b|\neg a) + P(\neg a)P(\neg b|\neg a) + P(a)(\neg b|a) \end{aligned} \tag{A.6}$$

For the right hand side of Eq. A.4 the following equations follow:

$$Q_a Q_{b|a} = \frac{P(a)}{P(a) + P(\neg a)} \cdot \frac{P(b|a)}{P(b|a) + P(\neg b|a)} \tag{A.7}$$

The numerator of this equation can be written as:

$$P(a)P(b|a) = P(a \cap b) \tag{A.8}$$

This is the same numerator as Eq. A.5. The only thing missing is to show that the denominator are the same. For the right hand side the denominator is:

$$\begin{aligned} &P(a)P(b|a) + P(a)P(\neg b|a) + P(\neg a)P(b|a) + P(\neg a)P(\neg b|a) \\ &= P(a \cap b) + P(\neg b \cap a) + P(\neg a)P(b|a) + P(\neg a)P(\neg b|a) \end{aligned} \tag{A.9}$$

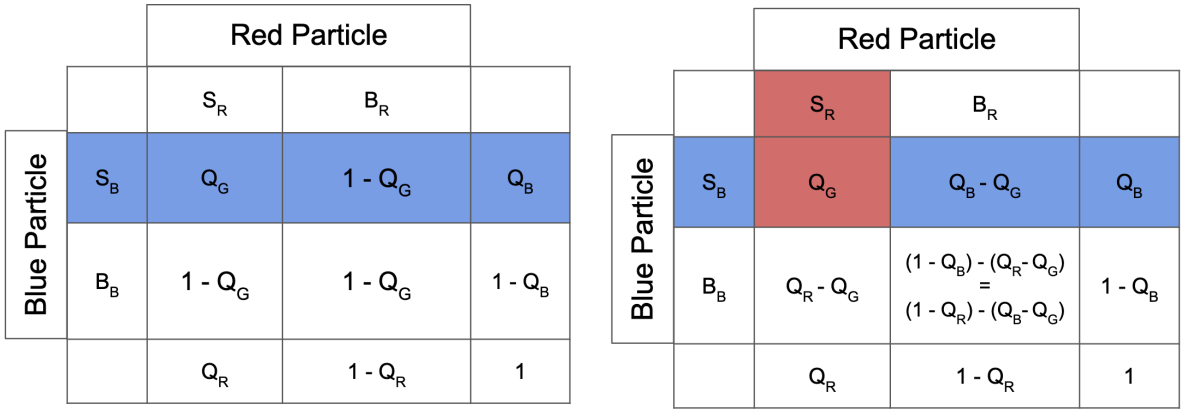

(a) The conditional method calculates first how much signal of one particle is present, in this case blue.

(b) The second step calculates the number of red particles that are present given that there is only signal for the blue particles.

Figure A.4: The conditional probability is a multi-step process

Now the initial question can be solved:

$$\begin{aligned} Q_{ab} &= Q_a Q_{b|a} \Rightarrow \\ P(\neg a)P(\neg b|a) + P(\neg a)P(b|a) &= P(\neg a)P(b|\neg a) + P(\neg a)(\neg b|\neg a) \\ P(\neg a)[P(b|a) + P(\neg b|a)] &= P(\neg a)[P(b|\neg a) + P(\neg b|\neg a)] \\ P(\neg a)[1] &= P(\neg a)[1] \end{aligned} \tag{A.10}$$

Testing the Method. The method seems plausible, mathematically speaking. Now, the only thing that is missing is to test it. The test shown below are performed on data. This is not ideal since one cannot know how close to the *true* solution the result is. However, the consistency of the method and how it compares to a non-correlated Q-factor can be estimated. To properly test this in MC, it is necessary to provide all the information for signal and background. This means that the angular distributions should be included when generating the MC samples. This would mean that ideally, one would like to fit the signal and background regions with a PWA. Then one would have the adequate MC samples to test this method.

The test used the same selection as described in the main analysis. The software used to calculate the Q-factor was written by Lawrence Ng and can be found in a the GitHub repository in Ref. [46]. The reference coordinates were M[3π] and M[$\gamma\gamma$]. The other coordinates used to estimate the distance were: the momentum transfer for the $\omega\eta$ system, the helicity angles for ω that describe

the decay of the $\omega\eta$ system, the helicity angles for the normal to the decay plane formed by the pions in the ω decay, the angles that describe the decay of η into two photons, and the angles that describe the decay of π^0 into two photons. These coordinates were used following the adivce given by Ref.[42] Note that the coordinates were the same for both stages of the calculation. These coordinates would be the same if one were to perform a 2D Q-factor calculation directly. The number of neighbors used to obtain the Q-factor was 100. It is very important that one uses the same neighbors in both steps of the conditional Q-factor. Fig. A.5 shows the reference coordinates and the distribution weighted by the Q-factor obtained for that stage. The Q-factor for ω was first calculated, then the Q-factor for η given ω. The alternative order was also computed, as well as the Q-factor that assumes no correlation between η and ω. The results are displayed in Fig. A.6. The last plot in the figure plots the ratio between the final Q-factor weight. The ratio between the two options for the conditional Q-factor is .96, except near the $\omega\eta$ threshold where the ratio drops. It is interesting to see that the Q-factor which assumed no correlation can be between 90% - 94% close to the conditional Q-factor value. These results show certain degree of consistency for the method and points that calculating a Q-factor assuming no correlation might over-estimate the background. Note that if there was in fact no correlation between the η and ω, then all three ratios would be closer to each other. It remains to investigate why the two different ways to calculate the conditional Q-factor are not closer to 1. Equally important, it remains to properly calculate how the errors would propagate for the method, and compare those to the 2D PDF direct approach.

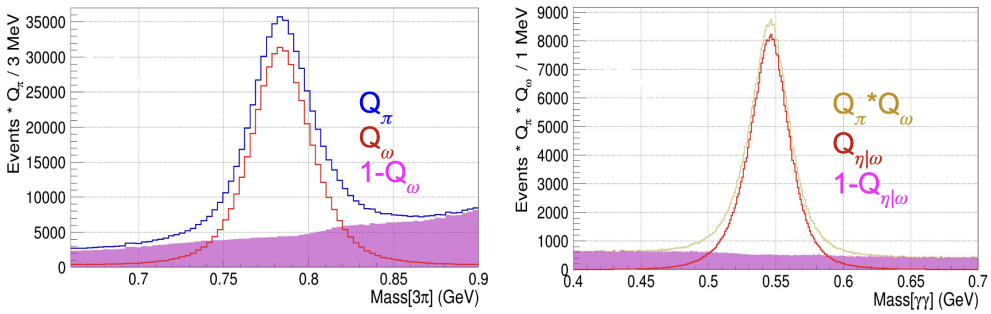

Figure A.5: The conditional Q-factor was calculated for ω and η. In this plots, ω was calculated first.

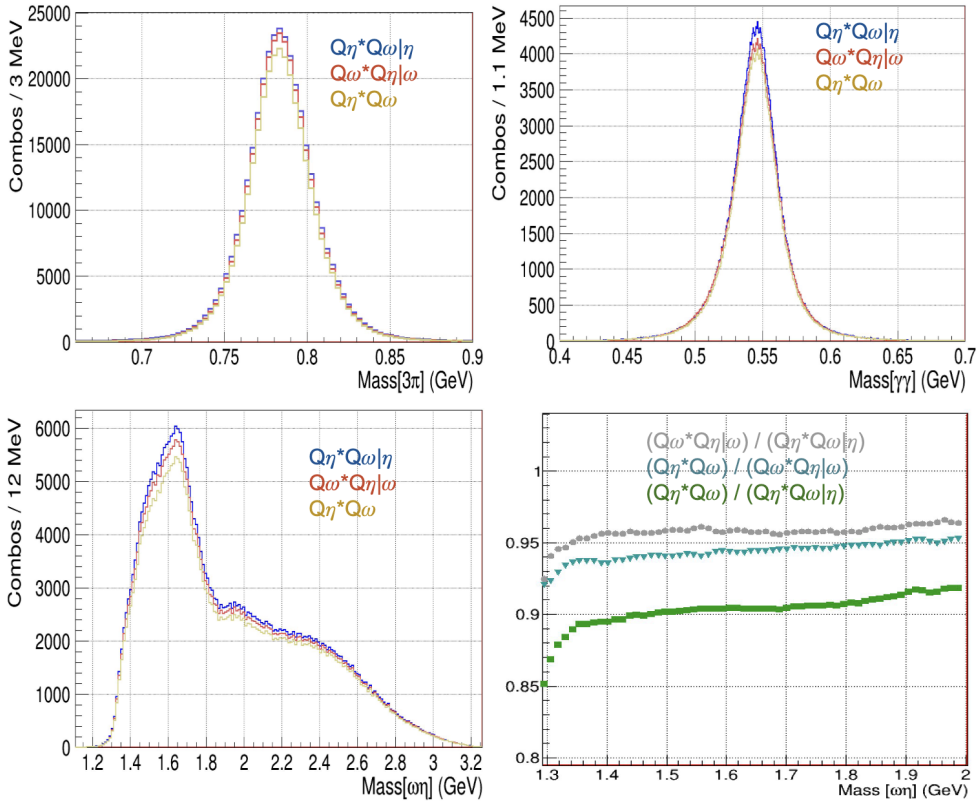

Figure A.6: These plots show the end result of weighting the mass distribution by the conditional Q-factor; blue has Q_η calculated first, orange has Q_ω calculated first, and golden assumes that the particles are not correlated.

BIBLIOGRAPHY

[1] J. et al. Allison. Geant4 developments and applications. *IEEE Transactions on Nuclear Science*, 53(1):270–278, 2006.

[2] Edmundo Barriga and Kevin Scheuer. Mathematical ambiguities in vector-pseudoscalar amplitude analysis. *GlueX Private Documents*, 2023.

[3] R. Barsotti and M.R. Shepherd. Using machine learning to separate hadronic and electromagnetic interactions in the gluex forward calorimeter. *Journal of Instrumentation*, 15(05):P05021, may 2020.

[4] Ł. Bibrzycki, C. Fernández-Ramírez, V. Mathieu, M. Mikhasenko, M. Albaladejo, A. N. Hiller Blin, A. Pilloni, and A. P. Szczepaniak. $$\pi ˆ-p\rightarrow \eta ˆ{(\prime)}\, \pi ˆ- p$$in the double-Regge region. *The European Physical Journal C*, 81(7):647, July 2021.

[5] Bradford Cannon. *Search for new and unusual stangeonia states using $\gamma p \to p\phi\eta$ with GlueX at Thomas Jefferson National Accelerator Facility.* PhD thesis, Florida State University, 2019.

[6] Kandice Carter. Jefferson lab accelerator delivers its first 12 gev electrons, Dec 2015.

[7] Frank E. Close and Philip R. Page. The production and decay of hybrid mesons by flux-tube breaking. *Nuclear Physics B*, 443(1):233–254, 1995.

[8] GlueX Collab. Simulation for gluex repository. `https://github.com/JeffersonLab/halld_sim`, 2023.

[9] GlueX Collaboration. Analysis launch cuts.

[10] GlueX Collaboration. A search for qcd exotics using a beam of photons. *GlueX Public Documents*, 2004.

[11] Wikimedia Commons. Standard model of elementary particles, 2019.

[12] Jozef J. et al. Dudek. Toward the excited isoscalar meson spectrum from lattice qcd. *Phys. Rev. D*, 88:094505, Nov 2013.

[13] H. Bilokon et al. Coherent bremsstrahlung in crystals as a tool for producing high energy photon beams to be used in photoproduction experiments at cern sps. *Nuclear Instruments and Methods in Physics Research*, 204(2):299–310, 1983.

[14] J. Allison et al. Recent developments in geant4. *Nuclear Instruments and Methods in Physics Research Section A: Accelerators, Spectrometers, Detectors and Associated Equipment*, 835:186–225, 2016.

[15] J. Kuhn et al. Exotic meson production in the $f_1(1285)\pi^-$ system observed in the reaction $\pi^- p \to \eta\pi^+\pi^-\pi^- p$ at 18 gev/c. *Physics Letters B*, 595(1):109–117, 2004.

[16] J. Stevens et al. The gluex dirc project. *Journal of Instrumentation*, 11(07):C07010, jul 2016.

[17] M. Ablikim et al. Observation of an isoscalar resonance with exotic $J^{PC} = 1^{-+}$ quantum numbers in $j/\psi \to \gamma\eta\eta^{'}$. *Phys. Rev. Lett.*, 129:192002, Oct 2022.

[18] M. Lu et al. Exotic meson decay to $\omega\pi^0\pi^-$. *Phys. Rev. Lett.*, 94:032002, Jan 2005.

[19] R. L. Workman et al. Review of Particle Physics. *PTEP*, 2022:083C01, 2022.

[20] S. Agostinelli et al. Geant4—a simulation toolkit. *Nuclear Instruments and Methods in Physics Research Section A: Accelerators, Spectrometers, Detectors and Associated Equipment*, 506(3):250–303, 2003.

[21] S. Boyarinov et al. The clas12 data acquisition system. *Nuclear Instruments and Methods in Physics Research Section A: Accelerators, Spectrometers, Detectors and Associated Equipment*, 966:163698, 2020.

[22] S. Eidelman et al. Review of particle physics. *Physics Letters B*, 592(1):1–5, 2004. Review of Particle Physics.

[23] Torbjörn Sjöstrand et al. An introduction to pythia 8.2. *Computer Physics Communications*, 191:159–177, 2015.

[24] Y. Van Haarlem et al. The gluex central drift chamber: Design and performance. *Nuclear Instruments and Methods in Physics Research Section A: Accelerators, Spectrometers, Detectors and Associated Equipment*, 622(1):142–156, 2010.

[25] B. Aubert et al. (BaBar Collaboration). The $e^+e^- \to 3(\pi^+\pi^-)$, $2(\pi^+\pi^-\pi^0)$ and $K^+K^-2(\pi^+\pi^-)$ cross sections at center-of-mass energies from production threshold to 4.5 gev measured with initial-state radiation. *Phys. Rev. D*, 73:052003, Mar 2006.

[26] M. Ablikim et al. (BESIII Collaboration). Observation of a resonant structure in $e^+e^- \to \omega\eta$ and another in $e^+e^- \to \omega\pi^0$ at center-of-mass energies between 2.00 and 3.08 gev. *Physics Letters B*, 813:136059, 2021.

[27] R.R. Akhmetshin et al. (CMD-3 Collaboration). Study of the process $e^+e^- \to \pi^+\pi^-\pi^0\eta$ in the c.m. energy range 1394-2005 mev with the cmd-3 detector. *Physics Letters B*, 773:150–158, 2017.

[28] P. Eugenio et al. (E852 Collaboration). Observation of a new $J^{PC} = 1^{+-}$ isoscalar state in the reaction $\pi^- p \to \omega\eta p$ at 18 gev/c. *Physics Letters B*, 497(3):190–198, 2001.

[29] S. Adhikari et al. (GlueX). The gluex beamline and detector. *Nuclear Instruments and Methods in Physics Research Section A: Accelerators, Spectrometers, Detectors and Associated Equipment*, 987:164807, 2021.

[30] M. Atkinson et al. (Omega Photon Collaboration. A peak in the $\omega\eta$ mass spectrum from diffractive photoproduction. *Z. Phys. C - Particles and Fields*, 34:303–306, 1987.

[31] M. N. Achasov et al. (SND Collaboration). Measurement of the $e^+e^- \to \omega\eta$ cross section below $\sqrt{s} = 2$ GeV. *Phys. Rev. D*, 94:092002, Nov 2016.

[32] Thomas Jefferson National Accelerator Facility. Jefferson lab website tour.

[33] Paul Geiger and Eric S. Swanson. Distinguishing among strong decay models. *Phys. Rev. D*, 50:6855–6862, Dec 1994.

[34] GlueX. Gluex picture archive.

[35] R. Jones. Intense beams of polarized and nearly monochromatic photons from coherent bremsstrahlung, Aug 1997.

[36] R. E. Kalman. A New Approach to Linear Filtering and Prediction Problems. *Journal of Basic Engineering*, 82(1):35–45, 03 1960.

[37] R. E. Kalman and R. S. Bucy. New Results in Linear Filtering and Prediction Theory. *Journal of Basic Engineering*, 83(1):95–108, 03 1961.

[38] Richard Kokoski and Nathan Isgur. Meson decays by flux-tube breaking. *Phys. Rev. D*, 35:907–933, Feb 1987.

[39] J. I. Latorre, P. Pascual, and S. Narison. Spectra and hadronic couplings of light hermaphrodite mesons. *Zeitschrift für Physik C Particles and Fields*, 34(3):347–360, 1987.

[40] Christoph W. Leemann, David R. Douglas, and Geoffrey A. Krafft. The continuous electron beam accelerator facility: Cebaf at the jefferson laboratory. *Annual Review of Nuclear and Particle Science*, 51(1):413–450, 2001.

[41] B. R. Martin. *Nuclear and Particle Physics.* Wiley, 2012.

[42] C. Meyer. Notes on q-factor analyses. *GlueX Private Documents*, 2022.

[43] C. A. Meyer and Y. Van Haarlem. Status of exotic-quantum-number mesons. *Phys. Rev. C*, 82:025208, Aug 2010.

[44] C.A. Meyer and E.S. Swanson. Hybrid mesons. *Progress in Particle and Nuclear Physics*, 82:21–58, 2015.

[45] Roger B. Nelson. *An Introduction to Copulas.* Springer, 2006.

[46] Lawrence Ng. Qfactors. `https://github.com/lan13005/QFactors`, 2022.

[47] A. Rodas, A. Pilloni, M. Albaladejo, C. Fernández-Ramírez, A. Jackura, V. Mathieu, M. Mikhasenko, J. Nys, V. Pauk, B. Ketzer, and A. P. Szczepaniak. Determination of the pole position of the lightest hybrid meson candidate. *Phys. Rev. Lett.*, 122:042002, Jan 2019.

[48] C. Salgado and V. Mathieu. Comparing formalisms for the analysis of two-pseudoscalar mesons produced by linearly polarized photons. *GlueX Public Documents*, 2020.

[49] C. Salgado and D. Weygand. On the partial-wave analysis of mesonic resonances decaying to multiparticle final states produced by polarized photons. *Physics Reports*, 537(1):1–58, 2014. On the Partial-Wave Analysis of Mesonic Resonances Decaying to Multiparticle Final States Produced by Polarized Photons.

[50] Amy Schertz. *Partial Wave Analysis of the $\omega\pi^-$ Final State Photoproduced at GlueX*. PhD thesis, William & Mary, 2022.

[51] Mattthew Shepherd. AmpTools User Guide. 2021.

[52] T. Shimada, A.D. Martin, and A.C. Irving. Double regge exchange phenomenology. *Nuclear Physics B*, 142(3):344–364, 1978.

[53] Torbjörn Sjöstrand, Stephen Mrenna, and Peter Skands. Pythia 6.4 physics and manual. *Journal of High Energy Physics*, 2006(05):026, may 2006.

[54] A Somov. Level-1 Trigger and DAQ system of the GlueX experiment. In *APS Division of Nuclear Physics Meeting Abstracts*, APS Meeting Abstracts, page HH.004, October 2008.

[55] M Williams, M Bellis, and C A Meyer. Multivariate side-band subtraction using probabilistic event weights. *Journal of Instrumentation*, 4(10):P10003, oct 2009.

BIOGRAPHICAL SKETCH

Edmundo Sebastian Barriga was born in Mexico City, Mexico. He moved to the U.S. when he was 16 years old. There, he finished his last two years of high school in the IB program of Miami Beach Senior High. He continue his education in Miami Dade Honors College were he received a A.A. in Physics and transferred to Florida International Univeristy (FIU). He graduated from FIU with a B.S. in Physics with a minor in Mathematics. In 2016, he started his Ph.D. in Physics at Florida State University (FSU).